AN EXPERIMENTAL INVESTIGATION OF THE STATIC AND DYNAMIC PERFORMANCE OF HORIZONTAL-APPLICATION AND VERTICAL-APPLICATION THREE-LOBE BEARINGS

A Thesis

by

RASISH KHATRI

Submitted to the Office of Graduate and Professional Studies of
Texas A&M University
in partial fulfillment of the requirements for the degree of

MASTER OF SCIENCE

Chair of Committee,	Dara W. Childs
Committee Members,	Luis San Andrés
	James R. Morgan
Head of Department,	Andreas Polycarpou

August 2014

Major Subject: Mechanical Engineering

ABSTRACT

Static and dynamic performance test results are provided for a horizontal-application three-lobe bearing evaluated over the following range of static-load orientations (all taken from the leading edge of the loaded pad): 0^o, 20^o, 30^o, 40^o, 60^o, 80^o, 90^o, and 100^o. This bearing has the following specifications: 100^o pad arc angle, 0.52 preload, 70% offset, 101.74 mm (4.0057 in) minimum bore diameter, 0.116 mm (7.55 mils) radial pad clearance, and 76.3 mm (3 in) axial length. The static and dynamic test results are evaluated to determine the sensitivity of the bearing to changes in the static load direction. The two questions the study aims to answer are: (1) "Is an offset three-lobe bearing a good choice when the radial static load vector represents an unknown variable?" and (2) "Can an offset three-lobe bearing be oriented advantageously with a known load direction?" Both the static and dynamic test results are compared to predictions obtained from a fixed-arc bearing Reynolds equation solver. Predictions using both the measured hot clearance and measured cold clearance as inputs are compared to the measured data.

Dynamic tests show that the horizontal-application three-lobe bearing is sensitive to load orientation at low speeds and high loads. Whirl-frequency ratios (WFR) at 6750 rpm with loads of 1149 kPa, 1723 kPa, and 2298 kPa are equal to zero for loads oriented towards the leading edge of the pad, and between 0.35 and 0.5 for loads oriented towards the trailing edge of the pad. This same general trend can be seen for WFR values at 9000 rpm and 10800 rpm. The horizontal-application three-lobe bearing is not sensitive to load orientation at high speeds and light loads. At 13200 rpm, measured WFRs are between 0.3 and 0.7 at all loads and for all load orientations. Measured WFR at the no-load condition are between 0.45 and 0.7 for all cases.

Stiffness orthotropy was found to vary significantly with load orientation. At 6750 rpm and 2298 kPa, the bearing is most orthotropic when the static load orientation is 30^o and 40^o, with K_{yy} being larger than K_{xx} by approximately 800 MN/m. At 13200

rpm and 2298 kPa, the bearing is most orthotropic for the 40^o and 100^o load orientations, with K_{yy} being larger than K_{xx} by approximately 800 MN/m.

Overall, it is concluded that the three-lobe bearing is not a good choice when the load direction is unknown, as the bearing can have different rotordynamic coefficients with different load orientations. Also, at high speeds, the three-lobe bearing cannot be oriented advantageously with a known load direction to enhance stability, as the WFR of the three-lobe bearing tested is largely independent of load direction. However, the three-lobe bearing can be oriented advantageously to split/change a critical speed, since the direct stiffness and stiffness orthotropy change with load direction.

Additionally, dynamic performance test results are provided for a vertical-application (nominally unloaded) three-lobe bearing. The vertical-application bearing has the following specifications: 100^o pad arc angle, 0.64 preload, 100% offset, 101.74 mm (4.0057 in) nominal diameter, 0.116 mm (5.27 mils) radial pad clearance, 76.3 mm (3in) axial length, and 100° static load orientation from the leading edge of the loaded pad. The performance of this bearing is evaluated to determine: (1) whether a fully (100%) offset three-lobe bearing configuration is more stable in terms of the WFR than a standard plain journal bearing and (2) whether a fully offset three-lobe bearing provides a larger direct stiffness (centering force) than a standard fixed-arc bearing.

Dynamic tests show that the vertical-application three-lobe bearing does not improve stability over conventional plain journal bearings. The measured WFRs for the vertical-application bearing are approximately 0.4-0.5 for nearly all test cases. Predicted WFRs are 0.46 at all test points. The vertical-application bearing dimensionless direct stiffness coefficients are compared to those for the horizontal-application bearing. The equivalent stiffness for the vertical-application bearing is larger than that of the horizontal-application bearing by a factor of 1.33 at 6750 rpm and a factor of 1.25 at 9000 rpm. Thus, the vertical-application bearing does impart a larger centering force to the journal relative to the horizontal-application bearing when the journal is not carrying a radial static load.

DEDICATION

To Rakhi, without whom,

this would have never been possible.

Thank You.

ACKNOWLEDGEMENTS

I would like to express my sincerest gratitude to Dr. Dara W. Childs for giving me the opportunity to work and research under him at the Turbomachinery Lab. His patience, dedication, and support throughout this process were much appreciated, and the technical guidance he provided was invaluable.

Several students and co-workers at the Turbomachinery Lab also helped me throughout my research. I want to thank Jason Wilkes for introducing me to the test rig and providing key insight throughout my time at the Turbo Lab. David Tschoepe was a tremendously valuable partner and friend during my time at the Turbo Lab, and his high mechanical aptitude proved instrumental at times. David Coghlan helped me by re-running several of my bearing tests and dedicating time to helping me learn from his experiences with the test rig. Jennifer Gaines, Matt Kluitenberg, and Jesse Salas played extremely pivotal roles in helping me to re-test my bearing and re-confirm several of my results. All of these individuals dedicated a significant amount of time to helping me, and I can say with a high degree of certainty that I could not have completed this process without their assistance.

I also want to thank Dr. Alan Palazzolo and Dr. Luis San Andrés for being outstanding educators and helping me to understand the fundamentals of rotordynamics and fluid-film lubrication. The lessons I learned in their classes have been a great aid to my research and my career.

NOMENCLATURE

$\boldsymbol{A_{ij}}$	Frequency-domain representation of the rotor-bearing absolute acceleration [L/t^2]
C_b	Radial bearing clearance [L], as defined in Eq. (1)
c_{ij}	Dimensionless direct and cross-coupled damping coefficients [-], defined by Eq. (8b)
C_{ij}	Direct and cross-coupled damping coefficients [F.t/L], defined by Fig. 6
C_p	Radial pad clearance [L], as defined in Eq. (2)
D	Bearing diameter [L]
$\boldsymbol{D_{ij}}$	Frequency-domain representation of the rotor-bearing relative displacement [L]
e	Eccentricity [L], defined by Fig. 1 and Eq. (9)
f_{bi}	Bearing Forces [F], defined by Eq. (5)
$\boldsymbol{F_s}$	Static Load Vector [F], defined by Figure 1
F_x , F_y	External loads applied in the x and y directions, respectively [F]
$\boldsymbol{H_{baseline}}$	Measured baseline complex dynamic stiffness coefficients [F/L]
$\boldsymbol{H_{ij}}$	Fluid-film bearing complex dynamic stiffness coefficients [F/L], defined by Eq. (15)
$\boldsymbol{H_{measured}}$	Total measured complex dynamic stiffness coefficients [F/L]
$\boldsymbol{j}$	Imaginary unit$\sqrt{-1}$ [-]
k_{eq}	Bearing equivalent stiffness [-], as defined by Eq. (7)
k_{ij}	Dimensionless direct and cross-coupled stiffness coefficients [-], as defined by

	Eq. (8a)
$\overline{k_{ij}}$	Dimensionless direct and cross-coupled stiffness coefficients [-], as defined by Eq. (25)
K_{ij}	Direct and cross-coupled stiffness coefficients [F/L], defined by Fig. 6
L	Pad axial length [L]
M_p	Dimensionless bearing preload [-], as defined in Eq. (3)
M_{ij}	Direct and cross-coupled virtual mass coefficients [M], defined by Fig. 6
M_s	Combined mass of bearing and bearing housing [M]
R_b	Radius of bearing [L], as defined in Figure 3
R_j	Radius of journal [L], as defined in Figure 3
R_p	Radius of pad [L], as defined in Figure 3
T_{in}	Oil Inlet Temperature [T]
T_o	Oil Outlet Temperature[T]
α	Bearing offset [-], as defined in Eq. (4)
$\Delta x, \Delta y$	Relative displacement between journal and bearing [L]
$\Delta \boldsymbol{H_{ij}}$	Repeatability of complex dynamic stiffness coefficients [F/L], defined by Eq. (24)
ε	Dimensionless eccentricity [-], defined by Eq. (10)
ω_s	Operating speed [1/t]
Ω	Excitation frequency [1/t]
φ	Attitude angle [-], defined by Fig. 1 and Eq. (11)

θ	Circumferential angle relative to the leading edge of pad [-], as defined in Figure 2
θ_L	Load orientation [-], as defined in Figure 2
θ_{min}	Angular location of min film thickness for centered rotor [-], as defined in Figure 3
θ_{pad}	Pad arc angle [-], as defined in Figure 2
CC	Cold Clearance
FFT	Fast Fourier Transform
HC	Hot Clearance
OEM	Original Equipment Manufacturer
OSI	Onset speed of instability
SEP	Static equilibrium position
WFR	Whirl-frequency ratio, defined by Eq. (6)

TABLE OF CONTENTS

LIST OF FIGURES

Page

LIST OF TABLES

Page

INTRODUCTION

Journal Bearings and Rotordynamics

Hydrodynamic bearings support the loads applied to a rotor-bearing system using a thin film of lubricant. Often times, a rotor-bearing system can be subject to large vibrations caused by (1) synchronous response due to rotor imbalance and (2) subsynchronous, self-exciting bearing instabilities called oil-whirl or oil-whip. Although the synchronous response near critical speeds encompasses the majority of rotordynamics-related vibration problems in modern, commercial turbomachinery, subsynchronous vibrations comprise the more dangerous and more damaging problems [1]. Subsynchronous vibrations in rotor-bearing systems can cause sudden, unforeseen mechanical failure.

Hydrodynamic bearings contribute stiffness and damping forces to the overall dynamics of rotating machinery and can have a large impact on either exciting or reducing potentially destructive high-amplitude vibrations. In fact, the damping in many rotating machines comes almost exclusively from their fluid-film bearings and seals [1]. Often times, performance and efficiency are the principal concerns for turbomachinery original equipment manufacturers (OEMs), and the appropriate consideration for structural vibrations and related reliability problems is put off until most components have been designed [2]. At that point, the simplest and most cost-effective modifications to make in the system are usually at the bearings. In addition to the dynamic properties of bearings, the static response and thermal performance of bearings can also greatly affect the overall system reliability and efficiency. Therefore, proper bearing design is essential to the cost-effective, efficient, and reliable performance of all rotating equipment.

Three-Lobe Bearing Design

Figure 1 illustrates the static behavior of a plain journal bearing.

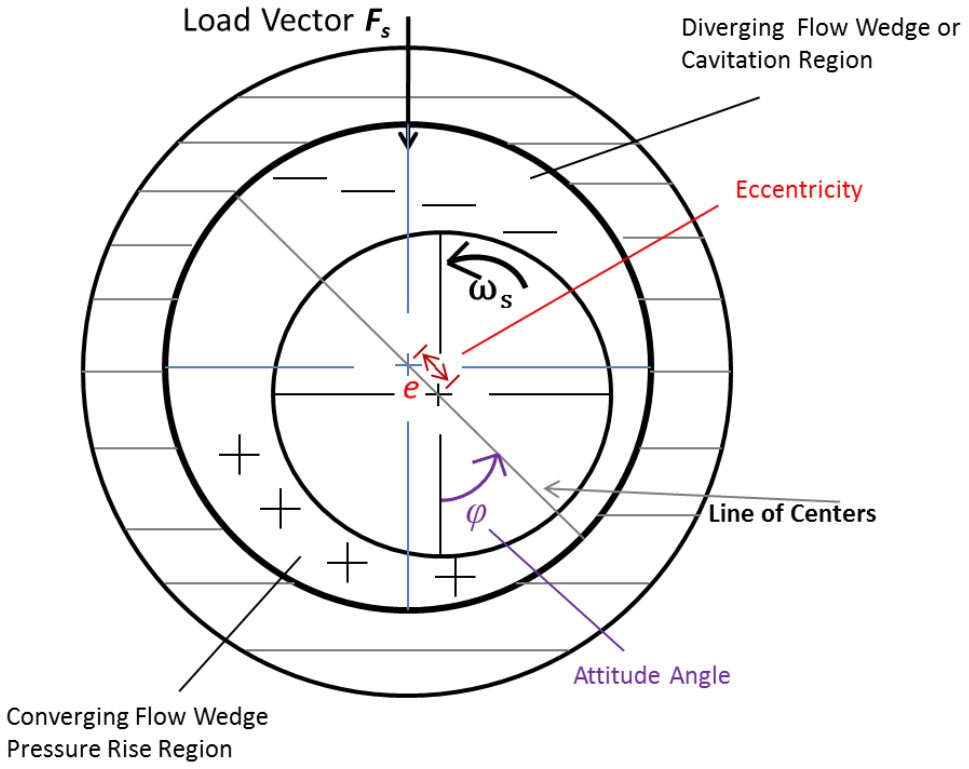

Figure 1. Static behavior of a journal supported by a plain journal bearing

The static load vector, $\boldsymbol{F}_s$, displaces the journal from the center of the bearing to some eccentric position, e. The journal typically displaces at some angle to the load

vector called the attitude angle, φ. This occurs as the journal attempts to find its static equilibrium position (SEP), the location at which the resultant of all applied and reaction forces acting on the journal is equal to zero. The eccentricity helps to create a converging-diverging oil wedge. A converging-diverging oil wedge is essential to generating the pressure required to lift the rotor off the bearing by creating regions of increasing and decreasing pressure. Typically, higher rotor speeds yield lower eccentricities and higher attitude angles; conversely, higher static loads yield higher eccentricities and lower attitude angles in fixed-arc bearings.

The cross section of a typical three-lobe bearing is shown in Figure 2.

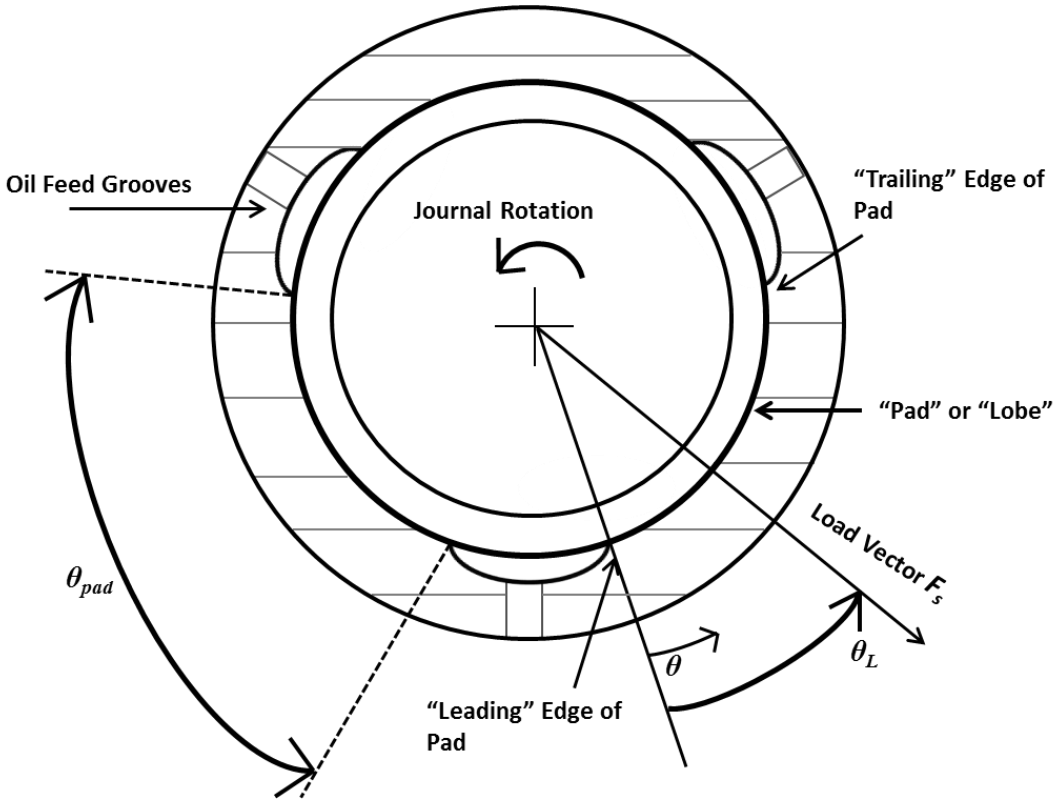

Figure 2. Basic geometry of a three-lobe bearing

The three curved surfaces nearest the journal are the pads (or lobes) of the bearing, and the areas in between are the oil grooves. The total arc angle of the pads, θ_{pad}, is illustrated in Figure 2. The journal rotation direction (illustrated as counter-clock-wise in Figure 2) defines the direction from the leading edge of the pad to the trailing edge of the pad.

θ, as shown in Figure 2, defines the angular coordinate from the leading edge of the pad. The static load orientation, defined by θ_L in Figure 2, is the angle from the leading edge of the pad to the static load vector. θ_L is a major variable of interest in this study. Three-lobe bearings are usually designed with a pre-specified θ_L, because the stiffness and damping provided by the bearing can vary depending on the direction of the static load vector. In this thesis, static load orientation is always referenced as an angular position relative to the leading edge of the pad.

The static load magnitude and direction on each bearing of a horizontal machine can usually be calculated from the weight and center of gravity of the rotor. In some cases, however, the net static load vector on the bearing includes other forces, such as the hydrodynamic side loads seen in centrifugal pumps. In such cases, the static load orientation may be unknown or may vary from one machine to the next, in serial production.

Vertical machines generally carry no radial static load, and special care must be taken at the design stage to ensure a converging-diverging oil wedge. This is discussed in detail later in this section.

Figure 3 illustrates the definition of the journal radius, bearing radius, and pad radius. R_j is the radius of the journal. The bearing radius, R_b, is defined as the distance from the center of a centered journal to the nearest point on the bearing. The pad radius, R_p, is the distance from the radial center of the pad arc to any point on the pad. In multi-lobe bearings, R_p is generally greater than R_j. Equivalently, this means that the radial

center of the pad arc is displaced some distance from the center of the rotor, when the rotor is centered within the bearing. The angular location of the minimum clearance for the centered rotor, θ_{min}, is also noted in Figure 3.

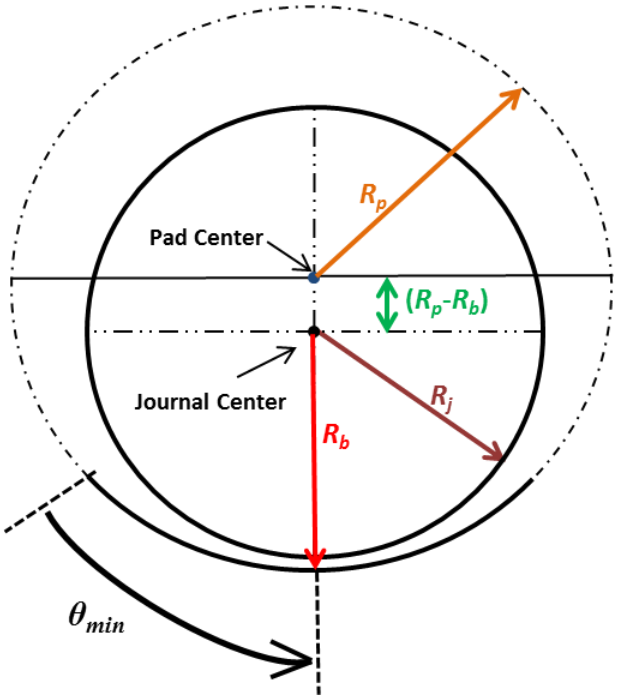

Figure 3. Geometrical description of journal, bearing, and pad radii

The radial bearing clearance, also called assembly clearance, is the minimum clearance for a centered rotor, defined by:

$$C_b = R_b - R_j \tag{1}$$

The radial pad clearance, or machined clearance, is defined by:

$$C_p = R_p - R_j \tag{2}$$

The pad preload, M_p, is defined by:

$$M_p = \frac{C_p - C_b}{C_p} = 1 - \frac{C_b}{C_p} = \frac{R_p - R_b}{R_p - R_j} \tag{3}$$

Figure 4 illustrates the concept of the pad preload.

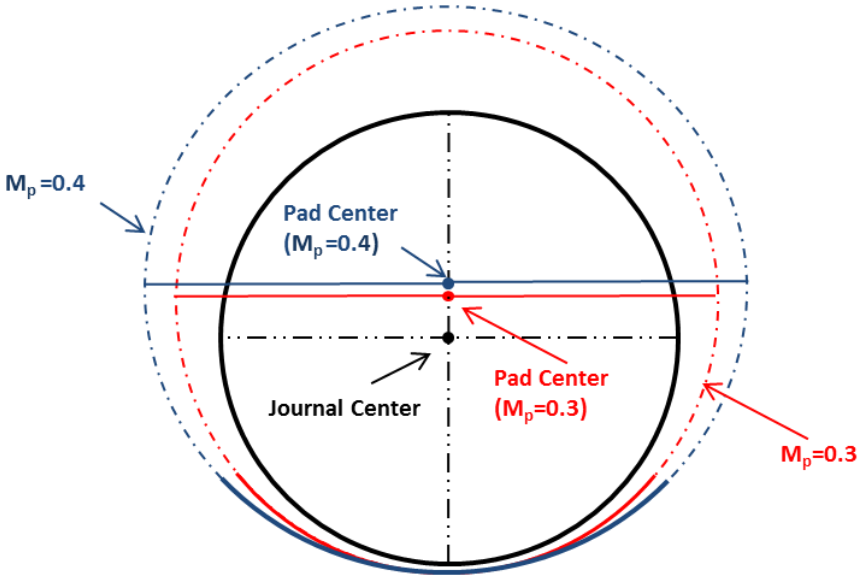

Figure 4. Geometric description of bearing preload

Sometimes, the numerator of Eq. (3) is simply referred to as the "preload", while the entire equation is called the "dimensionless preload." In this paper, the term

"preload" always refers to Eq. (3). A positive preload corresponds to the pad radius of curvature being larger than the journal radius. A zero preload corresponds to the shaft and bearing being concentric, as in the case of a plain journal bearing. Positively preloading a bearing creates a converging-diverging oil wedge, even when the rotor is centered. A converging-diverging oil wedge is important for generating pressure to provide lift (direct static stiffness) to the journal, as mentioned earlier. A negative preload will create an undesirable divergent-convergent oil-film wedge, and is avoided in practice.

The bearing offset, α, is defined by:

$$\alpha = \frac{\theta_{min}}{\theta_{pad}} \tag{4}$$

Figure 5 illustrates both a 50% offset pad and a 100% offset pad. The bearing offset dictates the angular location of the minimum oil-film thickness (or clearance) relative to the leading edge of the pad for a centered journal. For example, a 75% offset on an 80° arc pad corresponds to the minimum clearance being located 60° from the leading edge of the pad. Offsets greater than or equal to 50% are generally desired to have a larger portion of a converging oil wedge across the pad. An imaginary line connecting the location of the minimum film thickness on the pad to the pad center must cross through the center of a preloaded journal bearing, as shown in Figure 5.

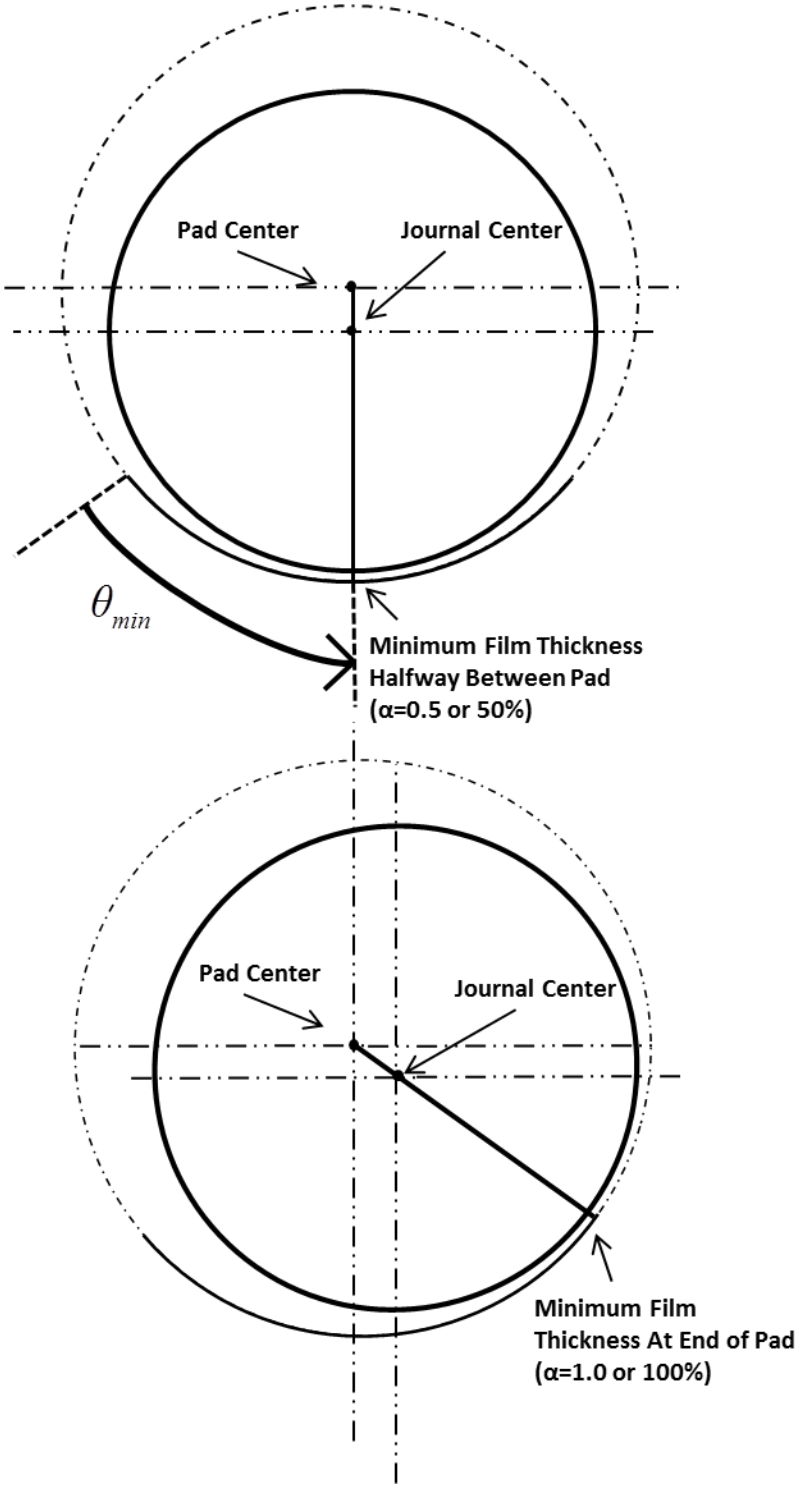

Figure 5. Physical description of offset

Table 1 summarizes the important three-lobe bearing geometrical parameters.

Table 1. Multi-lobe Bearing Geometrical Parameters

Symbol	Parameter	Definition
θ_{pad}	Pad Arc Angle	The total arc angle of an individual pad
L	Bearing Axial Length	Axial length of the pads
R_j	Journal Radius	Radius of the journal
R_p	Pad Radius	Radius of the bearing pads
R_b	Bearing Radius	Distance from the center to the minimum film thickness
C_p	Radial Pad Clearance	$C_p = R_p - R_j$
C_b	Radial Bearing Clearance	$C_b = R_b - R_j$
M_p	Pad Preload	$M_p = \frac{C_p - C_b}{C_p}$
θ	Coordinate angle	Angular coordinate from the leading edge of the pad
θ_{min}	Angle to Minimum Clearance	Denotes the angular position of the minimum clearance from the leading edge of the pad for a centered journal
θ_L	Pad Load Orientation	Angular displacement from the leading edge of pad to location of load vector
α	Pad Offset	Denotes the position of the minimum clearance from the leading edge of the pad for a centered journal as a percentage of the pad arc angle $\alpha = \frac{\theta_{min}}{\theta_{pad}}$

Rotor-bearing [K][C][M] Model

When journal amplitudes of motion are small and centered about an equilibrium position within the bearing, the fluid-film forces acting on the rotor can be linearized and approximated as a two-degree-of-freedom model of stiffness (K_{ij}), damping (C_{ij}), and virtual-mass (M_{ij}) coefficients, as shown in Figure 6.

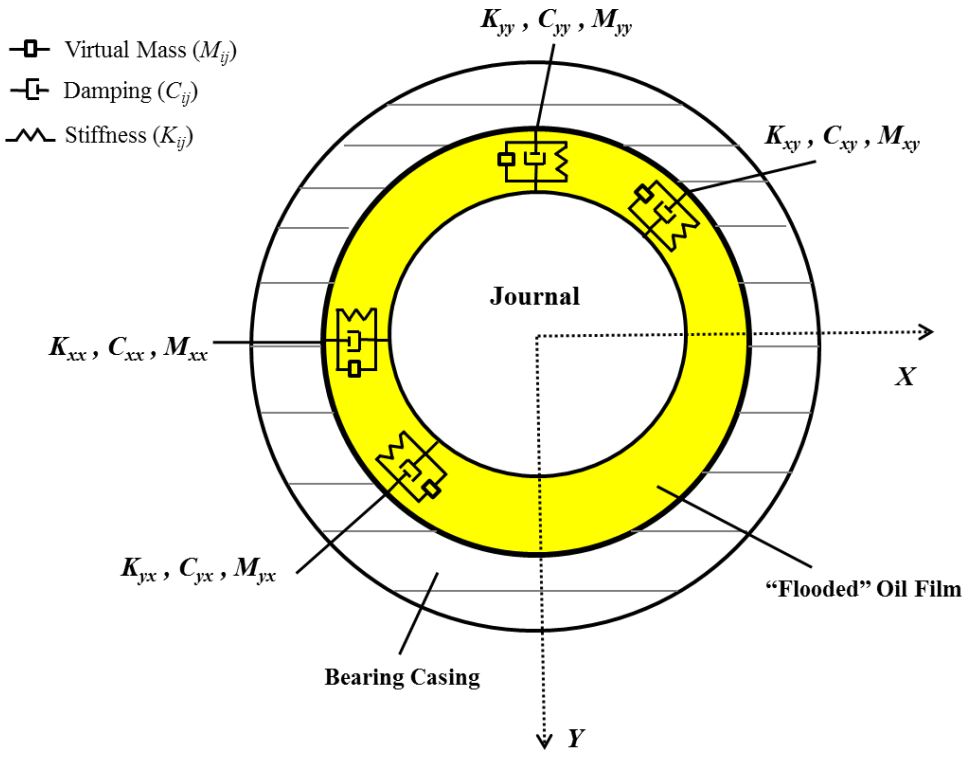

Figure 6. 2-DOF model of fluid-film bearing, adapted from [3]

The linearized equations of motion for the combined fluid-film forces, f_{bx} and f_{by}, are:

$$\begin{bmatrix} M_{xx} & M_{xy} \\ M_{yx} & M_{yy} \end{bmatrix} \begin{Bmatrix} \Delta\ddot{x} \\ \Delta\ddot{y} \end{Bmatrix} + \begin{bmatrix} C_{xx} & C_{xy} \\ C_{yx} & C_{yy} \end{bmatrix} \begin{Bmatrix} \Delta\dot{x} \\ \Delta\dot{y} \end{Bmatrix} + \begin{bmatrix} K_{xx} & K_{xy} \\ K_{yx} & K_{yy} \end{bmatrix} \begin{Bmatrix} \Delta x \\ \Delta y \end{Bmatrix} = - \begin{Bmatrix} f_{bx} \\ f_{by} \end{Bmatrix} \quad (5)$$

The twelve rotordynamic coefficients completely define the dynamic behavior of a journal-bearing system subjected to dynamic loads. The first subscript for each coefficient represents the direction of the fluid reaction force produced by a journal displacement in the direction of the second coefficient. The coefficients with the same two subscripts are called "direct" coefficients, while the coefficients with different subscripts are called "cross-coupled" coefficients. Generally, lower direct-damping coefficients and higher cross-coupled stiffness coefficients with different signs correspond to higher destabilizing forces [1].

The direct stiffness coefficients of a fluid-film bearing largely define the critical speeds of the rotor they support. A larger direct stiffness in the loaded direction generally yields higher critical speeds. A smaller direct stiffness in the loaded direction generally yields lower critical speeds. As a secondary effect, a smaller direct stiffness can help reduce the response amplitude when traversing critical speeds, by increasing the effectiveness of available damping. Additionally, stiffness orthotropy, defined as the difference in the two direct stiffness coefficients, can help produce a split critical speed. A split critical speed can be useful in shifting a critical speed out of the operating speed range [4].

An unloaded rotor supported on plain journal bearings is subject to oil whirl, where the rotor precesses at a frequency equal to approximately one-half the rotor spin speed. Both horizontal and vertical machines supported on most fixed-arc bearings are subject to oil-whip instabilities, where the rotor precesses at a frequency that is approximately equal to the first rotor critical speed. Oil-whip typically occurs at a speed equal to twice the first critical speed. The oil-whip precession frequency does not

change with increases in speed. The ratio of a rotor's first critical speed to the rotor onset speed of instability (OSI) equals the whirl-frequency ratio (WFR). Lund [5] derived the formula for the WFR as a function of the dimensionless stiffness and damping coefficients:

$$WFR^2 = \frac{(k_{eq} - k_{xx})(k_{eq} - k_{yy}) - k_{xy}k_{yx}}{c_{xx}c_{yy} - c_{xy}c_{yx}}, \text{ where,} \tag{6}$$

$$k_{eq} = \frac{(k_{xx}c_{yy} + k_{yy}c_{xx} - c_{yx}k_{xy} - c_{xy}k_{yx})}{\left(c_{xx} + c_{yy}\right)} \tag{7}$$

$$k_{ij} = K_{ij}\left(\frac{C_b}{F_s}\right) \tag{8a}$$

$$c_{ij} = C_{ij}\left(\frac{C_b\omega_s}{F_s}\right) \tag{8b}$$

k_{ij}, and c_{ij} are the dimensionless stiffness and damping coefficients, respectively. An alternative formula for non-dimensionalizing the stiffness coefficients is presented later.

Three-Lobe Bearings in Vertical Machines

Vertical-application bearings refer to those which generally carry minimal radial static loads, as the rotor weight is carried axially. As stated earlier, a radial static load on a bearing produces a journal eccentricity, a converging-diverging oil wedge, and thus a direct static stiffness. Because a vertical machine operating on plain journal bearings lacks an equilibrium journal eccentricity, the machine is nearly always subject to oil-whirl, where the rotor precesses at approximately 50% of the running speed. In the absence of a radial static load, the fixed-arc bearing designer must rely on preload and offset to generate the necessary direct static stiffness. Without either preload or a radial static load, the rotor will theoretically have no SEP and will therefore produce no radial

static stiffness in the centered position. Thus, a vertical machine running on plain journal bearings is inherently subject to oil-whirl [6].

Leader [6] examined a vertical sulfur pump experiencing subsynchronous vibrations due to "sulfur whirl" in its plain bushings. The subsynchronous whirl frequency was equal to nearly half the running speed and corresponded closely with the first rotor critical speed. To resolve this problem, the plain bushings were replaced with 100% offset, 0.7 preload, three-lobe bearings to maximize the direct stiffness from the bearings. By using three symmetric lobes with a 100% offset, the bearings are able to generate enough opposing pressure from each pad to produce a large centering force. This pressure generation is illustrated in Figure 7. This design change increased the predicted K_{xx} and K_{yy} coefficients by a factor of 27, reduced the predicted K_{xy} and K_{yx} coefficients by 70%, and raised the predicted first critical speed of the rotor beyond the operating speed range. Using Leader's published rotordynamic coefficients, the predicted WFR of this bearing is 0.17.

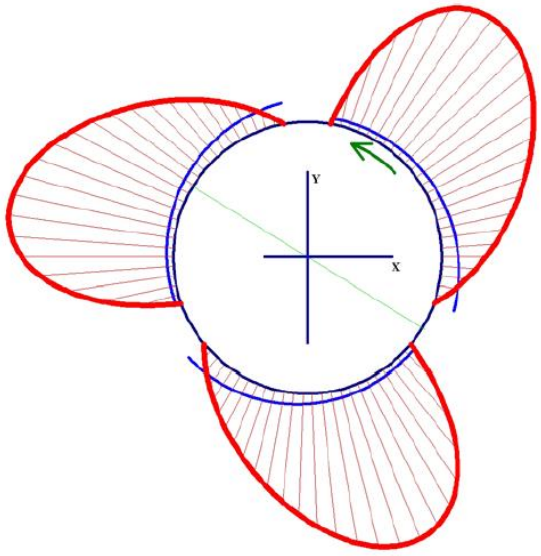

Figure 7. Predicted pressure profile of Leader's vertical-application three-lobe bearing, Leader [6]

Three-Lobe Bearing Types

Three-lobe bearings are classified by their geometries. Some major three-lobe bearing geometries are presented in Figure 8.

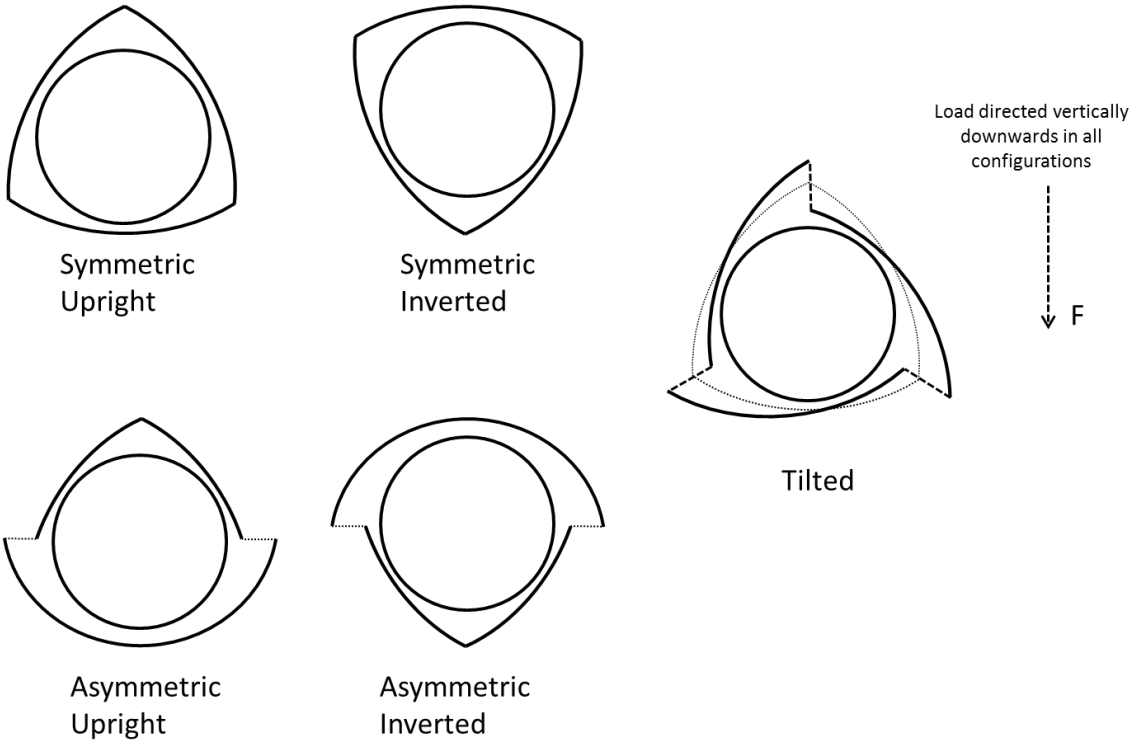

Figure 8. Common three-lobe bearing geometries

A symmetric three-lobe bearing is one in which all three lobes are of equal arc-length, while an asymmetric three-lobe bearing has pads with different arc-lengths. An

upright three-lobe bearing is a 50% offset bearing in which the radial static load is directed through the center of the pad, while an inverted three-lobe bearing is a 50% offset bearing in which the radial static load is directed through the center of the oil groove.

A *tilted* or *offset* three-lobe bearing is essentially a positively preloaded bearing with an offset greater than 50%. Relatively, little measured data exist for this configuration. Garner et al. [7] predict and compare the dynamic coefficients of various profile bore bearings and state that offset three-lobe bearings display improved stability, in terms of cross-coupled stiffnesses and direct damping, compared to the traditional symmetric three-lobe bearing. Additionally, they predict that the offset three-lobe bearing configuration has larger direct stiffness coefficients than the symmetric three-lobe bearing. Their analysis, however, was based on a single offset configuration (60% offset).

Statement of Work

As stated earlier, very little measured data exist for the offset three-lobe configuration relative to the symmetric upright and symmetric inverted configurations. This thesis aims to complement the work that has been performed on the offset three-lobe bearing configuration. Offset three-lobe bearings in this study are considered in two scenarios: (1) horizontal-application with a variable static load direction and (2) vertical-application with zero and very light loads.

The four primary objectives of this thesis are detailed below.

(1) The first part of this study examines the effect of varying the radial static load direction on the static and dynamic performance of a 0.52 preload, 70% offset horizontal-application three-lobe bearing. Eight load orientations are tested, detailed in the Test Procedure section. This part of the study aims to

answer the questions: (1) "Is the offset three-lobe configuration a good choice when the radial static load vector represents an unknown variable?" and (2) "Can the offset three-lobe configuration be oriented advantageously with a known load direction?" From a stability viewpoint, the most "advantageous" load orientation is one that features the lowest WFR, smallest cross-coupled stiffness coefficients, and largest direct damping coefficients. Either the highest or lowest direct stiffness coefficients could also be considered advantageous depending on whether the system designer chooses to shift a critical speed up or down. The load orientation which features the highest stiffness orthotropy could also be considered advantageous, since stiffness orthotropy can be used to split a critical speed [4], as well as enhance stability.

(2) The second part of this study examines the effect of using a 100% offset, 0.64 preload three-lobe bearing on the dynamic performance of a vertical machine. As noted earlier, plain journal bearings are unstable in vertical applications due to a lack of centering forces. Leader [6] used a three-lobe bearing with a 100% offset and 0.7 preload to increase the bearing direct stiffness (centering force) and stabilize a vertical pump. He reported rotordynamic coefficients that produce a 0.17 WFR for this bearing. A bearing geometrically similar to Leader's is tested, and its rotordynamic coefficients and WFR are examined.

(3) For both bearings, measurements are compared to predictions calculated from XL_JB_PRESS_DAM, part of the XLTRC^2 Rotordynamics Suite. This prediction tool is explained later.

(4) Finally, the measured K_{xx}, K_{yy}, and WFR for the vertical-application bearing are compared to those of the horizontal-application bearing to determine what, if any, advantage exists for using the 100% offset vertical-application bearing. Furthermore, Garner et al. [7] predicted that increasing the offset of a three-lobe bearing from 50% to 60% increases direct stiffness and enhances dynamic stability (by reducing $|K_{xy}|$ and $|K_{yx}|$, and increasing C_{xx} and C_{yy}).

This study compelements their work by comparing the direct stiffness and WFR of a 70% offset three-lobe bearing to a 100% offset three-lobe bearing.

Past Research

Various analytical studies and test programs have been carried out concerning both the determination of rotordynamic coefficients and the static-load performance of multi-lobe bearings. However, little work has been performed on the effects of static load direction sensitivity on three-lobe bearings. Many compilations of rotordynamic data for fixed-arc bearings fail to show any measured or predicted results for varying load orientations.

Lanes and Flack [8] analyzed and then tested the effects of bearing offset, preload, and load orientation on the stability of a rotor supported on three-lobe bearings. They tested a three-mass flexible rotor supported by seven different pairs of three-lobe bearings. Stability was evaluated on the basis of the observed OSI. The resulting stability maps showed that increasing preload generally increases OSI. The predictions showed that the dependence of stability on the static load orientation depends on the preload and offset. Varying the static load orientation was shown to affect the OSI of the system. The predicted and measured optimal load orientations for each set of preload and offset agreed to within 30° in most cases. At large offset values (α = 91%), the load orientation had minimal effect on stability. One bearing set (M_p=0.595/0.561, α=.505/.505) that was tested showed that load orientation had a particularly strong dependence on the OSI, with the 95^o load orientation having the highest OSI (9150 rpm) and the 20^o load orientation having the lowest OSI (5250 rpm). Another bearing set (M_p=0.747/0.723, α=.677/.677) initially showed that the OSI had virtually no dependence on load orientation (average OSI for all load orientations was 7500 rpm) when one of the pads of each bearing was tested. However, the bearings were rotated to test the other two pads of each bearing. When the tests were repeated for the other two

pads of each bearing, the OSI had a strong dependence on load orientation. For these tests, the 95^o load orientation had the lowest OSI (7700 rpm), and the 50^o load orientation had the highest OSI (8700 rpm). These conflicting results bring into question the repeatability of the measured data. The authors did not have an explanation for these conflicting outcomes.

Regarding predictions for multi-lobe bearings, Lanes and Flack [8] concluded that "bearing calculations are inaccurate for preloaded bearings" and that "more fundamental experimental pressure profile data are needed for this bearing type before further improvements in the theoretical predictions can be made". They noted that discrepancies between measurements and predictions are generally larger for multi-lobe bearings than pressure-dam bearings. In their study, discrepancies between measurements and predictions up to 45% for the OSI were reported, with the predicted OSI always being lower than the measured OSI.

Pettinato et al. [9] tested a .75 preload, 50% offset, 100^o pad arc angle, symmetric three-lobe bearing in three load orientations: 20^o, 50^o (load on pad), and -10^o (load between pad). The static load was applied along the *y*- direction. The -10^o (load directed into the oil groove) load orientation case showed the highest direct stiffness and direct damping coefficients orthogonal to the load (K_{xx} and C_{xx}) and the lowest direct stiffness and damping coefficients parallel to the load (K_{yy} and C_{yy}). The other two orientations had similar stiffness and damping coefficients, with the 50^o case having a slightly higher K_{yy} and C_{yy}, and the lowest K_{xx} and C_{xx}. They state that "the dynamic coefficients trended differently depending on load orientation", but give no specific conclusions as to which of the three load orientations are better for stability.

Mehta et al. [10] analyzed the effect of load orientation on the OSI of a flexible rotor supported by 0.5 preload, 50% offset three-lobe bearings with a preset eccentricity ratio of 0.4. They analyzed load orientations ranging from 20^o to 80^o of a 100^o arc angle pad. The 50^o load orientation was considered the nominal load direction. Their analysis showed that as the load orientation gets closer to 80^o, the OSI marginally decreases from

that of the nominal load orientation. As the load orientation gets closer to 20^o, the OSI significantly increases from that of the nominal load orientation. When the load orientation is below approximately 25^o, the OSI asymptotically increases. This implies that the WFR is zero for load orientations below approximately 25^o. This also implies that WFR increases with increasing load orientation.

The author notes the following deficiencies in the literature published to date on three-lobe bearing geometries:

(1). Comparatively little work has been performed on the offset three-lobe configuration. Most work focuses on the symmetric, upright three-lobe bearing.

(2). Most previous load orientation studies focus on dynamic data, in terms of rotor OSI and rotordynamic coefficients. Few papers discuss the effects of load orientation on static eccentricity, pad metal temperatures, and WFR.

(3). Few actual trends concerning load orientation sensitivity are found in the literature. Most studies (both analytical studies and test programs) conclude that load orientation has an effect on rotordynamic coefficients, but do not show concrete trends, in terms of WFRs, rotordynamic coefficients, SEP, or pad metal temperatures. Mehta et al. [10] remains the only study to date to predict any concrete trends regarding load orientation sensitivity of a three-lobe bearing.

(4). Few papers discuss the design of multi-lobe bearings for vertical (light load/no load) applications.

Appendix C contains a list of other relevant literature not presented in this section.

Prediction Tool

Predictions for both bearings are run using XL_JB_PRESS_DAM, part of the XLTRC^2 Rotordynamics Suite. A screenshot showing the input/output parameters for the program is shown in Figure 9. The program takes geometric input data in the form of pad preload, pad offset, pad clearance, bearing diameter, rotor diameter, and the angle of the leading edge of one of the pads relative to a fixed coordinate system. Additionally, the supply pressure, supply temperature, and properties of the lubricant are input. Measured hot (when available) and cold clearance values were used for predictions and compared to all measured data. The Haussen thermohydrodynamic model was used to estimate bearing temperature increases, as this is generally regarded as an accurate thermal convective model for laminar flows through a cylindrical geometry. The Haussen thermohydrodynamic model assumes fully developed laminar flow and a thermally-developing constant wall temperature [11]. The program uses the finite-difference method to evaluate a coupled Reynolds Equation and Haussen thermohydrodynamic model using the provided inputs to predict SEP, maximum temperature increases, and the twelve rotordynamic coefficients.

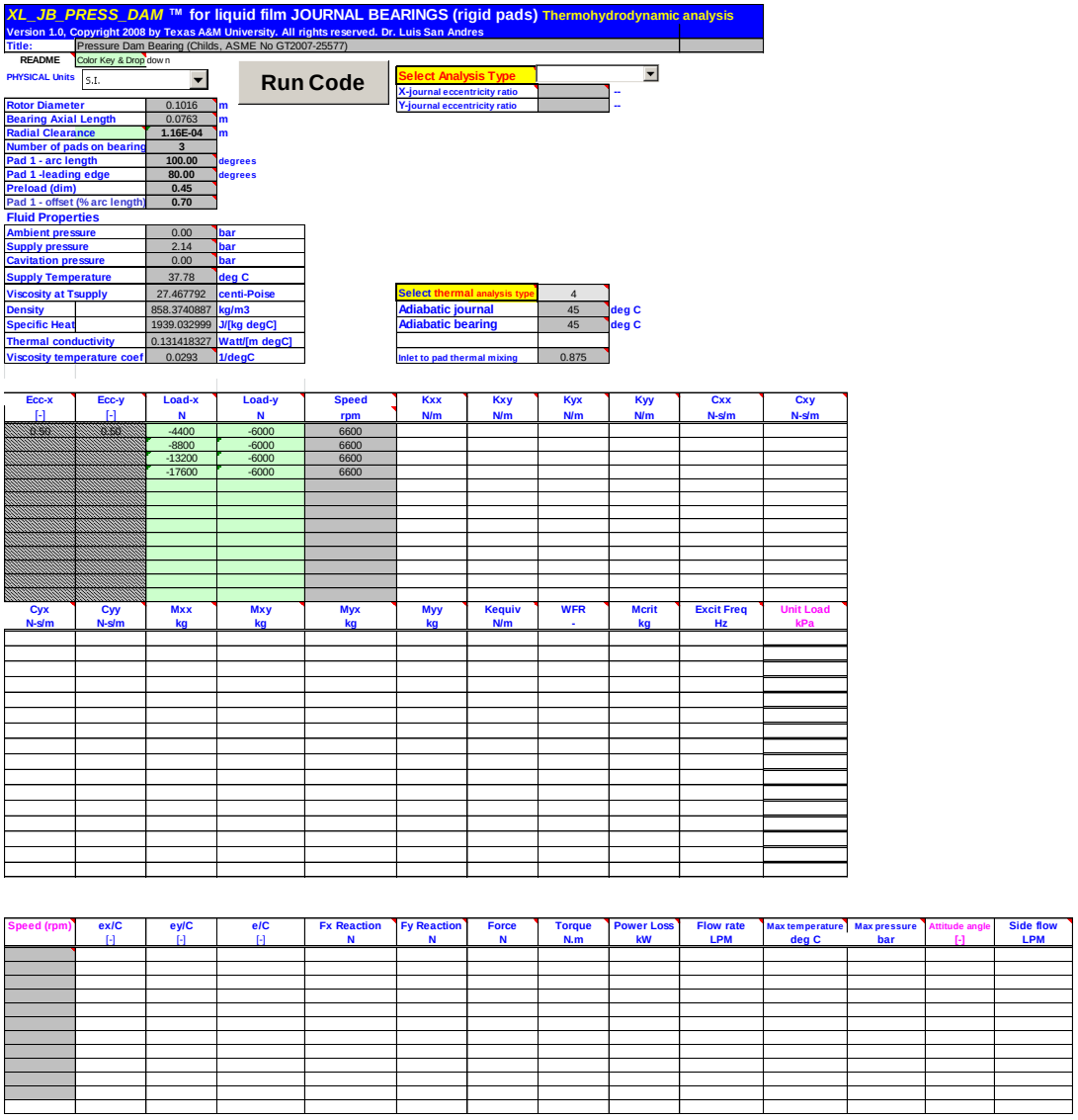

Figure 9. Screenshot of input/output parameters for XL_JB_PRESS_DAM program

TEST RIG

Figure 10 shows an overview of the test rig. Kaul [12] designed this test rig to measure rotordynamic characteristics of floating-ring bushing seals. The test rig has been used to test fluid-film bearings, as described by Childs et al. [13]. The rig consists of the test rotor supported on ball bearings, the test bearing/housing assembly, a static loader, hydraulic shakers, an air-drive turbine, an oil delivery system, and supporting instrumentation.

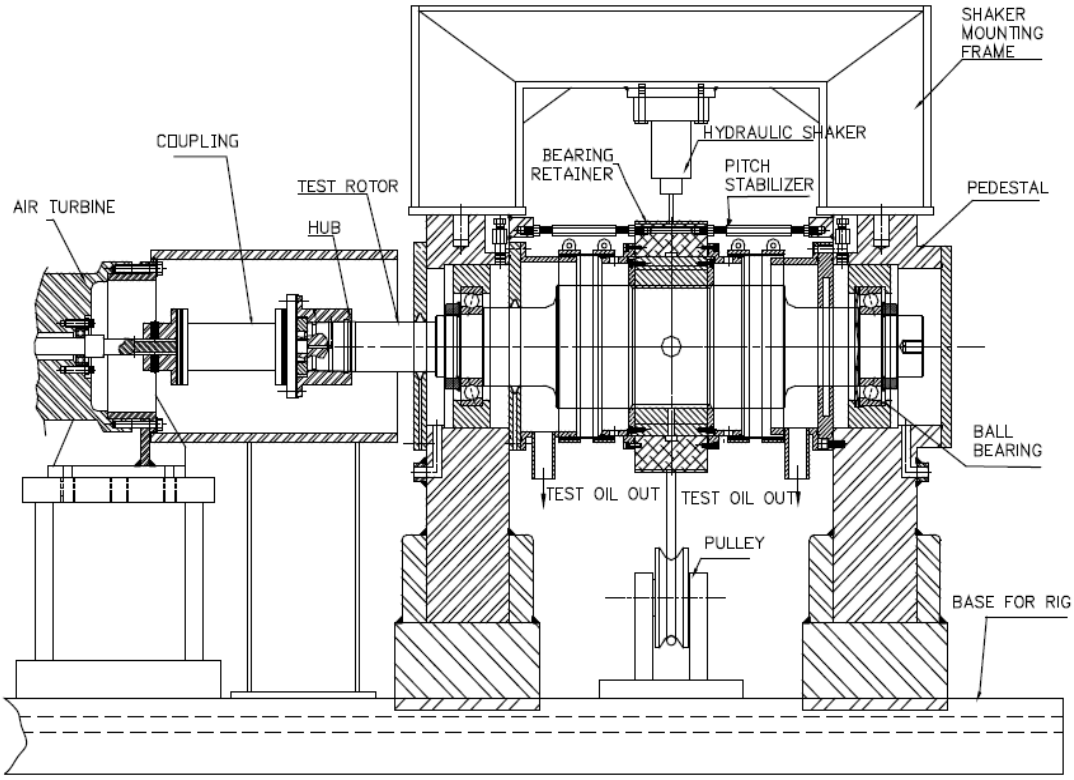

Figure 10. Schematic of "floating" bearing test rig [12]

The rig follows the "floating" bearing design first described by Glienicke [14]. The rotor is supported on a steel frame by hybrid-ceramic, angular-contact ball bearings that are lubricated by an oil-mist system. The test bearing is contained within a bearing housing, supported by hydraulic loaders, as described later in this section. The diameter of the test rotor at the bearing (test journal diameter) is 101.592 millimeters at room temperature. A buffer-seal keeps the oil-mist from escaping towards the air turbine, while two buffer-seals keep the mist from entering the oil discharge chambers and test journal.

An air turbine drives the shaft with a maximum power output of approximately 65 kW and a maximum rotational speed of approximately 18,000 rpm. The air turbine is connected to the rotor hub through a high-speed, flexible disc coupling.

ISO VG 32 oil is supplied to the test bearing from an oil supply tank. The oil system can deliver up to 75 liters per minute. The oil discharges axially from the test bearing through two rubber gasket strips and two retaining cartridges secured to the air buffer seals. The discharged oil enters a sump tank through six outlet hoses connected to the bottom of the retaining cartridges. A heat exchanger and pneumatically-controlled valves are used to control the temperature of the supply tank.

A pneumatic static loader loads the bearing with a maximum force of approximately 22,240 N (5000 lbf). The static load is always applied in the *y*- direction. The *x*- direction is always orthogonal to the static load. Dynamic excitation is applied to the bearing from hydraulic shakers in both the *x*- and *y*- directions as shown in Figure 11. The hydraulic shakers can also apply static loads which are used to center the rotor relative to the stator prior to testing. The "*x*-shaker" can apply a maximum tensile or compressive load of 4448 N (1,000 lbf), and the "*y*-shaker" can apply a maximum tensile load of 4448 N (1,000 lbf) and a maximum compressive load of 11,120 N (2,500 lbf). Both shakers can provide excitation frequencies to 1,000 Hz.

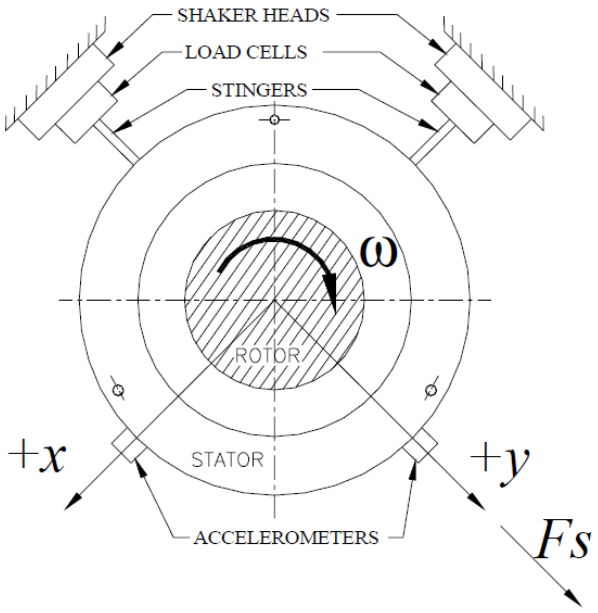

Figure 11. Loading configuration viewed from non-drive end [12]

As shown in Figure 11, the stator is attached to the hydraulic shakers through simple bar elements called stingers. Load cells between the stingers and shaker heads measure the applied loads output from the shakers. As shown in Figure 12, the static loader is attached to the stator through a yoke and spring assembly, which helps keep the directed load vector constant. A load cell located between the static loader and the yoke measures the applied static load.

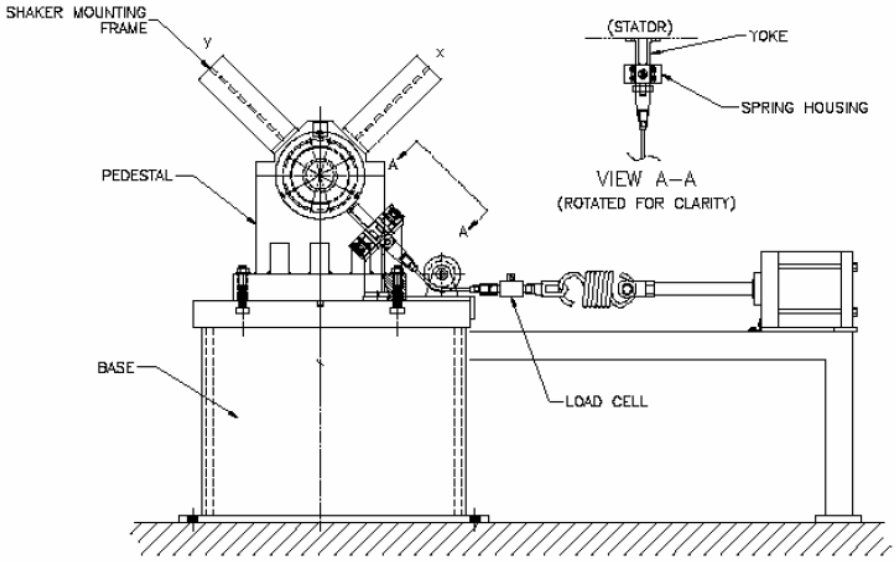

Figure 12. Schematic of the test rig showing static loader assembly [12]

The bearing is pressed into the housing prior to installing the complete stator onto the test rig. Care is taken to avoid bearing crush. Pitch stabilizers attach the bearing housing to the steel frame, aligning the test bearing housing around the rotor.

Instrumentation

Table 2 summarizes all of the instrumentation used for this study. The test bearing housing holds much of the instrumentation. Two non-contacting eddy current proximity probes are located on each end of the bearing housing along both excitation directions to measure relative motion between the rotor and test bearing. Piezoelectric accelerometers are located near the axial center-plane of the stator, one aligned along each excitation direction. Three thermocouples are located circumferentially around the inner diameter of the pads of the test bearing. Each pad contains one thermocouple near the trailing edge of the pad. These are shown and discussed in a later section.

Thermocouples are placed near the oil inlet and oil outlet lines attached to the stator to measure the inlet and outlet oil temperatures. A tachometer located on the non-drive end of the test rig measures the rotational phase and speed of the rotor. Three pressure transducers measure the stator inlet and outlet pressures of the oil.

Table 2. Instrumentation Used on the Test Rig

Application	Instrumentation (quantity)	Location	Measurement Obtained
Operational	Thermocouples (2)	Ball Bearings (2)	Temperature
	Thermocouples (2)	Main Tank (1) and Sump Tank (1)	Temperature
	Fiber Optic Displacement Sensor	Air Turbine (Near Coupling Attachment)	Vibration near Coupling
	Pressure Gauges (3)	In the Lubrimate® System	Oil Mist Pressure
Test Data	Load Cells (2)	Hydraulic Shakers	Static and Dynamic Force Output
	Load Cell (1)	Static Loader	Static Force Output
	Eddy Current Proximity Probes (4)	Top of Stator (two on Drive End, two on Non-Drive End)	Relative Displacement of Stator from Rotor
	Accelerometers (2)	Top of Stator (one along each excitation direction)	Absolute Acceleration of Stator
	Pressure Transducers (3)	Top of Stator (1), Bottom of Stator (2)	Stator Inlet Pressure
	Thermocouples (5)	Near Inner Diameter on Drive End of Bearing Pads (3); At inlet and outlet oil ports	Pad Temperatures; Inlet and Outlet Oil Temperatures
	Tachometer	Non-Drive End of Rotor	Speed (Angular Displacement)

Horizontal-Application Bearing Description

The horizontal-application bearing tested is an offset three-lobe configuration with 70% offset and a 0.52 preload. The bearing specifications are given in Table 3. Seven load orientations (θ_L = 0°, 20°, 30°, 40°, 80°, 90°, and 100°) were originally tested using ISO VG 32 oil, with an oil inlet temperature of 37.8°C. Several years later, the 60° load orientation was tested to help create a more complete data set. For logistical reasons, the 60° load orientation was tested with a different oil (ISO VG 46), and the oil inlet temperature was altered to keep the same inlet oil viscosity as that of ISO VG 32 at 37.8°C.

Table 3. Specifications for Horizontal-Application Three-Lobe Bearing

Manufacturer	KMC Bearings
Number of lobes	3
Loading Configuration	0°, 20°, 30°, 40°, 60°, 80°, 90°, and 100° from the leading edge
Bearing (Bore) Diameter	101.74 mm (4.0057 inches)
Pad Arc Angle	100° (20° groove)
Pad Axial Length	76.30 mm (3.005 inches)
Preload	0.52
Radial Pad Clearance	0.133mm (0.00527 inches)
Measured Radial Bearing Cold Clearance	0.0637 mm (0.00251 inches)
Offset	70%
Nominal Inlet Oil Temperature	50.0°C (122°F) for 60° load orientation 37.8°C (100°F) for remaining load orientations
Lubricant Used	ISO VG 46 for 60° load orientation ISO VG 32 for remaining load orientations
Rotor Diameter	101.59 mm (3.9997 inches)

Figure 13 shows a side view of the bearing as viewed from the drive end. Three thermocouples are machined at the trailing edge of the pad. The thermocouples are drilled to the axial mid-plane of the bearing.

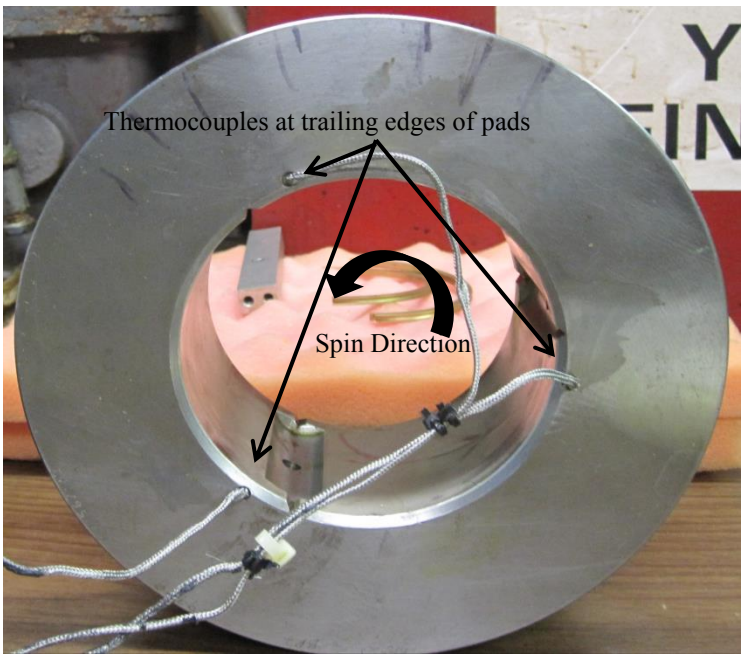

Figure 13. Location of thermocouples on horizontal-application bearing

Vertical-Application Bearing Description

The second bearing tested is a 0.64 preload, 100% offset vertical-application bearing. The bearing specifications for the vertical-application bearing are given in Table 4. The pad arc angle is 100^{o}. For this bearing, the no-load condition is tested, as well as light static loads applied at the trailing edge of the pad. This means that $\theta_L = 100^{o}$ for the vertical-application bearing.

Table 4. Vertical-Application Bearing Specifications

Manufacturer	KMC Bearings
Number of lobes	3
Loading Configuration	100° from the leading edge
Bearing (Bore) Diameter	101.74 mm (4.0057 inches)
Pad Arc Angle	100°
Pad Axial Length	76.3 mm (3.005 inches)
Preload	0.64
Radial Pad Clearance	0.191mm (0.00755 inches)
Measured Radial Bearing Cold Clearance	0.0693 mm (0.00273 inches)
Offset	100%
Nominal Inlet Oil Temperature	37.8°C (100°F)
Lubricant Used	ISO VG 32
Rotor Diameter	101.59 mm (3.9997 inches)

TEST PROCEDURE

The test procedure aims to produce sound static and dynamic measurements. Static data include the hot and cold radial bearing clearance measurements, static equilibrium positions, and pad metal temperatures. Dynamic data include the measured dynamic stiffness, the rotordynamic coefficients curve-fit from the measured dynamic-stiffness coefficient data, and calculated whirl-frequency ratio.

Test Matrix

The controlled test variables for the horizontal-application bearing study are the static load vector (both magnitude and direction), rotational speed, and oil flow rate. The test matrix in Table 5 summarizes the different combinations of unit load magnitude, speed, and flow rate. As speed increases, the oil outlet flow rate increases, and higher flow rates are required to maintain a flooded bearing. Note the flow rate only varies with the speed, and all loads tested at a single speed were tested with the same flow rate. The majority of this test matrix was repeated for each of the eight load orientations illustrated in Figure 14.

For the 60^{o} load orientation, the 0 kPa and 13200 rpm cases were not tested. Additionally, static data was not taken for the 60^{o} load orientation.

Table 5. Horizontal-Application Bearing Test Matrix

	Nominal Static Unit Load (kpa)				
Speed (RPM), Flow rate (LPM)	**0,0**	**575**	**1149**	**1723**	**2298**
6750, 24.61	Z	X	X	X	X
9000, 26.50	Z	X	X	X	X
10800, 28.39	Z	X	X	X	X
13200, 30.28	Z	Z	Z	Z	Z

X=tested at 0^o, 20^o, 30^o, 40^o, 60^o, 80^o, 90^o, and 100^o load orientations
Z=tested at 0^o, 20^o, 30^o, 40^o, 80^o, 90^o, and 100^o load orientations only

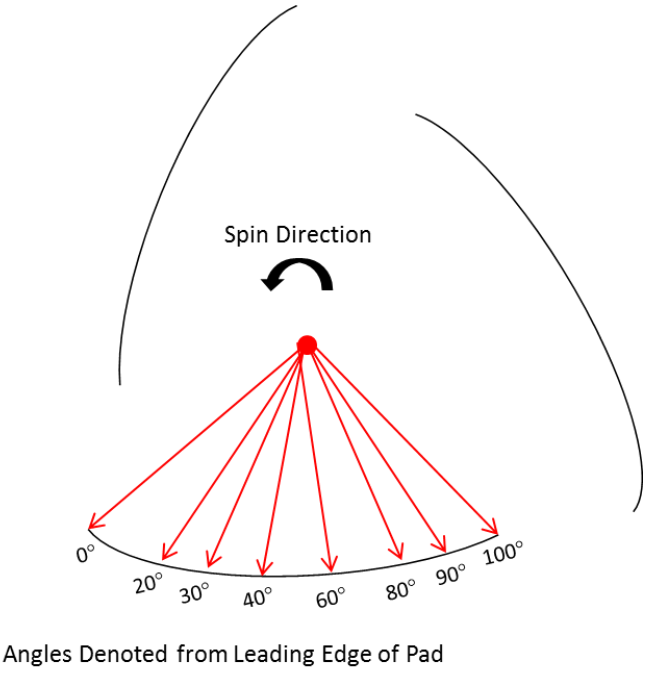

Figure 14. Eight different static load orientations tested for the horizontal-application bearing (pad arc angle θ_{pad}= 100°)

Table 6 shows the test matrix for the vertical-application bearing study. This bearing was tested at four different speeds, with zero load and two light loads. As previously discussed, the load orientation for this bearing is fixed at 100^{o}.

Table 6. Vertical-Application Bearing Test Matrix

	Nominal Static Load (kpa)		
Speed (RPM), Flow rate (LPM)	**0**	**58**	**117**
2000, 17.04	X	X	X
4400, 18.93	X	X	X
6750, 20.82	X	X	X
9000, 22.71	X	X	X

Static Data

Prior to running any tests, a cold-clearance measurement of the bearing is made by applying a small, slowly-rotating force to the bearing housing using the hydraulic shakers. The rotating force causes the bearing to trace the clearance profile between the test bearing and journal, while the proximity probes record the relative displacement of the bearing from the rotor. The average radial distance of this cold clearance is calculated by breaking the measurements up into three sections and iteratively solving for the minimum and maximum distances from each pad to the center of the clearance profile.

The measured cold clearance for the horizontal-application bearing (.52 preload, 70% offset) is presented in Figure 15 for the 0^{o} load orientation. The fitted clearance is

plotted over the same figure. The measured cold clearance for the horizontal-application bearing is 64 microns.

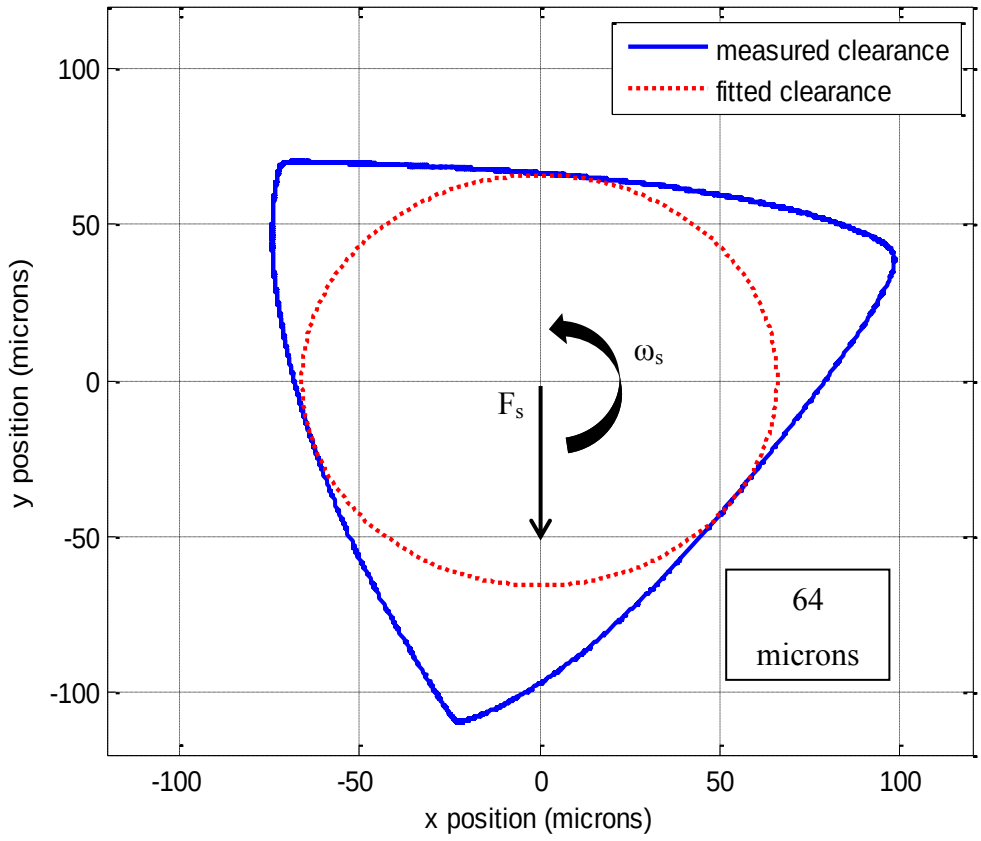

Figure 15. Measured cold clearance of horizontal-application bearing (0^o load orientation)

The measured cold clearance for the vertical-application bearing (.64 preload, 100% offset) is shown in Figure 16. The measured cold clearance for the vertical-application bearing is 69 microns.

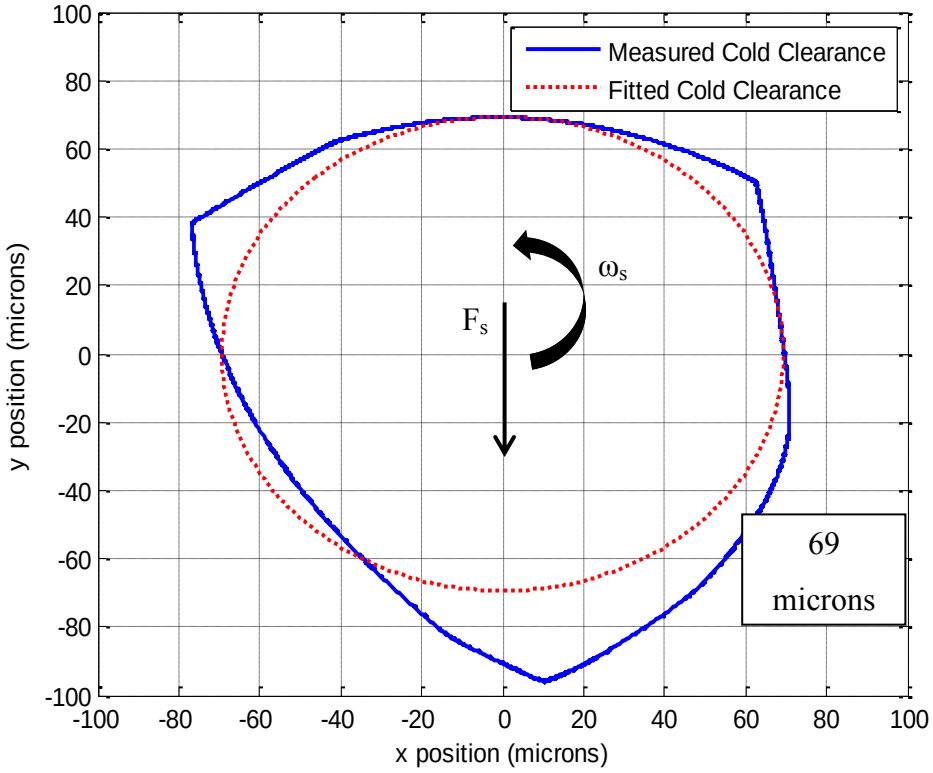

Figure 16. Measured and fitted vertical-application bearing cold clearance

A hot-clearance test was also obtained by running the rotor up to the maximum speed and radial static load, waiting for the bearing to achieve thermal equilibrium, removing the radial static load, spinning down the rotor to zero speed, and then quickly taking a clearance measurement with the bearing at the hotter temperature. This procedure is similar to that first described by Wilkes [15].

For the horizontal-application bearing, only one hot-clearance measurement was taken for the 0^o load orientation. The measured and fitted hot-clearance plots for the horizontal-application bearing are provided in Figure 17 for the 0^o load orientation. This

hot-clearance measurement was taken after running the rotor to 13.2 krpm with a 2298 kPa static load prior to shutting down the static loader and air turbine. This was the only orientation for which a hot clearance measurement was taken. The measured hot clearance is 47 microns. This equates to roughly 73% of the measured cold clearance.

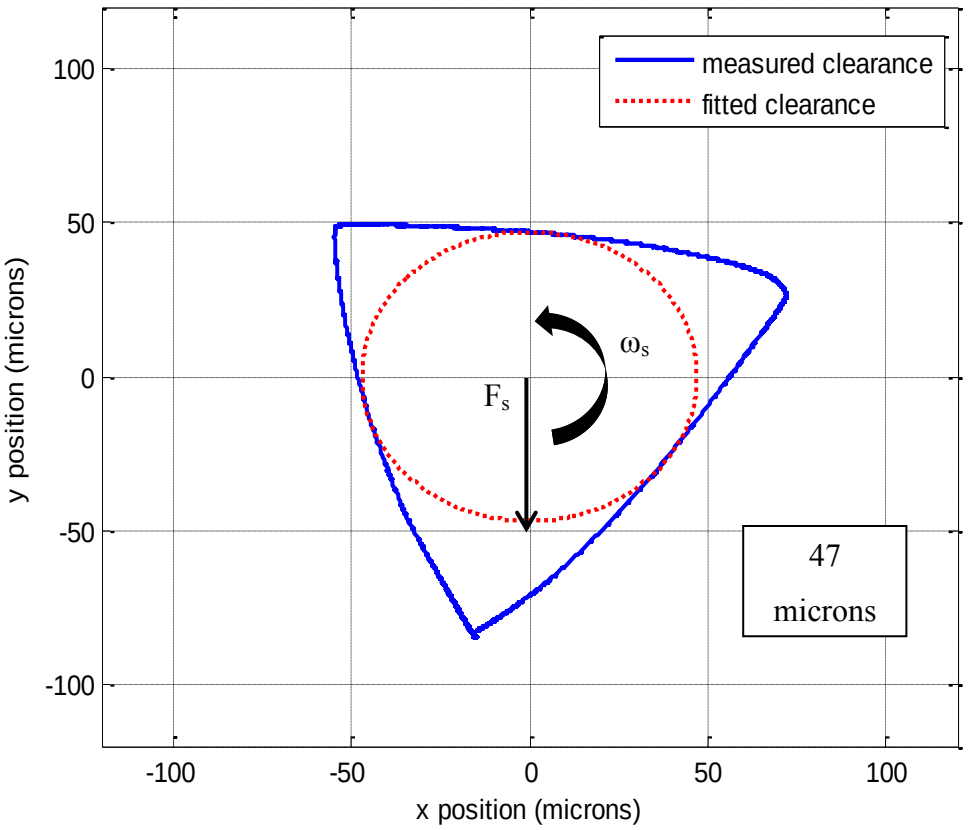

Figure 17. Measured hot clearance of horizontal-application bearing (0^o load orientation)

Also, for the vertical-application bearing (.64 preload, 100% offset), only one hot-clearance measurement was taken. The vertical-application bearing measured hot clearance is shown in Figure 18. The measured hot clearance is 57 microns. This hot-clearance measurement was taken after running the rotor to 9 krpm with a 117 kPa static load prior to shutting down the static loader and air turbine.

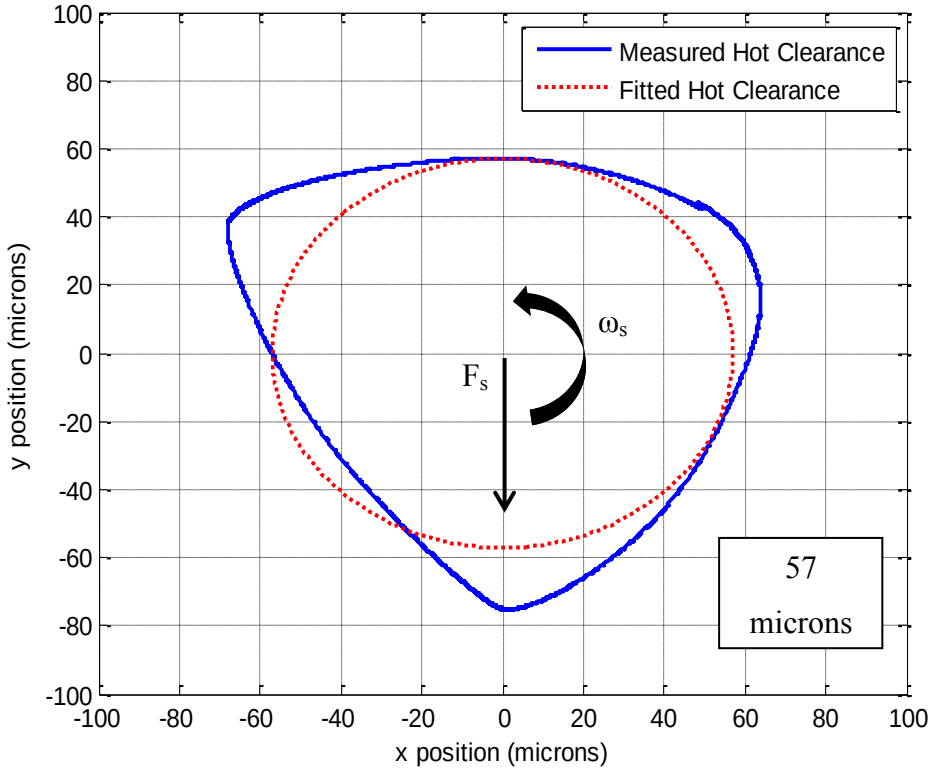

Figure 18. Measured and fitted vertical-application bearing hot clearance

The average cold clearance measurements can be interpreted as a "maximum operating clearance" and the average hot clearance measurements can be interpreted as a "minimum operating clearance". The effect of using the hot or cold clearance on

predictions is compared in later sections. Additionally, the effect of using the hot-clearance center location to determine the SEP of the no-load condition for the 0^o load orientation is examined in a later section.

A typical static test involves stepping through a set of static loads at a given constant speed and recording the SEP of the rotor within the bearing. These measurements are then reduced to produce SEP locus plots, which show the SEP of the journal within the bearing as a function of load at a constant speed. The dimensional eccentricity, non-dimensional eccentricity ratio, ε, and attitude angle can be calculated from the measured eccentricities in each direction, e_x and e_y, using:

$$e = \sqrt{e_x^2 + e_y^2} \tag{9}$$

$$\varepsilon = \frac{e}{C_b} \tag{10}$$

$$\varphi = \tan^{-1}\left(\frac{e_y}{e_x}\right) \tag{11}$$

Pad metal temperatures at each of the three pad thermocouple locations are also recorded during a static test. The j-type thermocouples have a measurement uncertainty of $\pm$2%. The measured maximum pad temperature increases are presented later.

Dynamic Data

The parameter identification model described by Childs and Hale [16] is used to determine the rotordynamic coefficients. The equations of motion for the stator under dynamic excitation are shown in Eq. (12), where M_s is the stator mass, f_i represents the components of the dynamic force applied to the stator in the direction of i, and f_{bi} represents the bearing reaction force components.

$$M_s \begin{Bmatrix} \ddot{x} \\ \ddot{y} \end{Bmatrix} = \begin{Bmatrix} f_x \\ f_y \end{Bmatrix} - \begin{Bmatrix} f_{bx} \\ f_{by} \end{Bmatrix} \tag{12}$$

Note that f_{bx} and f_{by} were defined earlier in Eq. (1).

Substituting Eq. (1) into Eq. (12) yields:

$$-\begin{Bmatrix} f_x - M_s\ddot{x} \\ f_y - M_s\ddot{y} \end{Bmatrix} = \begin{bmatrix} M_{xx} & M_{xy} \\ M_{yx} & M_{yy} \end{bmatrix} \begin{Bmatrix} \Delta\ddot{x} \\ \Delta\ddot{y} \end{Bmatrix} + \begin{bmatrix} C_{xx} & C_{xy} \\ C_{yx} & C_{yy} \end{bmatrix} \begin{Bmatrix} \Delta\dot{x} \\ \Delta\dot{y} \end{Bmatrix} + \begin{bmatrix} K_{xx} & K_{xy} \\ K_{yx} & K_{yy} \end{bmatrix} \begin{Bmatrix} \Delta x \\ \Delta y \end{Bmatrix} \tag{13}$$

Taking a Fast Fourier Transform (FFT) converts Eq. (13) from the time domain to the frequency domain, yielding:

$$-\begin{Bmatrix} \boldsymbol{F_x} - M_s \boldsymbol{A_x} \\ \boldsymbol{F_y} - M_s \boldsymbol{A_y} \end{Bmatrix} = \begin{bmatrix} M_{xx} & M_{xy} \\ M_{yx} & M_{yy} \end{bmatrix} \begin{Bmatrix} \boldsymbol{D_x} \\ \boldsymbol{D_y} \end{Bmatrix} (\boldsymbol{j}\Omega)^2 + \begin{bmatrix} C_{xx} & C_{xy} \\ C_{yx} & C_{yy} \end{bmatrix} \begin{Bmatrix} \boldsymbol{D_x} \\ \boldsymbol{D_y} \end{Bmatrix} (\boldsymbol{j}\Omega) + \begin{bmatrix} K_{xx} & K_{xy} \\ K_{yx} & K_{yy} \end{bmatrix} \begin{Bmatrix} \boldsymbol{D_x} \\ \boldsymbol{D_y} \end{Bmatrix} \tag{14}$$

$\boldsymbol{A_i}$ and $\boldsymbol{F_i}$ represent the components of the Fourier transforms of the absolute acceleration and dynamic force components in the *i*- direction, respectively. $\boldsymbol{D_x}$ and $\boldsymbol{D_y}$ represent the Fourier transforms of the relative displacement components between the stator and rotor, Ω represents the dynamic excitation frequency, and $\boldsymbol{j}$ represents the standard imaginary unit. All variables in Eq. (14) are measured other than the twelve rotordynamic coefficients. At this point, it becomes easier to simplify this equation by introducing the variable $\boldsymbol{H_{ij}}$, called the complex dynamic stiffness coefficients and defined by:

$$\boldsymbol{H_{ij}} = (K_{ij} - \Omega^2 M_{ij}) + \boldsymbol{j}\left(\Omega C_{ij}\right) \tag{15}$$

Substituting Eq. (15) into Eq. (14) yields:

$$-\begin{Bmatrix} \boldsymbol{F_x} - M_s \boldsymbol{A_x} \\ \boldsymbol{F_y} - M_s \boldsymbol{A_y} \end{Bmatrix} = \begin{bmatrix} \boldsymbol{H_{xx}} & \boldsymbol{H_{xy}} \\ \boldsymbol{H_{yx}} & \boldsymbol{H_{yy}} \end{bmatrix} \begin{Bmatrix} \boldsymbol{D_x} \\ \boldsymbol{D_y} \end{Bmatrix} \tag{16}$$

Eq. (16) provides two equations for four unknowns. By alternately exciting the rotor in both directions while simultaneously measuring relative motion in both directions, the frequency-domain equations of motion can be expanded into:

$$-\begin{bmatrix} \boldsymbol{F}_{xx} - M_s \boldsymbol{A}_{xx} & \boldsymbol{F}_{xy} - M_s \boldsymbol{A}_{xy} \\ \boldsymbol{F}_{yx} - M_s \boldsymbol{A}_{yx} & \boldsymbol{F}_{yy} - M_s \boldsymbol{A}_{yy} \end{bmatrix} = \begin{bmatrix} \boldsymbol{H}_{xx} & \boldsymbol{H}_{xy} \\ \boldsymbol{H}_{yx} & \boldsymbol{H}_{yy} \end{bmatrix} \begin{bmatrix} \boldsymbol{D}_{xx} & \boldsymbol{D}_{xy} \\ \boldsymbol{D}_{yx} & \boldsymbol{D}_{yy} \end{bmatrix} \tag{17}$$

Finally, Eq. (17) is rearranged to form:

$$\begin{bmatrix} \boldsymbol{H}_{xx} & \boldsymbol{H}_{xy} \\ \boldsymbol{H}_{yx} & \boldsymbol{H}_{yy} \end{bmatrix} = -\begin{bmatrix} \boldsymbol{F}_{xx} - M_s \boldsymbol{A}_{xx} & \boldsymbol{F}_{xy} - M_s \boldsymbol{A}_{xy} \\ \boldsymbol{F}_{yx} - M_s \boldsymbol{A}_{yx} & \boldsymbol{F}_{yy} - M_s \boldsymbol{A}_{yy} \end{bmatrix} \begin{bmatrix} \boldsymbol{D}_{xx} & \boldsymbol{D}_{xy} \\ \boldsymbol{D}_{yx} & \boldsymbol{D}_{yy} \end{bmatrix}^{-1} \tag{18}$$

Eq. (18) is arranged such that the unknowns are on the left-hand side and the measured quantities on the right-hand side. Hence, by measuring the stator mass, excitation force, absolute stator acceleration, and relative displacement vectors between the stator and rotor, the $\boldsymbol{H}_{ij}$ coefficients can be found.

A typical dynamic test involves sinusoidal excitation over a range of frequencies from 10 Hz to 350 Hz in 10 Hz increments using a multi-frequency (or dynamic) waveform. The actual frequencies tested are multiplied by a factor of 1,000/1,024 with the nominal frequencies to isolate certain frequencies from electrical noise. The dynamic waveform, which takes less than a second to execute, is applied to the stator 320 times along each direction. The relative displacement between the stator and the rotor, absolute acceleration of the stator, and dynamic force magnitude are recorded as previously described. The 320 sets of measurements along each axis are then broken into five groups of 64. Each of the five groups of data along one axis is combined with each of the five groups of data along the other axis to form a total of 25 complex dynamic stiffness matrices. The repeatability of the reported average values of these complex dynamic stiffnesses is based on a statistical analysis of these data. The direct and cross-coupled complex dynamic stiffnesses are then calculated and plotted against excitation frequency. Note that the complex dynamic stiffness is composed of both a real and imaginary part as shown in Eqs. (19) and (20), respectively.

$$Re(\boldsymbol{H_{ij}}) = (K_{ij} - \Omega^2 M_{ij}) \tag{19}$$

$$Im(\boldsymbol{H_{ij}}) = \boldsymbol{j}\left(\Omega C_{ij}\right) \tag{20}$$

The plot of the Re($\boldsymbol{H_{ij}}$) vs. Ω is curve fitted to a function of Ω^2, and the stiffness and virtual mass coefficients are determined as the coefficients of the curve-fitted function. For Re($\boldsymbol{H_{ij}}$) vs. Ω, a standard linear regression is applied on:

$$y = ax+b, \text{ where} \tag{21}$$

$$y=Re(\boldsymbol{H_{ij}})$$

$$a = -M_{ij}$$

$$x= \Omega^2$$

$$b = K_{ij}$$

Similarly, the imaginary part is curve-fitted as a standard linear function of Ω, and the damping coefficient is determined as the slope of this curve fit. For Im($\boldsymbol{H_{ij}}$) vs. Ω, a linear regression is applied on:

$$y = ax+b, \text{ where} \tag{22}$$

$$y=Im(\boldsymbol{H_{ij}})$$

$$a = C_{ij}$$

$$x= \Omega$$

$$b = C_{ij,o}$$

R^2 values are calculated for each of the curve-fits using standard linear regression theory. The uncertainties for each of the rotordynamic coefficients are calculated as the 95% confidence intervals (assuming a Gaussian distribution) of the coefficients of the linear regressions performed on the Re($\boldsymbol{H_{ij}}$) and Im($\boldsymbol{H_{ij}}$) vs. Ω.

A baseline measurement, $\boldsymbol{H}_{baseline}$, is taken to measure the dynamic coefficients of the system without oil in the bearing. This represents the complex dynamic stiffness of the test rig connection to the stator and is assumed to directly add to the test bearing complex dynamic stiffness to give the total measured complex dynamic stiffness, $\boldsymbol{H}_{measured}$. Therefore, the baseline measurement is subtracted from the test measurements to yield the test bearing complex dynamic stiffness:

$$\boldsymbol{H}_{ij} = \boldsymbol{H}_{measured} - \boldsymbol{H}_{baseline} \tag{23}$$

The baseline stiffness and damping is affected by all attachments from the stator to ground, including the oil inlet and outlet hoses, pitch stabilizers, static loader and instrumentation. The static loader has an especially large effect on the baseline complex dynamic stiffness, and as such, both an unloaded and loaded baseline measurement is taken to compensate for the unloaded and loaded test measurements, respectively. Typically, the baseline measurements are at least an order of magnitude lower than the test measurements. The total repeatability error from the dynamic stiffness measurements is defined by Eq. (24) and is graphically represented by error bars in the complex dynamic stiffness plots.

$$\Delta \boldsymbol{H}_{ij} = \sqrt{\left(\Delta \boldsymbol{H}_{ij,Test}\right)^2 + \left(\Delta \boldsymbol{H}_{ij,Baseline}\right)^2} \tag{24}$$

HORIZONTAL-APPLICATION BEARING STATIC RESULTS

Pad Metal Temperatures

Pad-metal-temperature-increases are calculated by taking the difference between the measured temperature increases at a given speed and load and subtracting the temperature measured at zero speed and zero load. The maximum pad-metal-temperature-increases are obtained from the highest difference measured from the three installed pad thermocouples. Each of the three thermocouples is located 90^o from the leading edge of the pad, drilled to the axial mid-plane, as shown earlier in Figure 13. Note, since there were only three thermocouples installed, the true maximum pad-metal-temperature-increases may differ from the reported values, as the complete temperature distribution around the bearing cannot be captured with only one thermocouple per pad. Predictions for the "no-load" condition were run using a 1.3 kPa load to represent a very light static load, since the numerical code used for predictions does not converge for values approaching zero.

Figure 19 shows the maximum pad-metal-temperature-increases vs. load orientation at 6750 rpm, and at three different unit loads. The 30^o and 90^o load orientations show the highest pad-metal-temperature-increases. It is unclear what causes these peaks for the 30^o and 90^o load orientations. The measurements show that the bearing is most sensitive to load orientation at 0 kPa. A 0 kPa, the maximum pad-metal-temperature-increases range from 14-26 ^{o}C, depending on load orientation. The measured-pad-temperature increases versus load-orientation approach a small range of values at the highest static load. At 2298 kPa, there is very little difference in the maximum pad-metal-temperature-increases between the different load orientations, with values ranging from 35-39 ^{o}C for all load orientations.

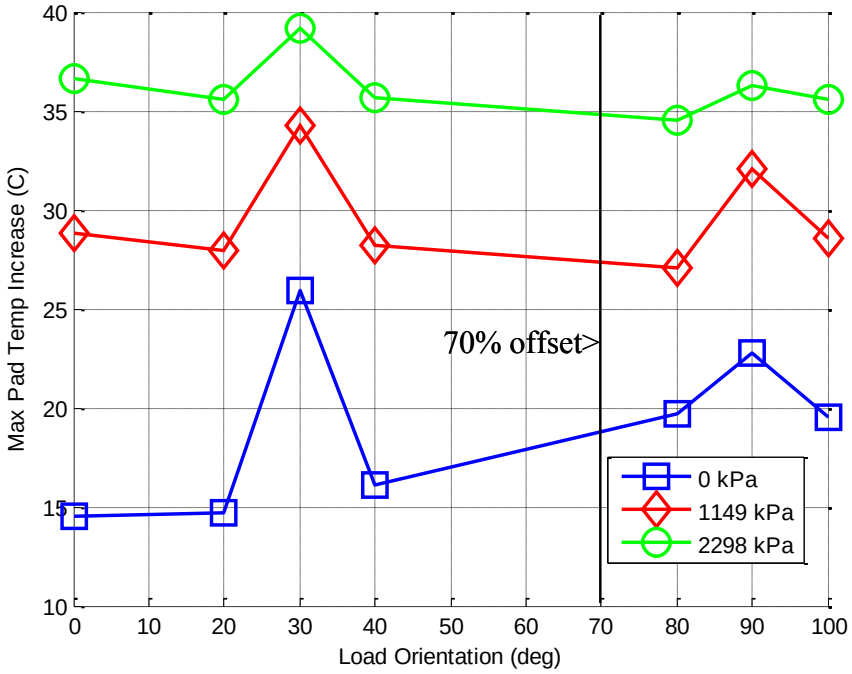

Figure 19. Maximum pad-metal-temperature-increases at 6750 rpm

Figure 20 shows the maximum-pad-metal-temperature-increases vs. load orientation at 13200 rpm, and at three different unit loads. Most of the observations cited above for Figure 19 apply to Figure 20. However, at 13200 rpm, the maximum-pad-metal-temperature-increases are significantly higher at all test points. At 0 kPa, the measurements range from 37-53 ^{o}C. At 2298 kPa, the measurements range from 63-69^{o}C.

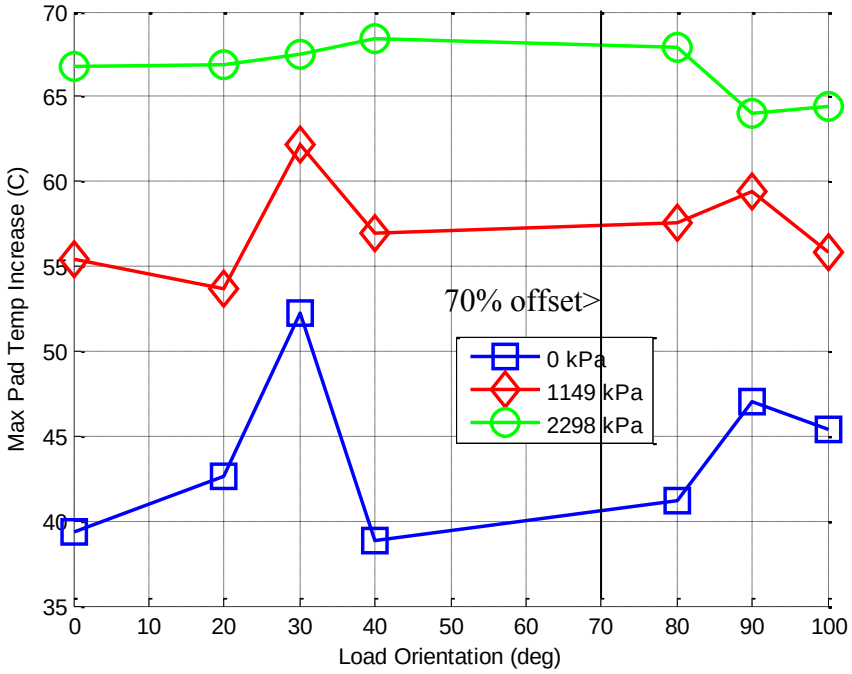

Figure 20. Maximum pad-metal-temperature-increases at 13200 rpm

As discussed above, the measured pad-temperature-increases versus load orientation approach a small range of values at the highest loads. Table 7 summarizes the maximum pad temperature increases at 2298 kPa for each speed.

Table 7. Maximum-Temperature-Increases at 2298 kPa for the Horizontal-Application Bearing

Speed (rpm)	Range of maximum-temperature increases at 2298 kPa for all load orientations (^{o}C)
6750	35-39
9000	44-49
10800	52-57
13200	63-69

Figure 21 shows the measured and predicted maximum-pad-metal-temperature-increases versus load orientation at 6750 rpm, for the 0 kPa and 2298 kPa test points. The "inlet to pad thermal mixing" constant was set to 0.8. This is the percentage of "hot" oil leaving the upstream pad and mixing with the fresh supply oil entering the downstream pad.

Using the different measured clearance values has a significant effect on the predictions. Generally speaking, using the hot clearance predicts larger maximum-pad-temperature increases than using the cold clearance. At 0 kPa, the predictions are constant versus load orientation. At 2298 kPa, the predictions show a slight variation, with the smallest pad-metal-temperature-increases occurring for the 80^{o} load orientation, and the largest pad-metal-temperature-increases occurring for the 0^{o} load orientation. At both 0 kPa and 2298 kPa, the predictions using the cold clearance give significantly better agreement with measurements than predictions using the hot clearance. This makes sense, as the true clearance is expected to be closer to the cold clearance at 6750 rpm.

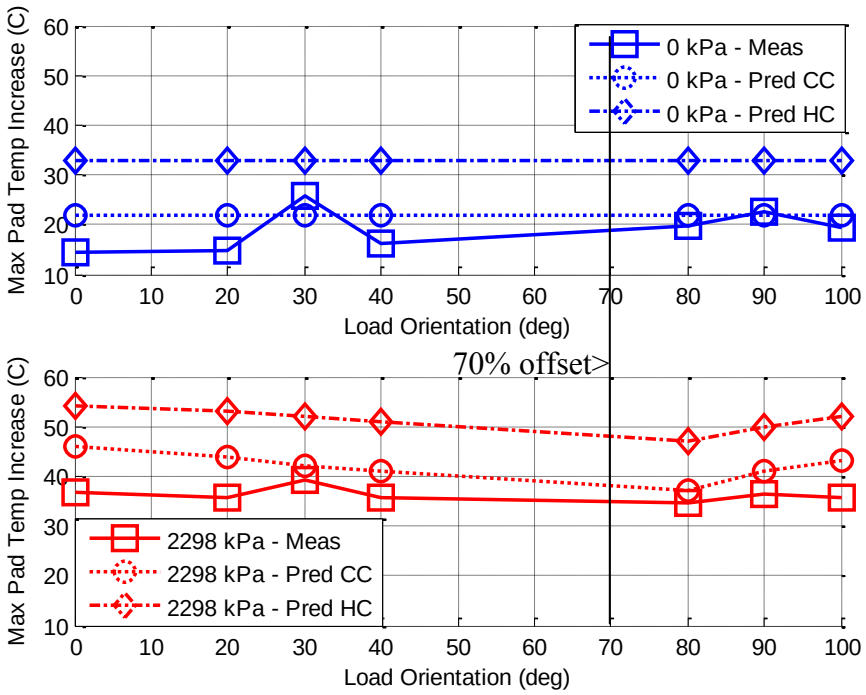

Figure 21. Measured and predicted maximum-pad-metal-temperature-increases at 6750 rpm, with 0 kPa (top) and 2298 kPa (bottom) loads

Figure 22 shows the measured and predicted maximum-pad-metal-temperature-increases versus load orientation at 13200 rpm, for the 0 kPa and 2298 kPa test points. At 0 kPa, the predictions using the hot clearance give better agreement with measurements at most load orientations. At 2298 kPa, the predictions using the hot clearance give significantly better agreement with measurements at all load orientations. This makes sense, as the true clearance is expected to be closer to the hot clearance at 13200 rpm.

A comparison of Figures 21 and 22 shows that, at 13200 rpm, the measured and predicted pad-temperature-increases are approximately 25°C-35°C larger than those at 6750 rpm.

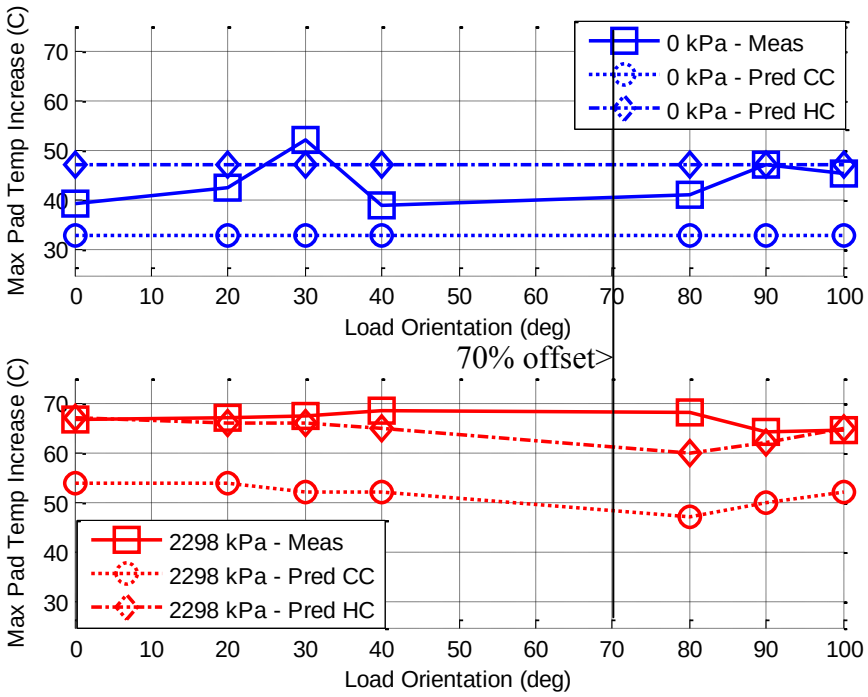

Figure 22. Measured and predicted maximum-pad-metal-temperature-increases at 13200 rpm, with 0 kPa (top) and 2298 kPa (bottom) loads

Static Equilibrium Position (SEP)

The SEP plot for the 0^{o} load orientation is shown in Figure 23. The results of Figure 23 are based on the assumption that the no-load condition defines the center of the bearing. Assuming the no-load condition as the bearing center yields very low attitude angles at light loads and negative attitude angles at higher loads; these are unexpected characteristics of fixed-arc bearings. Therefore, using the no-load condition to define the bearing center is not an accurate method.

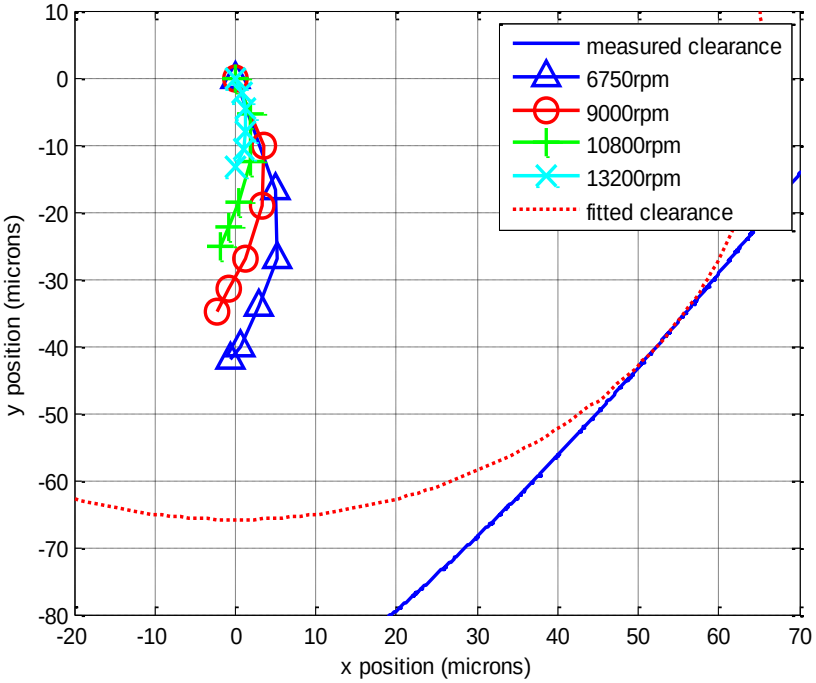

Figure 23. SEP for 0^o load orientation (assuming no-load test point at center)

Figure 24 shows the SEP plot for the 0^o orientation using the hot-clearance center to determine the rotor SEP at 0 kPa. Using the hot-clearance center yields larger attitude angles at light loads and all positive attitude angles, as expected for fixed-arc bearings. Therefore, using the hot-clearance center to determine the rotor SEP is the more accurate method.

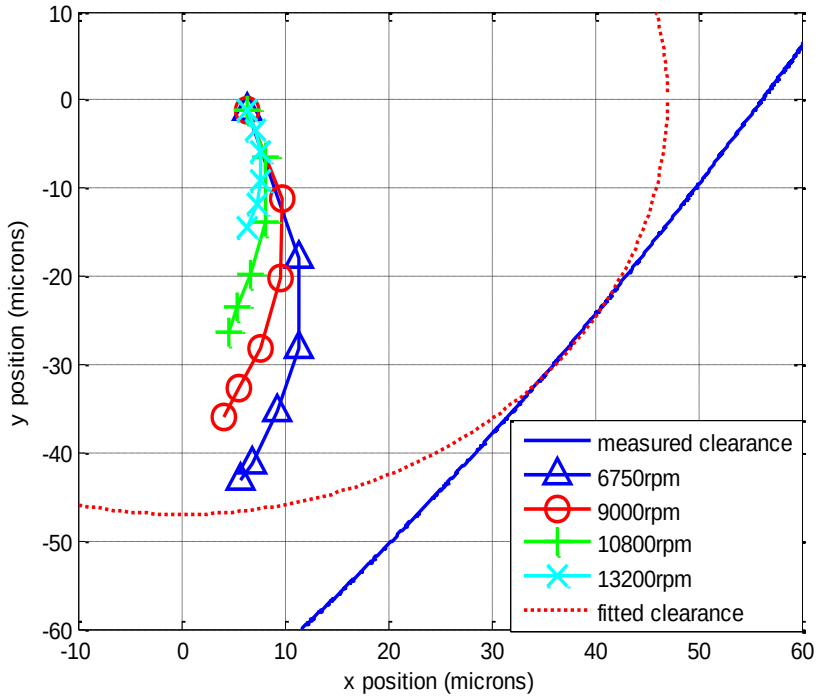

Figure 24. SEP for 0^o load orientation (using hot-clearance measurement to determine center)

Since the hot-clearance was only measured for one load orientation, the remaining SEP plots are not reported. The attitude angles are also not reported.

There is a small, constant difference between the eccentricities calculated by the two methods. The eccentricities are evaluated and reported, using the no-load condition to determine the bearing center.

Figure 25 shows the eccentricity ratio vs. load orientation at 6750 rpm, and at four different unit loads. The measured hot clearance is used to calculate the eccentricity ratios. The eccentricity ratio gives a measure of the static stiffness of the bearing, with a larger eccentricity ratio generally yielding a smaller static stiffness, and a smaller eccentricity ratio generally yielding a larger static stiffness. Figure 25 shows that the

bearing has the smallest eccentricity ratio (largest static stiffness) when loaded towards the 20°, 30°, and 40° load orientations. The bearing has the largest eccentricity ratio (smallest static stiffness) when loaded towards the leading or the trailing edge of the pad. This trend is also validated by the measured K_{yy} coefficients shown in a later section. The trend is more pronounced at higher static loads. At 575 kPa, the trend is not as well-defined.

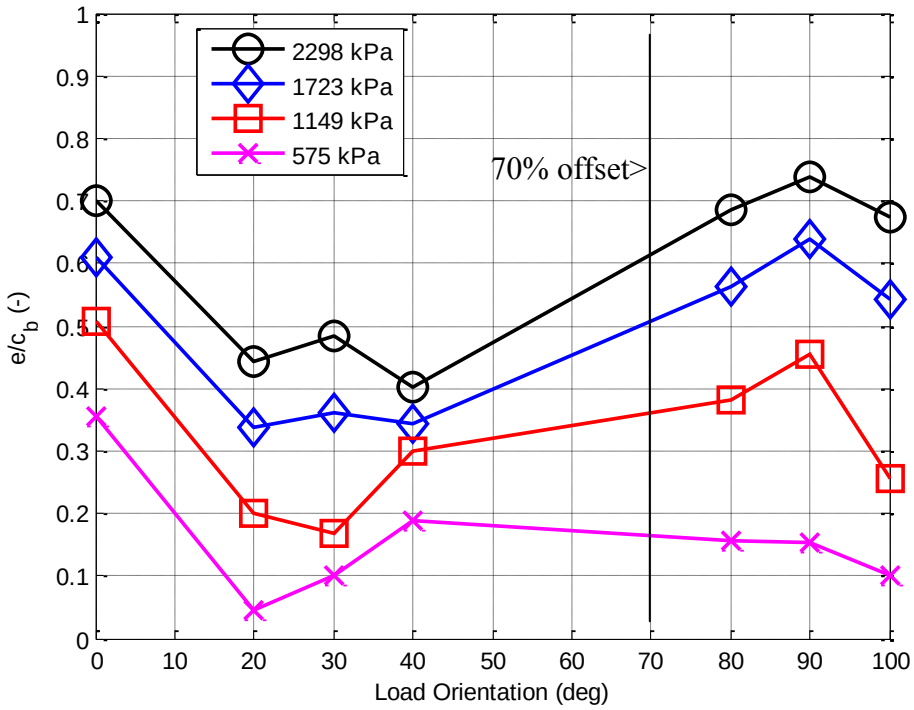

Figure 25. Eccentricity ratio vs. load orientation at 6750 rpm (hot clearance used to calculate eccentricity ratio)

Figure 26 shows the eccentricity ratio vs. load orientation at 13200 rpm and at four different unit loads. The plot shows that the bearing has the smallest eccentricity

ratio (largest static stiffness) when loaded towards the 20°, 30°, and 40° load orientations, and the largest eccentricity ratio (smallest static stiffness) when loaded towards the leading edge of the pad and the 80° load orientation. At 2298 kPa, the 90° and 100° load orientations also produce large eccentricity ratios, but this is not true at the other three loads. A comparison of Figures 25 and 26 shows that increasing running speed from 6750 rpm to 13200 rpm reduces the measured eccentricity ratios.

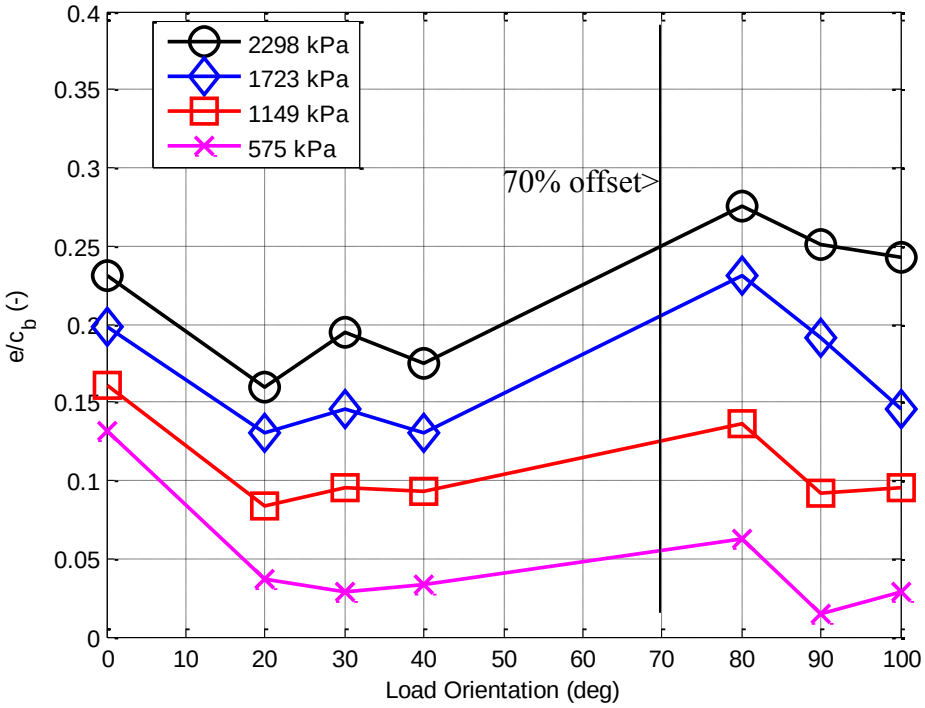

Figure 26. Eccentricity ratio vs. load orientation at 13200 rpm (hot clearance used to calculate eccentricity ratio)

Figure 27 shows the measured and predicted eccentricity ratios vs. load angle at the 13200 rpm/575 kPa (high-speed/low-load) test point. The high-speed/low-load test point is generally predicted to produce the smallest eccentricity ratio. As such, both the measured and predicted eccentricity ratios are below 0.1 for load orientations at this test

point. Predicted eccentricities are generally slightly higher than measured values at this test point.

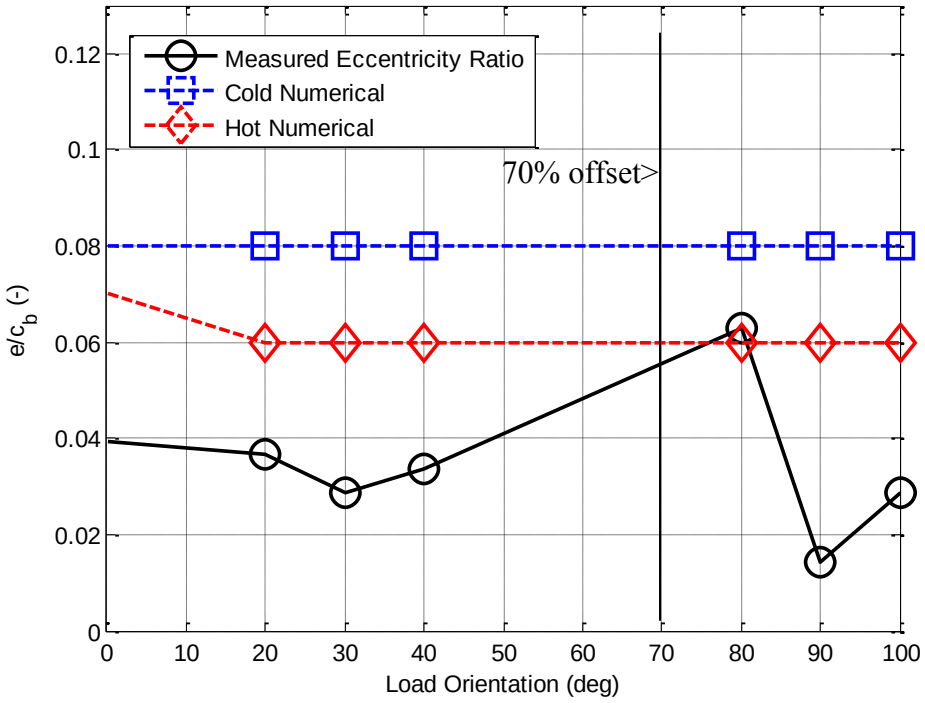

Figure 27. Eccentricity ratio vs. load orientation at 13200 rpm and 575 kPa (hot clearance used to calculate measured eccentricity ratio)

Figure 28 shows the eccentricity ratio vs. load angle at the 6750 rpm/2298 kPa (low-speed/high-load) test point. The low-speed/high-load test point is generally predicted to produce the largest eccentricity ratio. The measured eccentricity ratios range from 0.4-0.75 at this test point. As mentioned earlier, there is a smaller measured rotor eccentricity when the load is directed towards the center of the bearing, while there is a larger measured rotor eccentricity when the load is directed towards the leading and

trailing edges. The predictions (using either hot or cold clearance) show a similar trend with respect to load orientation sensitivity. However, the magnitudes of the predicted eccentricities are lower than the magnitudes of the measured eccentricities.

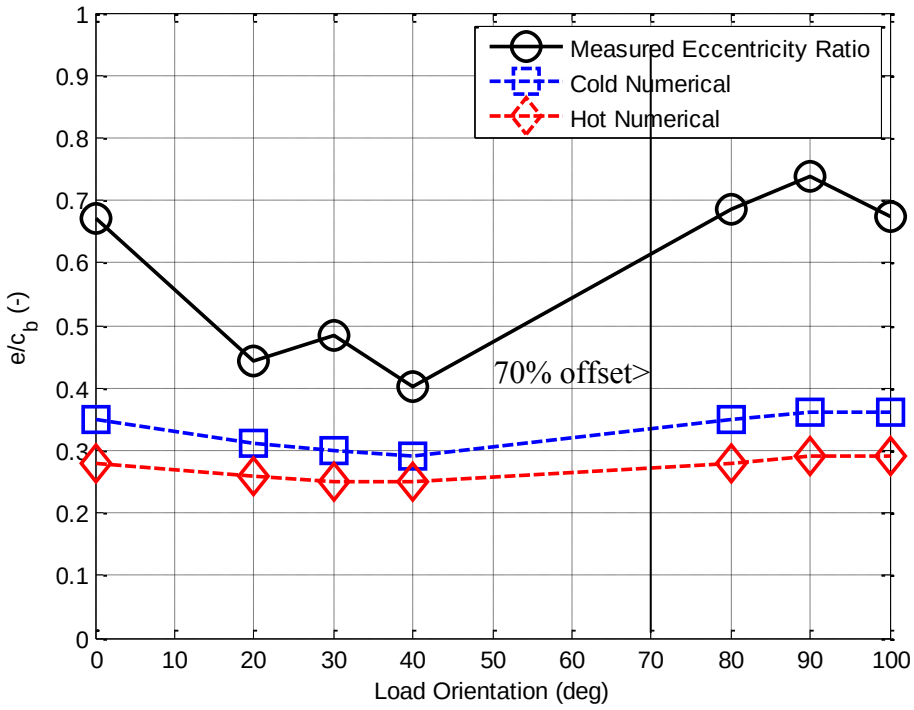

Figure 28. Eccentricity ratio vs. load orientation at 6750 rpm and 2298 kPa (hot clearance used to calculate measured eccentricity ratio)

HORIZONTAL-APPLICATION BEARING DYNAMIC RESULTS

Complex Dynamic Stiffness Measurements

Figure 29 illustrates the direct Re($\boldsymbol{H_{ij}}$) vs. Ω for the 6750 rpm/ 2298 kPa/80^o load orientation test point. The figure shows that the Re($\boldsymbol{H_{xx}}$) terms are 30-40% larger than the Re($\boldsymbol{H_{yy}}$) terms. This means that $K_{xx}>K_{yy}$. Additionally, the curvature of Re($\boldsymbol{H_{xx}}$) and Re($\boldsymbol{H_{yy}}$) terms implies that M_{xx} and M_{yy} are both close to zero. There is not a distinct upward or downward curvature versus Ω.

The repeatabilities of the Re($\boldsymbol{H_{xx}}$) and Re($\boldsymbol{H_{yy}}$) measurements shown in Figure 29 are fairly good. The repeatabilities vary for other load orientations, speeds, and static loads, but generally, the repeatabilities for all Re($\boldsymbol{H_{xx}}$) and Re($\boldsymbol{H_{yy}}$) measurements are quite good. In many cases, the repeatability bars are too small to be observed. Data points with repeatabilities on the same order of magnitude as the measured Re($\boldsymbol{H_{xx}}$) and Re($\boldsymbol{H_{yy}}$) coefficients were not used to evaluate the rotordynamic coefficients. The curve-fits of the measured direct stiffness coefficients to the linear [K][C][M] model defined by Eq. (5) are poor. The curve-fit of Re($\boldsymbol{H_{xx}}$) vs. Ω has an R^2 value of 0.68, and the curve-fit of Re($\boldsymbol{H_{yy}}$) vs. Ω has an R^2 value of 0.72. The R^2 values for Re($\boldsymbol{H_{xx}}$) and Re($\boldsymbol{H_{yy}}$) vs. Ω for the remaining load orientations (not shown) at 6750 rpm / 2298 kPa are all between 0.55 and 0.8.

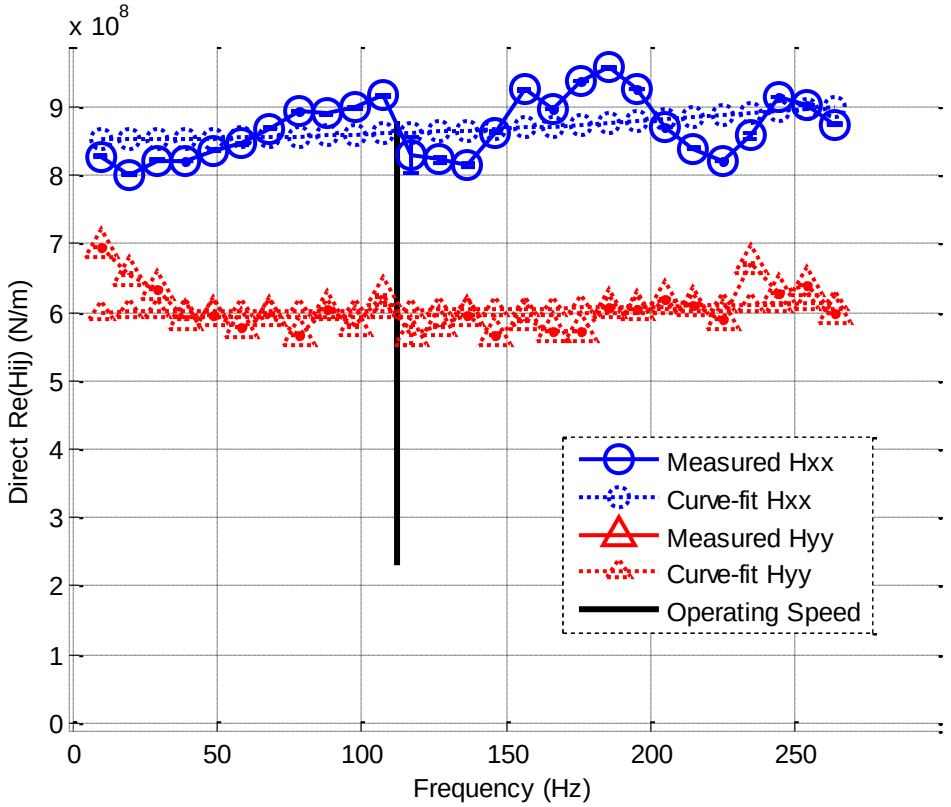

Figure 29. Re(H_{xx}) and Re(H_{yy}) at 6750 rpm / 2298 kPa / 80° load orientation

Figure 30 shows the cross-coupled Re($\boldsymbol{H_{ij}}$) vs. Ω for the 6750 rpm/ 2298 kPa/80° load orientation test point. The figure shows that, for low frequencies, |Re($\boldsymbol{H_{xy}}$)|>|Re($\boldsymbol{H_{yx}}$)|. This implies that $|K_{xy}|>|K_{yx}|$. For this load orientation, the magnitudes of Re($\boldsymbol{H_{xy}}$) and Re($\boldsymbol{H_{yx}}$) are roughly 0.3-0.4 times those of Re($\boldsymbol{H_{xx}}$) and Re($\boldsymbol{H_{yy}}$). Re($\boldsymbol{H_{xy}}$) and Re($\boldsymbol{H_{yx}}$) have different signs, implying that K_{xy} and K_{yx} have different signs. Different-sign cross-coupled stiffnesses contribute de-stabilizing forces to the rotor. The curvatures of Re($\boldsymbol{H_{xy}}$) and Re($\boldsymbol{H_{yx}}$) vs. Ω shown in Figure 30 imply that both M_{xy} and M_{yx} are not well-defined.

Figure 30 shows that the repeatabilities of Re($\boldsymbol{H_{xy}}$) and Re($\boldsymbol{H_{yx}}$) are quite good for this test point. In general, repeatabilities for the Re($\boldsymbol{H_{xy}}$) and Re($\boldsymbol{H_{yx}}$) coefficients

vary depending on speed, load, and load orientation. Data points with repeatabilities on the same order of magnitude as the measured Re($\boldsymbol{H}_{xy}$) and Re($\boldsymbol{H}_{yx}$) coefficients were not used to evaluate the rotordynamic coefficients. The curve-fits of the real parts of the cross-coupled complex dynamic stiffness coefficients to the linear [K][C][M] model defined by Eq. (5) are poor. The curve-fit of Re($\boldsymbol{H}_{xy}$) vs. Ω has an R^2 value of 0.69, and the curve-fit of Re($\boldsymbol{H}_{yx}$) vs. Ω has an R^2 value of 0.62. The R^2 values for Re($\boldsymbol{H}_{xx}$) and Re($\boldsymbol{H}_{yy}$) vs. Ω for the remaining load orientations (not shown) at 6750 rpm / 2298 kPa are all between 0.5 and 0.75.

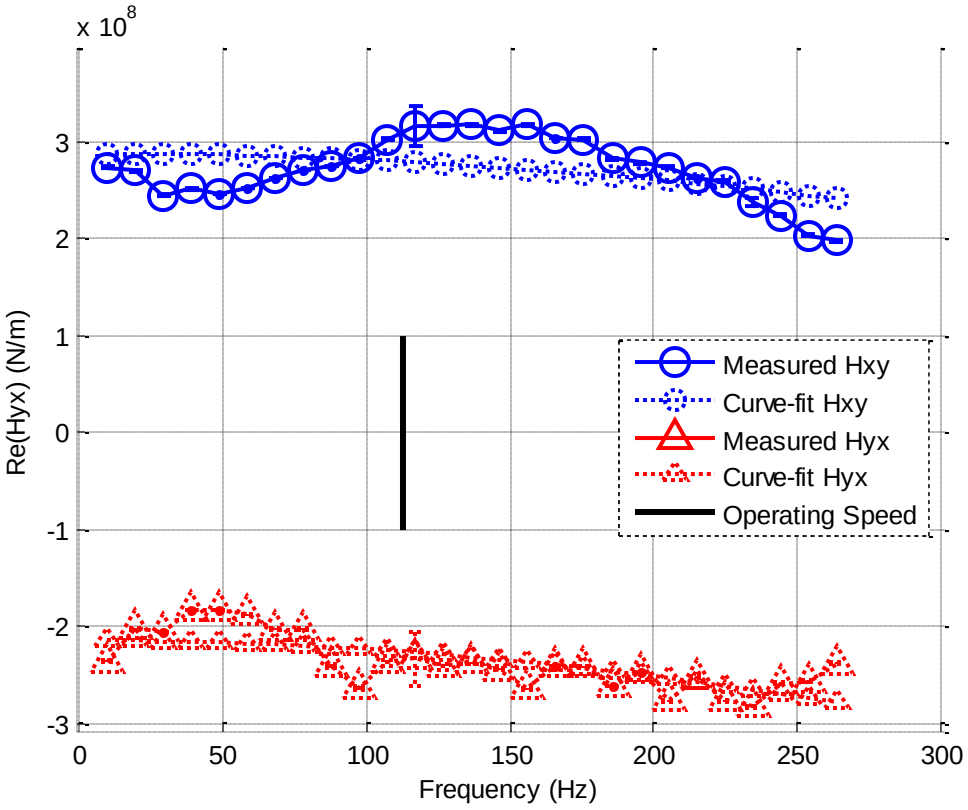

Figure 30. Re($\boldsymbol{H}_{xy}$) and Re($\boldsymbol{H}_{yx}$) at 6750 rpm / 2298 kPa / 80° load orientation

In general, the magnitudes of K_{xx}, K_{yy}, K_{xy}, and K_{yx} vary with speed, load, and load orientation; these coefficients are discussed in detail in subsequent sections. M_{xx} M_{xy}, M_{yx}, and M_{yy} are not reported, because uncertainties for the majority of these coefficients are on the same order of magnitude (or larger) as the measured results. The uncertainties of the rotordynamic coefficients, calculated as the 95% confidence intervals of the $\boldsymbol{H_{ij}}$ vs. Ω curve-fit coefficients, are shown later in this section.

Figure 31 shows Im($\boldsymbol{H_{xx}}$) and Im($\boldsymbol{H_{yy}}$) vs. Ω for the 6750 rpm/ 2298 kPa /80^o load orientation test point. The figure shows that the Im($\boldsymbol{H_{xx}}$) and Im($\boldsymbol{H_{yy}}$) terms are well-fitted by a frequency-independent, constant damping coefficient. The Im($\boldsymbol{H_{xx}}$) and Im($\boldsymbol{H_{yy}}$) terms are close in magnitude at low frequencies and diverge at higher frequencies, with Im($\boldsymbol{H_{xx}}$) being larger than Im($\boldsymbol{H_{yy}}$). Since the slope of the direct imaginary complex dynamic stiffness coefficients vs. frequency determines the direct damping coefficients, the divergence of Im($\boldsymbol{H_{xx}}$) and Im($\boldsymbol{H_{yy}}$) vs. Ω implies $C_{xx}>C_{yy}$.

The Im($\boldsymbol{H_{xx}}$) and Im($\boldsymbol{H_{yy}}$) coefficients have very high repeatabilities and very good curve-fits. In many cases, the repeatability bars are too small to be observed. R^2 values for the curve-fits for all load orientations, speeds, and loads are greater than 0.95.

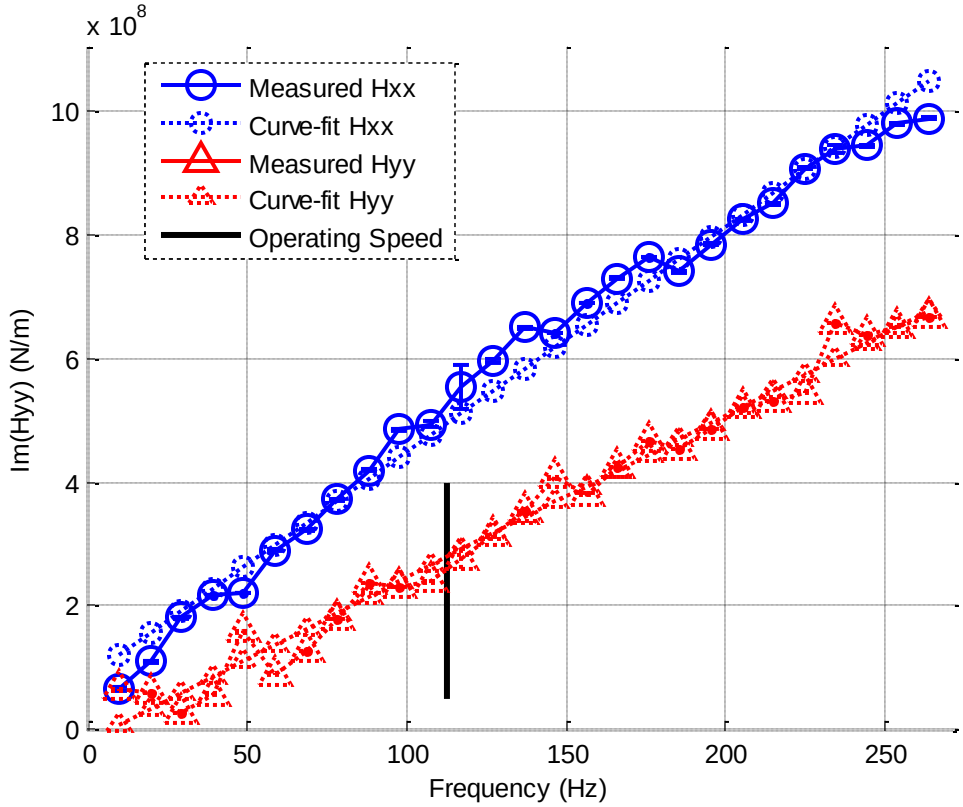

Figure 31. Im(H_{xx}) and Im(H_{yy}) at 6750 rpm / 2298 kPa / 80° load orientation

Figure 32 shows Im($\boldsymbol{H_{xy}}$) and Im($\boldsymbol{H_{yx}}$) vs. Ω for the 6750 rpm/ 2298 kPa /80° load orientation test point. The figure shows that Im($\boldsymbol{H_{xy}}$) increases with frequency and Im($\boldsymbol{H_{yx}}$) decreases with frequency. This means that C_{xy} is positive and C_{yx} is negative. Im($\boldsymbol{H_{xy}}$) and Im($\boldsymbol{H_{yx}}$) are poorly curve-fitted as linear functions of Ω. The curve-fit of Im($\boldsymbol{H_{xy}}$) vs. Ω has an R^2 value of 0.48, and the curve-fit of Im($\boldsymbol{H_{yx}}$) vs. Ω has an R^2 value of 0.18. Generally speaking, the Im($\boldsymbol{H_{xy}}$) and Im($\boldsymbol{H_{yx}}$) coefficients have poorer repeatabilities than the other measured complex dynamic coefficients. For this reason, the C_{xy} and C_{yx} terms are not evaluated or reported.

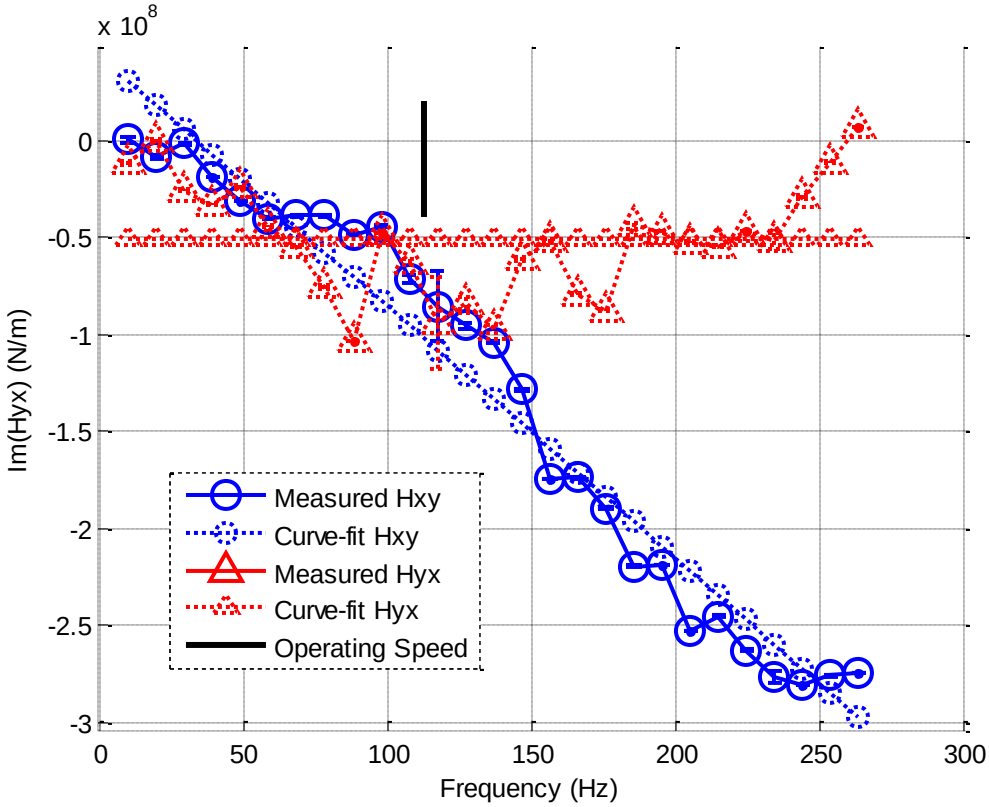

Figure 32. Im(H_{xy}) and Im(H_{yx}) at 6750 rpm / 2298 kPa / 80° load orientation

Table 8 summarizes the R^2 values and 95% confidence intervals for the coefficients of all of the $\boldsymbol{H_{ij}}$ vs. Ω curve-fits for the 6750 rpm/2298 kPa/ 80° load orientation test point. The values in Table 8 are generally representative of all speeds, loads, and load orientations. The confidence intervals of the slopes of the curve-fits of all of the Re($\boldsymbol{H_{ij}}$) coefficients are very high, and thus M_{xx}, M_{yy}, M_{xy}, and M_{yx} are not well-defined. The confidence intervals of the slopes of the curve-fits of the cross-coupled Im($\boldsymbol{H_{ij}}$) coefficients are high, and thus C_{xy} and C_{yx} are not well-defined. However, the 95% confidence intervals of K_{xx}, K_{yy}, K_{xy}, K_{yx}, C_{xx}, and C_{yy}, are quite low. As stated earlier, these coefficients are evaluated and presented in subsequent sections.

Table 8. R^2 Values and 95% Confidence Intervals of Coefficients for 6750 rpm/2298 kPa/80^o Load Orientation (Confidence Intervals < 10% in Bold)

Coefficient	R^2 value of curve-fit	Confidence interval of y-intercept (expressed as percentage of y-intercept)	Confidence interval of slope (expressed as percentage of the slope)
Re($\boldsymbol{H}_{xx}$)	.68	**+/- 2.8%**	+/- 107%
Re($\boldsymbol{H}_{xy}$)	.69	**+/- 6.1%**	+/- 80%
Re($\boldsymbol{H}_{yx}$)	.62	**+/- 5.6%**	+/- 40%
Re($\boldsymbol{H}_{yy}$)	.72	**+/- 3.2%**	+/- 296%
Im($\boldsymbol{H}_{xx}$)	.98	N/A	**+/- 4.7%**
Im($\boldsymbol{H}_{xy}$)	.48	N/A	+/- 21.2%
Im($\boldsymbol{H}_{yx}$)	.18	N/A	+/- 8927%
Im($\boldsymbol{H}_{yy}$)	.99	N/A	**+/- 5.4%**

Thus far, complex dynamic coefficients for the 80^o load orientation have been presented. Generally speaking, the trends noted for Figures 29-32 and Table 8 apply to the other six load orientations as well.

Measured vs. Predicted Direct Stiffness Coefficients

Figure 33 shows the measured and predicted K_{xx} and K_{yy} coefficients for the 100^o load orientation at 6750 rpm. Predictions for the "no-load" condition were run using a 1.3 kPa load to represent a very light static load. Measurements and predictions both show that K_{xx} and K_{yy} coefficients increase with increasing load for this load orientation at 6750 rpm. Also, both measurements and predictions show that K_{xx} is larger than K_{yy} for this load orientation. Both predictions and measurements show that $K_{xx} \cong K_{yy}$ at the no-load condition.

Using the measured cold clearance, K_{xx} and K_{yy} are well-predicted at 6750 rpm. The K_{xx} and K_{yy} coefficients predicted using the measured hot clearance are both larger than measured values at 6750 rpm. This makes sense, as the true clearance is expected to be closer to the measured cold clearance at 6750 rpm.

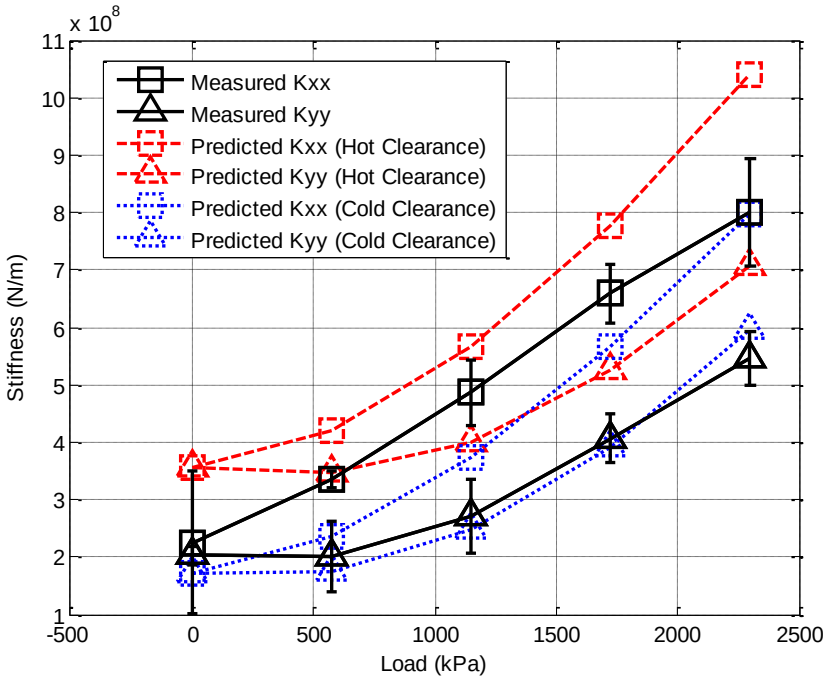

Figure 33. K_{xx} and K_{yy} for 100° load orientation at 6750 rpm

Figure 34 shows the K_{xx} and K_{yy} coefficients for the 100° load orientation at 13200 rpm. Both the K_{xx} and K_{yy} coefficients increase when increasing speed from 6750 rpm to 13200 rpm. Using the measured hot clearance, K_{yy} is well-predicted at 13200 rpm. K_{xx} coefficients predicted using the measured cold and hot clearance are lower than measured K_{xx} coefficients, but predictions using the hot clearance give better agreement. These trends make sense, as the true clearance is expected to be closer to the measured hot clearance at 13200 rpm. Comparing Figures 33 and 34 shows that the measured and

predicted K_{xx} and K_{yy} coefficients increase as running speed increases from 6750 rpm to 13200 rpm.

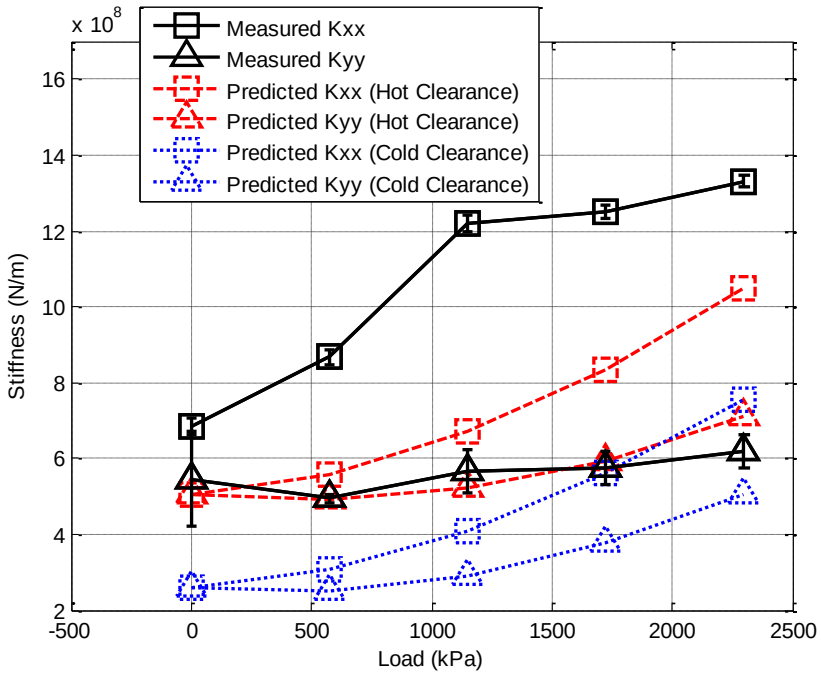

Figure 34. K_{xx} and K_{yy} for 100° load orientation at 13200 rpm

In general, these trends are representative of all load orientations and speeds. In a later section, the measured K_{xx} and K_{yy} coefficients are presented versus load orientation.

Measured vs. Predicted Cross-Coupled Stiffness Coefficients

Figure 35 shows the measured and predicted K_{xy} and K_{yx} for the 100° load orientation at 6750 rpm. Predictions for the "no-load" condition were run using a 1.3 kPa load to represent a very light static load. Both measurements and predictions show $K_{xy} \cong -K_{yx}$. Additionally, both measurements and predictions show relatively constant

K_{xy} terms vs. unit load. The K_{xy} and K_{yx} coefficients predicted using either the hot clearance or cold clearance are larger than measured cross-coupled stiffnesses. However, predictions using the cold clearance give significantly better agreement with measured values than predictions using the hot clearance.

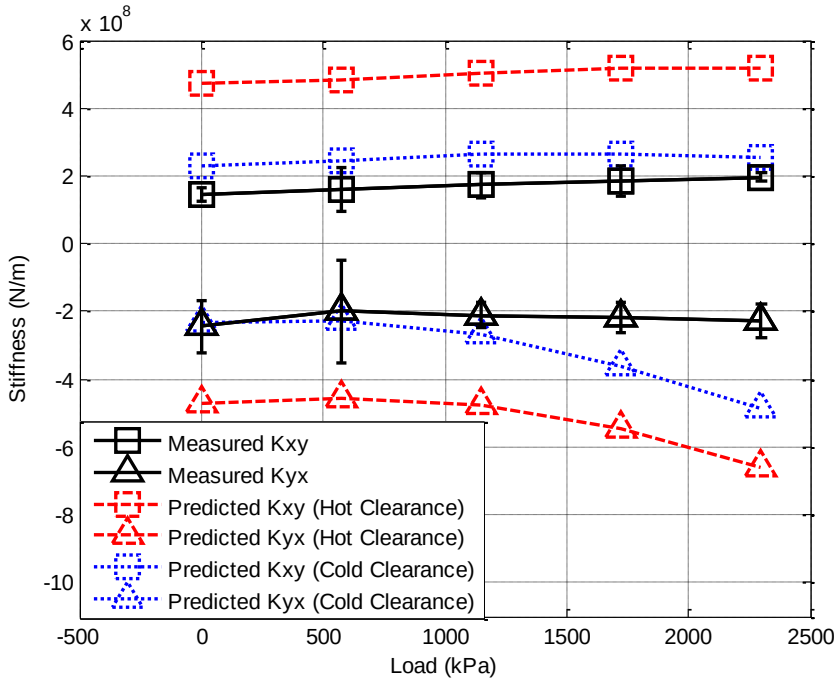

Figure 35. K_{xy} and K_{yx} for 100° load orientation at 6750 rpm

Figure 36 shows K_{xy} and K_{yx} for the 100° load orientation at 13200 rpm. The cross-coupled coefficients predicted using the cold clearance are very close to the measured values. At 13200 rpm, however, the operating radial bearing clearance is expected to be closer to the hot clearance. Comparing Figures 35 and 36 shows that both measured and predicted $|K_{xy}|$ and $|K_{yx}|$ increase as running speed increases from 6750 rpm to 13200 rpm.

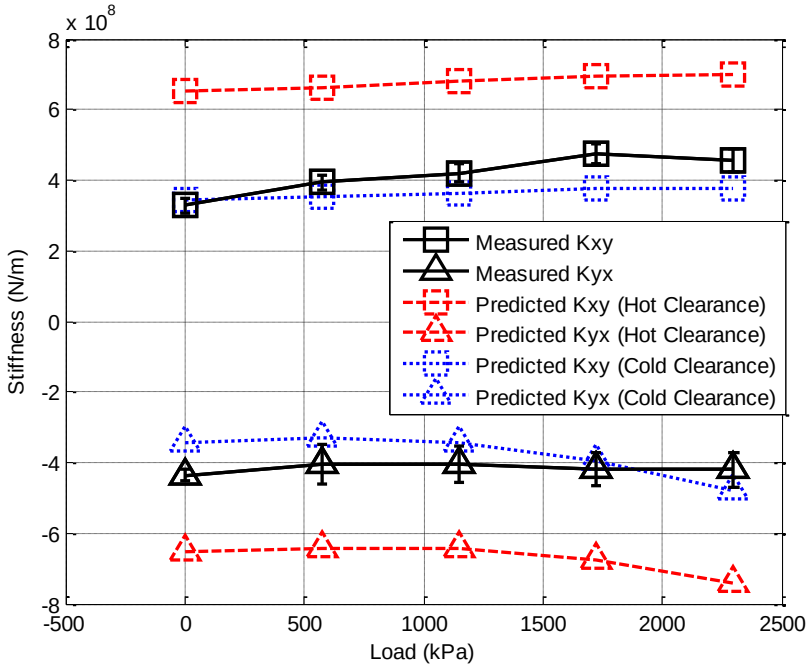

Figure 36. K_{xy} and K_{yx} for 100° load orientation at 13200 rpm

In general, these trends are representative of all load orientations and speeds. In subsequent sections, the measured K_{xy} and K_{yx} coefficients are presented versus load orientation.

Measured vs. Predicted Direct Damping Coefficients

Figure 37 shows measured and predicted C_{xx} and C_{yy} coefficients for the 100° load orientation at 6750 rpm. Predictions for the "no-load" condition were run using a 1.3 kPa load to represent a very light static load.

The C_{xx} and C_{yy} terms predicted by using both the hot clearance and cold clearance are larger than measured values in Figure 37. However, agreement between the predictions and the measured data is better at lighter loads than at higher loads. Both predictions show C_{xx} and C_{yy} increasing with increasing load, but the measured C_{xx} and

C_{yy} terms are relatively constant versus unit load. Both measurements and predictions show a higher C_{xx} term than a C_{yy} term for this load orientation.

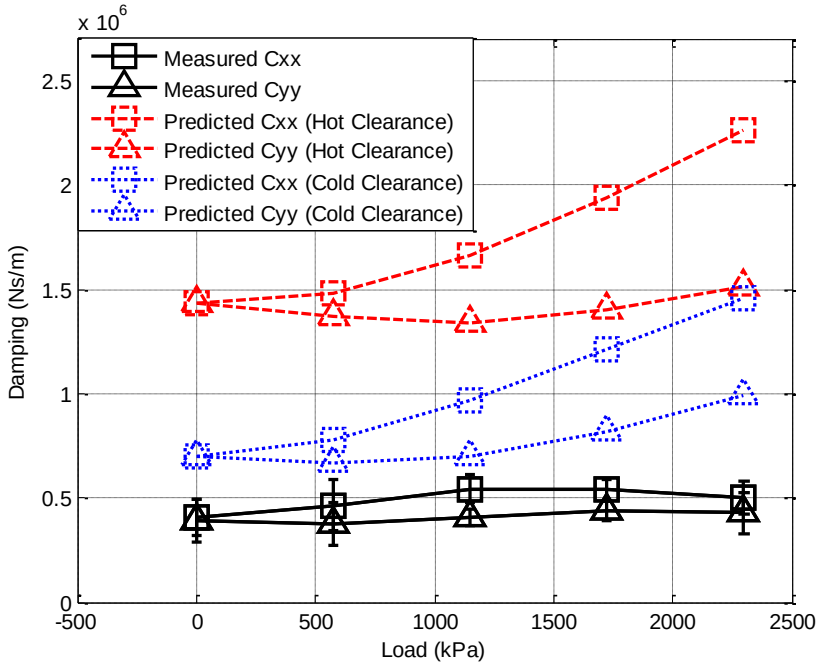

Figure 37. C_{xx} and C_{yy} for 100° load orientation at 6750 rpm

Figure 38 shows measured and predicted C_{xx} and C_{yy} coefficients for the 100° load orientation at 13200 rpm. Increasing speed from 6750 rpm to 13200 rpm slightly decreases the measured C_{xx} and C_{yy} coefficients. Predictions show that C_{xx} and C_{yy} should decrease when increasing running speed from 6750 rpm to 13200 rpm. For example, both the C_{xx} and C_{yy} coefficients predicted using the hot clearance at 0 kPa decrease by approximately 45% when increasing speed from 6750 rpm to 13200 rpm.

Comparing Figures 37 and 38 shows that predictions do not improve with increasing speed. At both speeds, predicted C_{xx} and C_{yy} terms are larger than measured values.

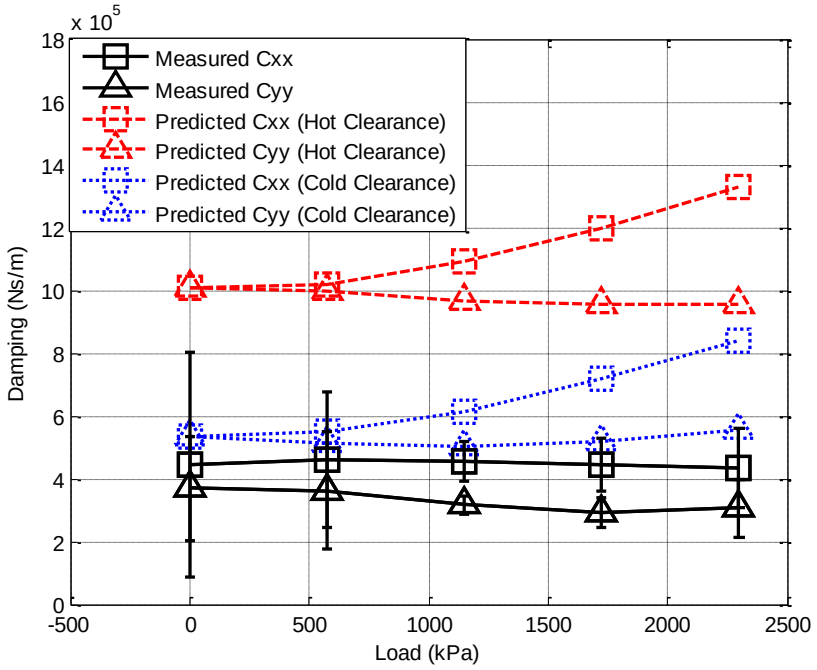

Figure 38. C_{xx} and C_{yy} for 100° load orientation at 13200 rpm

In general, these trends are representative of all load orientations and speeds. In a later section, the measured C_{xx} and C_{yy} coefficients are presented versus load orientation.

Load-Angle Orientation Comparison of Measured Dynamic Coefficients

This section shows comparisons of the rotordynamic coefficients vs. static load orientation. As mentioned earlier, the *y*- direction is always the loaded direction and the *x*- direction is always orthogonal to the loaded direction.

Figure 39 shows K_{xx} and K_{yy} vs. load orientation at 6750 rpm. The bearing has the highest K_{xx} and lowest K_{yy} when the load vector is pointed towards the trailing edge of the pad. The bearing has the lowest K_{xx} and highest K_{yy} when the load vector is pointed towards the middle of the pad. Pointing the load vector closer to the leading

edge of the pad produces an intermediate value of K_{xx} and a low K_{yy}. The trend becomes more pronounced with larger loads. At 0 kPa, this trend is not very prevalent.

The K_{yy} vs. load orientation measurements confirm the ε vs. load orientation measurements seen earlier in Figure 25. In general, Figure 25 showed that ε is lowest for the 20°, 30°, and 40° load orientations.

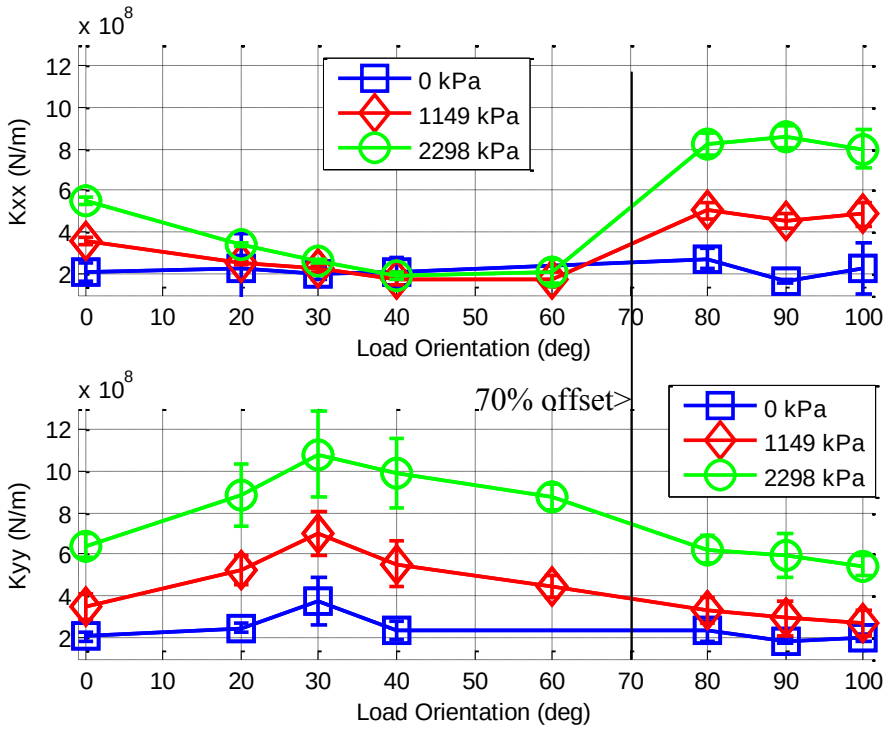

Figure 39. K_{xx} (top) and K_{yy} (bottom) vs. load orientation at 6750 rpm

Figure 40 shows K_{xx} and K_{yy} vs. load orientation at 13200 rpm. Generally speaking, the trends regarding load and load orientation at 6750 rpm also apply at 13200 rpm. Increasing running speed from 6750 rpm to 13200 rpm increases the value of both

K_{xx} and K_{yy}. The K_{yy} vs. load orientation measurements confirm the ε vs. load orientation measurements seen earlier in Figure 26.

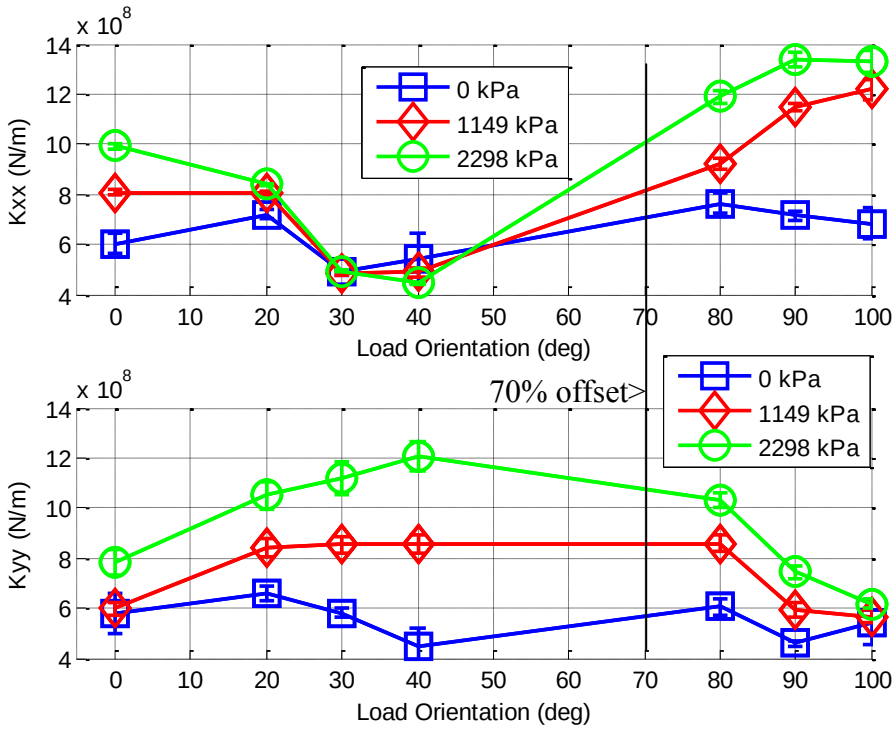

Figure 40. K_{xx} (top) and K_{yy} (bottom) vs. load orientation at 13200 rpm

Figure 41 shows K_{xx} and K_{yy} versus load orientation overlaid at the 6750 rpm / 2298 kPa test point. Additionally, the figure shows $|K_{xx} - K_{yy}|$ and $|K_{xx} - K_{yy}|$/average(K_{xx}, K_{yy}) versus load orientation for the same test point. Essentially, this figure shows a quantifiable measure of relative orthotropy and absolute orthotropy vs. load orientation. More orthotropy is generally beneficial to stability, and results in a reduction of the WFR.

Figure 41 shows that the bearing is the most orthotropic when loaded towards the middle of the pad, with K_{yy} being larger than K_{xx} by approximately 800 MN/m for the

30° and 40° load orientations. The bearing is less orthotropic when loaded towards the trailing edge of the pad, with K_{xx} being larger than K_{yy} by approximately 200 MN/m for the 80°, 90°, and 100° load orientations. At the leading edge of the pad, $K_{xx} \cong K_{yy}$.

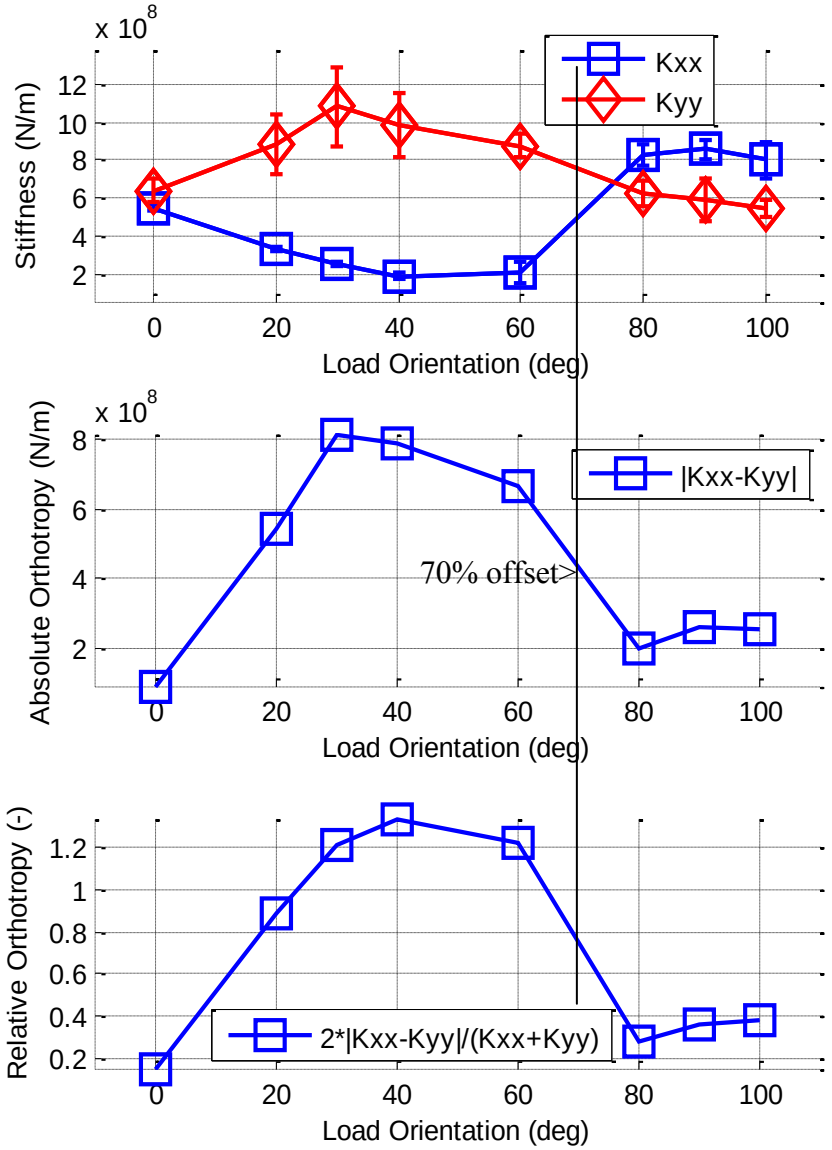

Figure 41. K_{xx} and K_{yy} (top) and $|K_{xx} - K_{yy}|$ (bottom) vs. load orientation at 6750 rpm / 2298 kPa

Figure 42 shows K_{xx} and K_{yy} versus load orientation overlaid at the 13200 rpm / 2298 kPa test point. The figure also shows $|K_{xx} - K_{yy}|$ and $|K_{xx} - K_{yy}|$/average(K_{xx}, K_{yy}) versus load orientation at the same test point. Comparing Figures 41 and 42 shows that the bearing has roughly the same absolute orthotropy when loaded at the 40° load orientation ($|K_{xx} - K_{yy}|$ = 800 MN/m) at both speeds. However, because the average value of K_{xx} and K_{yy} increases with speed from approximately 600 MN/m to 800 MN/m, the relative orthotropy, as a ratio of the absolute orthotropy to the average value of K_{xx} and K_{yy}, decreases with speed from approximately 1.3 to 0.9 for the 40° load orientation. Increasing running speed from 6750 rpm to 13200 rpm increases the absolute orthotropy of the bearing when loaded at the trailing edge of the pad from approximately 200 MN/m to 800 MN/m, and increases the relative orthotropy from approximately 0.4 to 0.75.

Figure 43 shows K_{xy} and K_{yx} versus load orientation at 6750 rpm. At 0 kPa, K_{xy} and K_{yx} are largely independent of load orientation. At the higher loads, the bearing has the smallest K_{xy} terms when the load vector is pointed towards the leading edge of the pad. The bearing has the largest magnitude (most negative) of K_{yx} coefficients when the load vector is pointed towards the leading edge of the pad. These trends regarding load orientation become more pronounced at larger loads. The K_{xy} and K_{yx} coefficients measured for the 60°, 80°, 90°, and 100° load orientations do not change much with increasing load magnitudes.

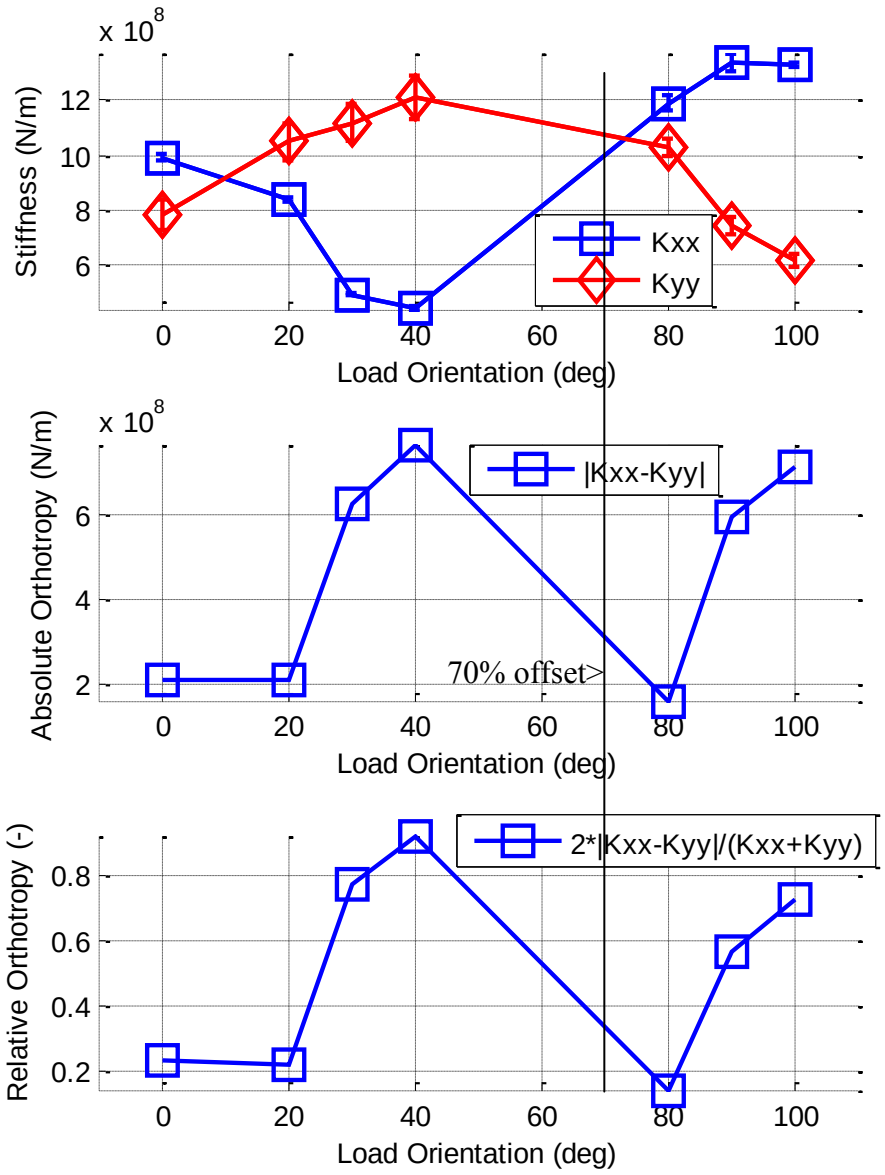

Figure 42. K_{xx} and K_{yy} (top) and $|K_{xx} - K_{yy}|$ (bottom) vs. load orientation at 13200 rpm / 2298 kPa

K_{xy} and K_{yx} have the same sign for the 0°, 20°, and 30° load orientations at 2298 kPa. Same-sign cross-coupled stiffness coefficients do not feed energy into the rotor's

whirl orbit and thus are not de-stabilizing. This is reflected later in the WFR calculations, as all three of these test points have 0 WFRs.

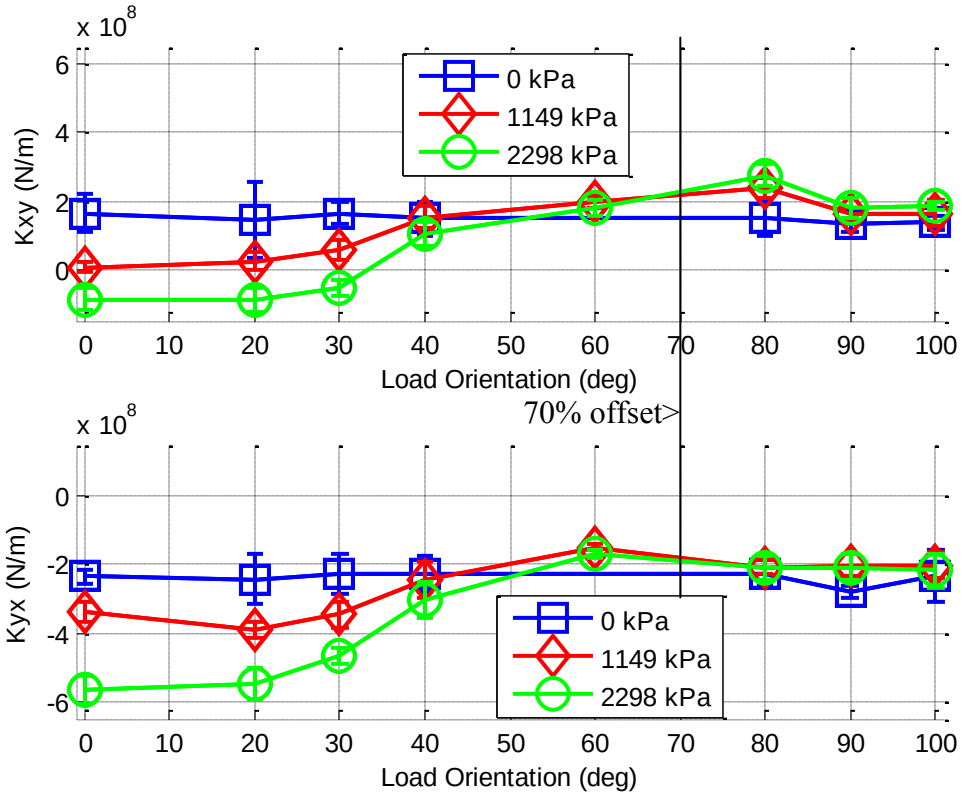

Figure 43. K_{xy} (top) and K_{yx} (bottom) vs. load orientation at 6750 rpm

Figure 44 shows K_{xy} and K_{yx} versus load orientation at 13200 rpm. In general, the trends regarding load orientation noted above for Figure 43 apply to Figure 44 as well. However, at 13200 rpm, the K_{xy} terms for the 60°, 80°, 90°, and 100° increase with load magnitude and K_{xy} terms for the 0°, 20°, and 30° load orientations do not change much with load magnitude. At 13200 rpm, there are no test points with same-sign K_{xy} and K_{yx} coefficients. A comparison of Figures 43 and 44 shows that increasing speed from 6750 rpm to 13200 rpm generally increases both $|K_{xy}|$ and $|K_{yx}|$.

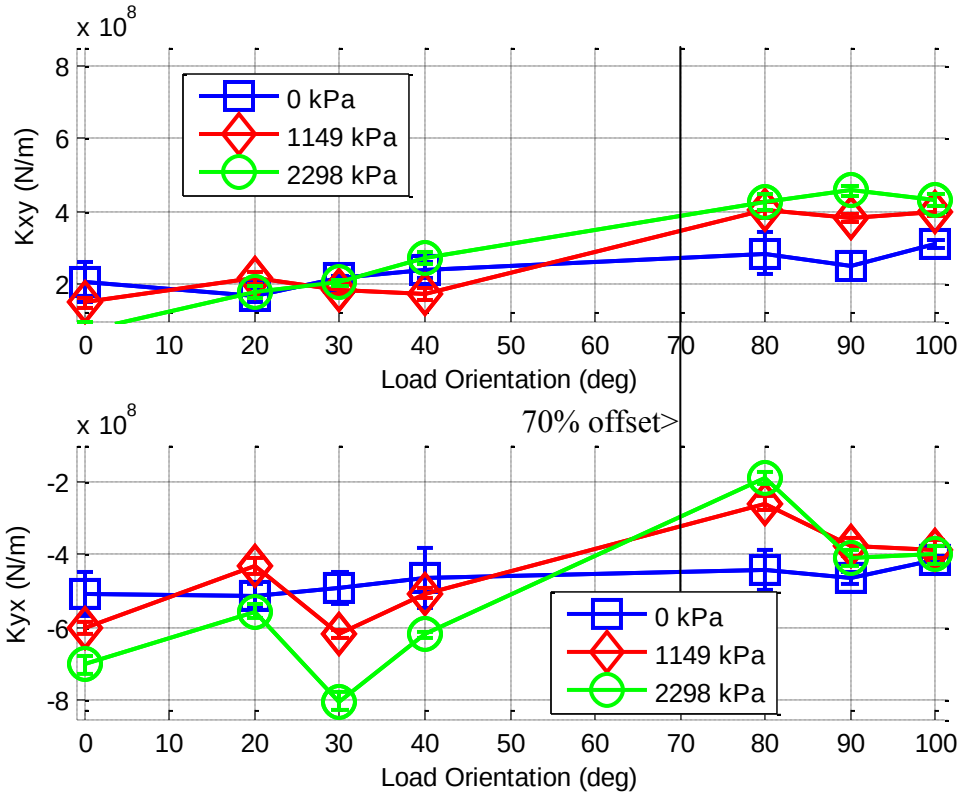

Figure 44. K_{xy} (top) and K_{yx} (bottom) vs. load orientation at 13200 rpm

Figure 45 shows K_{eq} versus load orientation at 6750 rpm. The K_{eq} coefficients increase with increasing load magnitudes. At 0 kPa and 1149 kPa, K_{eq} is largely independent of load orientation. At the 2298 kPa, the bearing has the largest K_{eq} term when the load orientation is 80^o, 90^o, or 100^o. The K_{eq} coefficient for the 80^o load orientation is 40% larger than that for the 0^o load orientation.

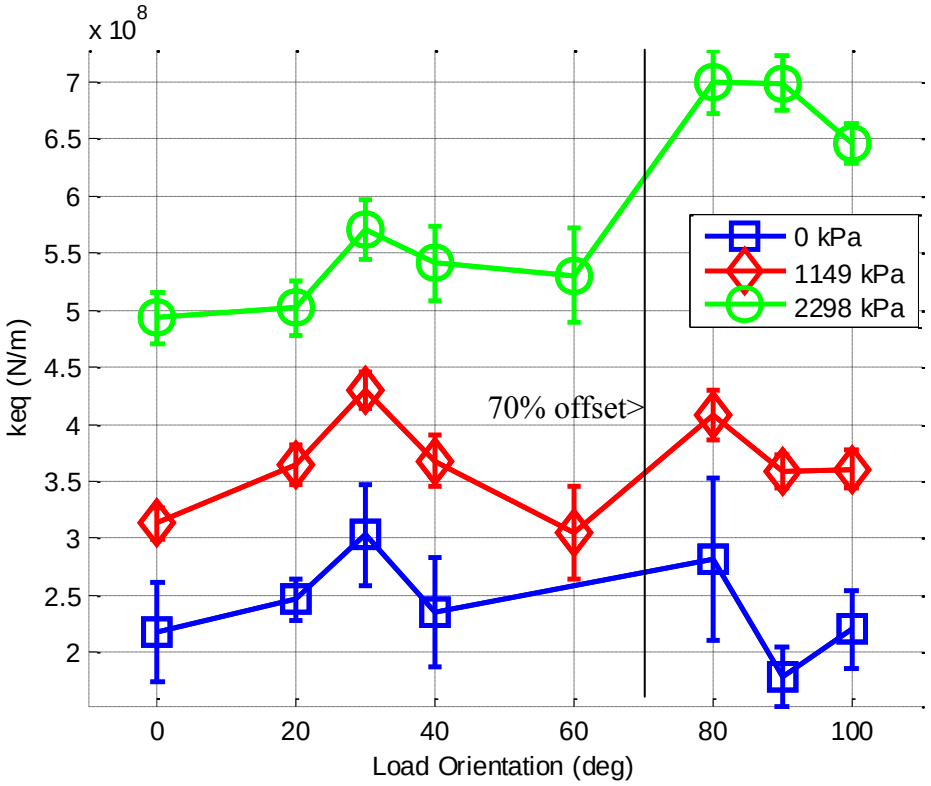

Figure 45. K_{eq} vs. load orientation at 6750 rpm

Figure 46 shows K_{eq} versus load orientation at 9000 rpm. Increasing speed from 6750 rpm to 13200 rpm increases the values of K_{eq} at all test points. At 1149 kPa and 2298 kPa, the 80° load orientation has the largest K_{eq} coefficient. At 0 kPa, the K_{eq} coefficients are largely independent of load orientaiton.

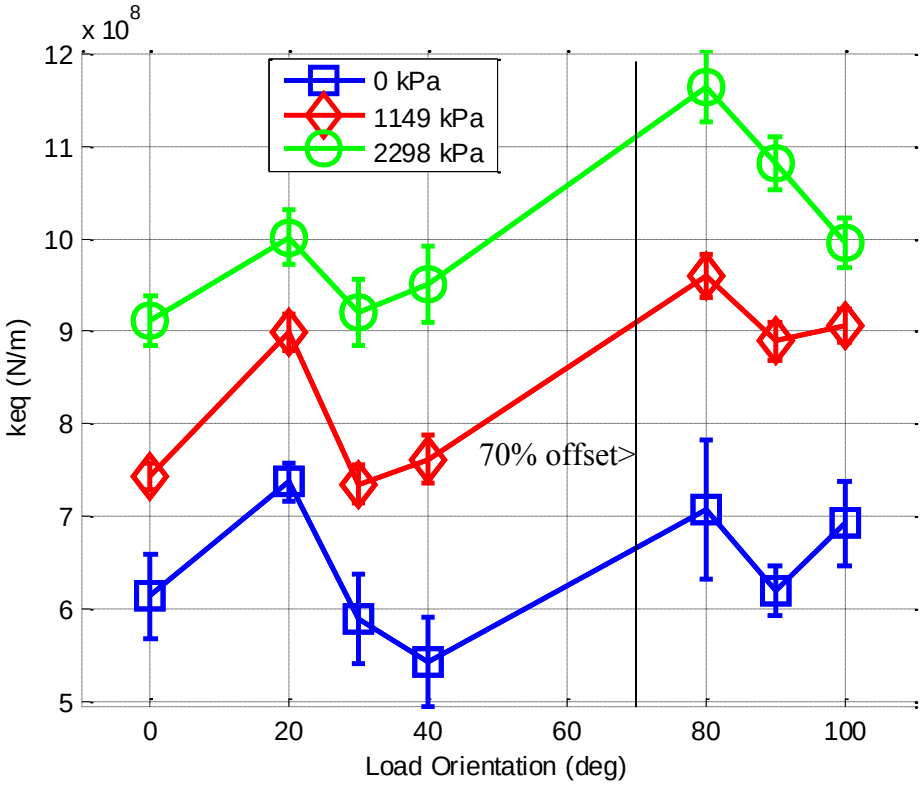

Figure 46. K_{eq} vs. load orientation at 13200 rpm

Figure 47 shows C_{xx} and C_{yy} versus load orientation at 6750 rpm. At 0 kPa, C_{xx} and C_{yy} are largely independent of load orientation. At the larger loads, the C_{xx} coefficients are largest when the load vector is pointed towards the trailing edge of the pad and lowest when the load vector is pointed towards the leading edge of the pad. C_{yy} is largest when the load vector is pointed towards the leading edge of the pad and smallest when the load vector is pointed towards the trailing edge of the pad. This trend becomes more pronounced as load increases. C_{xx} decreases with increasing load for load orientations pointing towards the leading edge of the pad and increases with increasing load for load orientations pointing towards the trailing edge of the pad. C_{yy} increases with increasing load for all load orientations at 6750 rpm.

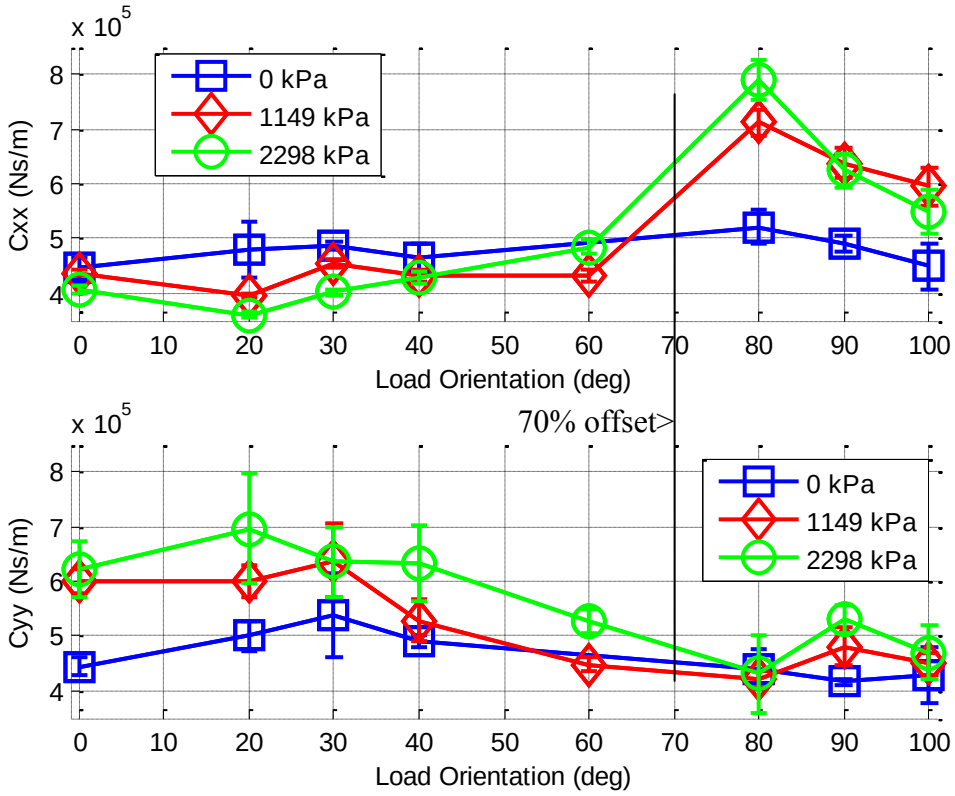

Figure 47. C_{xx} (top) and C_{yy} (bottom) vs. load orientation at 6750 rpm

Figure 48 shows C_{xx} and C_{yy} versus load orientation at 13200 rpm. Figure 46 generally shows the same trends noted in Figure 47 regarding load orientation. A comparison of Figures 47 and 48 shows that increasing the running speed from 6750 rpm to 13200 rpm generally decreases the magnitude of both C_{xx} and C_{yy}. Figure 48 also shows that increasing unit load decreases the magnitude of the C_{yy} coefficients at all load orientations, opposite of the trend noted in Figure 47.

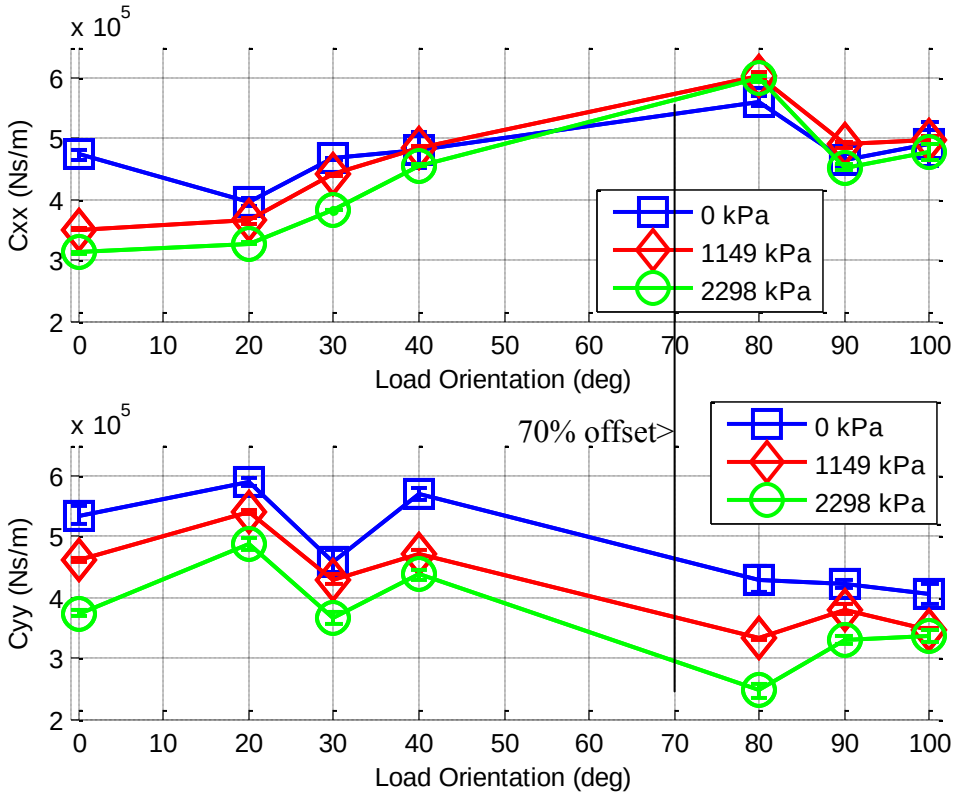

Figure 48. C_{xx} (top) and C_{yy} (bottom) vs. load orientation at 13200 rpm

Whirl Frequency Ratios

Since the uncertainties of M_{xy} and M_{yx} were large, Lund's [5] WFR formula, shown earlier in Eq. (6), was used.

Figure 49 shows the WFR vs. load orientation at 6750 rpm. At 0 kPa, the WFR is largely independent of load orientation. The 80°, 90°, and 100° load orientations show consistently higher WFRs than the 0°, 10°, 20°, and 40° orientations, especially at higher loads and lower speeds. At 6750 rpm and 2298 kPa (the highest load and lowest speed tested), the 80°, 90°, and 100° load orientations show WFRs between 0.35 and 0.5; however, the 0°, 10°, 20°, 40°, and 60° load orientations have a zero WFR. Therefore, the load orientations closer to the leading edge of the pad and center of the pad are more

stable than the load orientations closer to the trailing edge of the pad for the 6750 rpm/2298 kPa test point.

Figure 49 also shows that increasing unit load generally decreases WFR. The large decreases in WFR with increasing unit load for load orientations close to the leading edge of the pad is due to larger increases in the magnitudes of C_{yy} with increasing load, as noted earlier in Figure 47. The zero WFRs for load orientations close to the middle of the pad at 2298 kPa is due to large stiffness orthotropy for the load orientations near the center of the pad, as noted earlier in Figure 41. WFRs are between 0.5 and 0.7 at the no-load test point for all load orientations.

Note that the 20°, 30°, and 40° load orientations are stable at 1149 kPa. Figure 25 showed that these test points produce ε between 0.2 and 0.3. This is quite different from a plain journal bearing, where ε~0.65 is required for good stability.

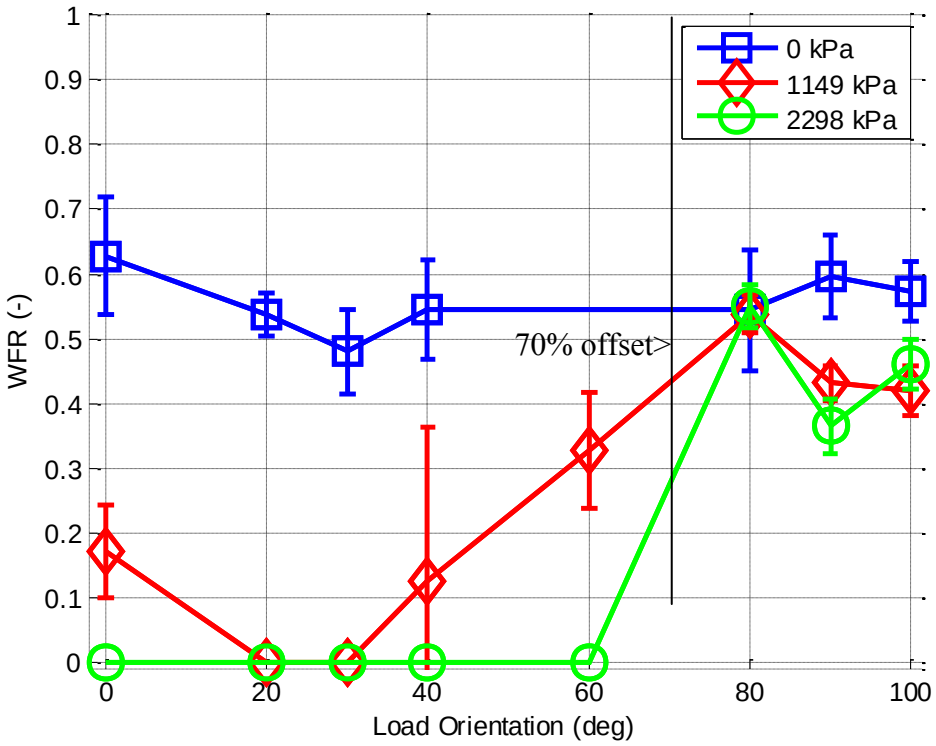

Figure 49. WFR vs. load orientation at 6750 rpm

Figure 50 shows the WFR vs. load orientation at 13200 rpm. At 13200 rpm, the WFR is largely independent of load orientation, and is between 0.3 and 0.7 at all test points. There is no discernible trend with respect to load magnitude at 13200 rpm. Comparing Figures 49 and 50 shows that increasing running speed from 6750 rpm to 13200 rpm generally increases WFR at all points where WFR<0.4 at 6750 rpm. For the test points with WFR>0.4, there is no discernable trend in respect to speed.

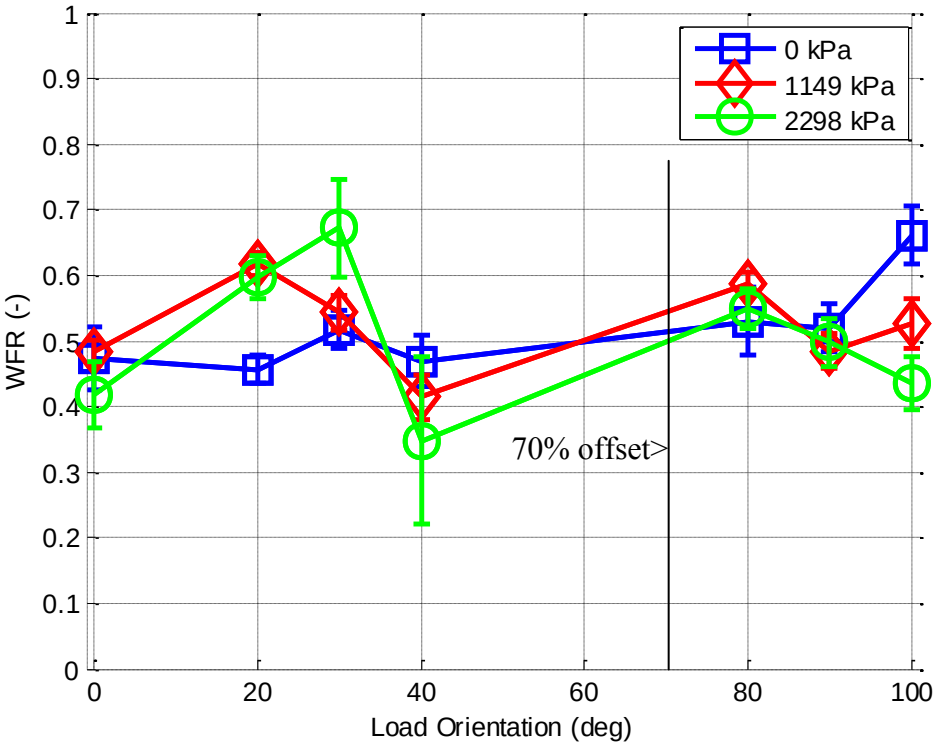

Figure 50. WFR vs. load orientation at 13200 rpm

VERTICAL-APPLICATION BEARING DYNAMIC RESULTS

Complex Dynamic Stiffnesses

Figure 51 shows Re($\boldsymbol{H}_{xx}$) and Re($\boldsymbol{H}_{yy}$) vs. Ω for the vertical-application bearing at 9000 rpm and 117 kPa. The curve-fit of the Re($\boldsymbol{H}_{xx}$) vs. Ω measurement has a 0.62 R^2 value, while the curve-fit for the Re($\boldsymbol{H}_{yy}$) vs. Ω measurement has a 0.41 R^2 value. The Re($\boldsymbol{H}_{xx}$) coefficients are slightly higher than the Re($\boldsymbol{H}_{yy}$) coefficients at low frequencies, implying that $K_{xx} > K_{yy}$. The curvature of the Re($\boldsymbol{H}_{xx}$) and Re($\boldsymbol{H}_{yy}$) coefficients vs. Ω is not well-defined. Thus, M_{xx} and M_{yy} are not well-defined. Repeatabilities for the Re($\boldsymbol{H}_{xx}$) and Re($\boldsymbol{H}_{yy}$) coefficients were generally good, and in many cases, the repeatability bars are too small to be observed. Generally speaking, the trends noted for Figure 51 apply to the remaining speeds and loads.

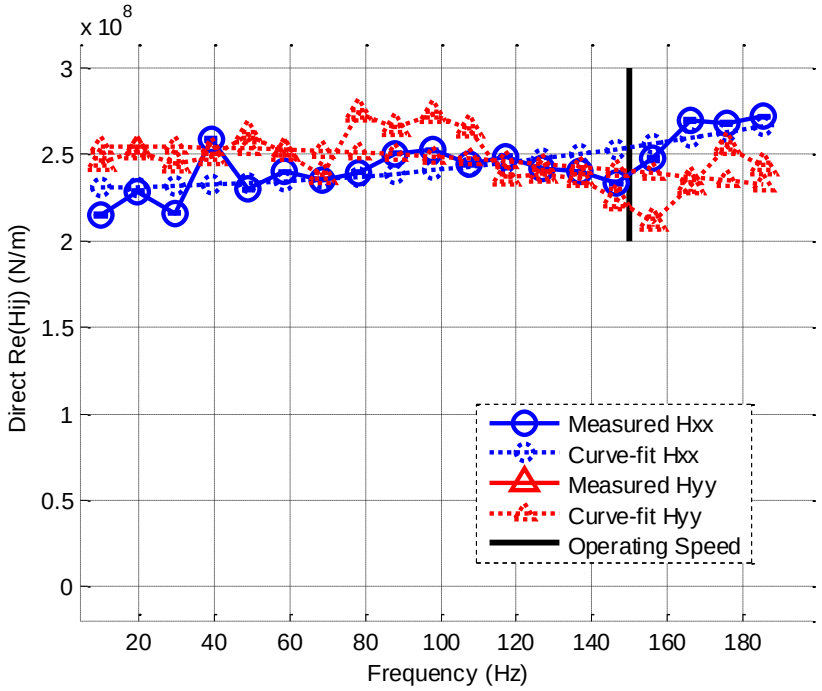

Figure 51. Re(H_{xx}) and Re(H_{yy}) measurements at 9000 rpm and 117 kPa

Figure 52 shows Re($\boldsymbol{H_{xy}}$) and Re($\boldsymbol{H_{yx}}$) vs. Ω for the vertical-application bearing at 9000 rpm and 117 kPa. The curve-fit of the Re($\boldsymbol{H_{xx}}$) vs. Ω measurement has a 0.51 R^2 value, while the curve-fit for the Re($\boldsymbol{H_{yy}}$) vs. Ω measurement has a 0.45 R^2 value. Re($\boldsymbol{H_{xy}}$) is positive and Re($\boldsymbol{H_{yx}}$) is negative, implying that K_{xy} and K_{yx} have opposite signs. This means that K_{xy} and K_{yx} contribute de-stabilizing forces to the rotor. The curvature of the Re($\boldsymbol{H_{xy}}$) and Re($\boldsymbol{H_{yx}}$) coefficients vs. Ω is not well-defined. Thus, M_{xy} and M_{yx} are not well-defined. Repeatabilities for the Re($\boldsymbol{H_{xy}}$) and Re($\boldsymbol{H_{yx}}$) coefficients were generally good, and in many cases, the repeatability bars are too small to be observed. Generally speaking, the trends noted for Figure 52 apply to the remaining speeds and loads.

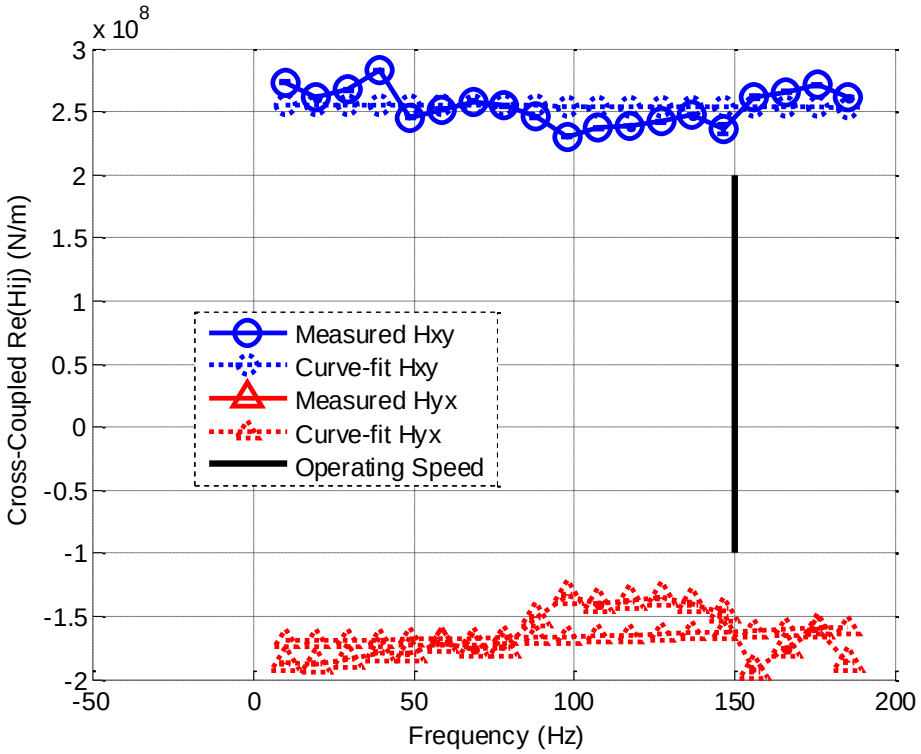

Figure 52. Re(H_{xy}) and Re(H_{yx}) measurements at 9000 rpm and 117 kPa

Figure 53 shows Im($\boldsymbol{H_{xx}}$) and Im($\boldsymbol{H_{yy}}$) vs. Ω for the vertical-application bearing at 9000 rpm and 117 kPa. The slope of Im($\boldsymbol{H_{xx}}$) is slightly larger than the slope of Im($\boldsymbol{H_{yy}}$), implying that $C_{xx}>C_{yy}$. The R^2 value for the curve-fit of Im($\boldsymbol{H_{xx}}$) versus Ω is 0.97, while the R^2 value for the curve-fit of Im($\boldsymbol{H_{yy}}$) versus Ω is 0.99. The uncertainty bars for the Im($\boldsymbol{H_{xx}}$) and Im($\boldsymbol{H_{yy}}$) coefficients are fairly good. Thus, both Im($\boldsymbol{H_{xx}}$) and Im($\boldsymbol{H_{yy}}$) are well-defined by frequency-independent damping terms. Generally speaking, the trends regarding the goodness-of-fit and repeatabilities of the Im($\boldsymbol{H_{xx}}$) and Im($\boldsymbol{H_{yy}}$) terms apply to all other speeds and loads, as well. In all cases, curve-fits of Im($\boldsymbol{H_{xx}}$) and Im($\boldsymbol{H_{yy}}$) vs. Ω carried R^2 values between 0.92 and 1.00.

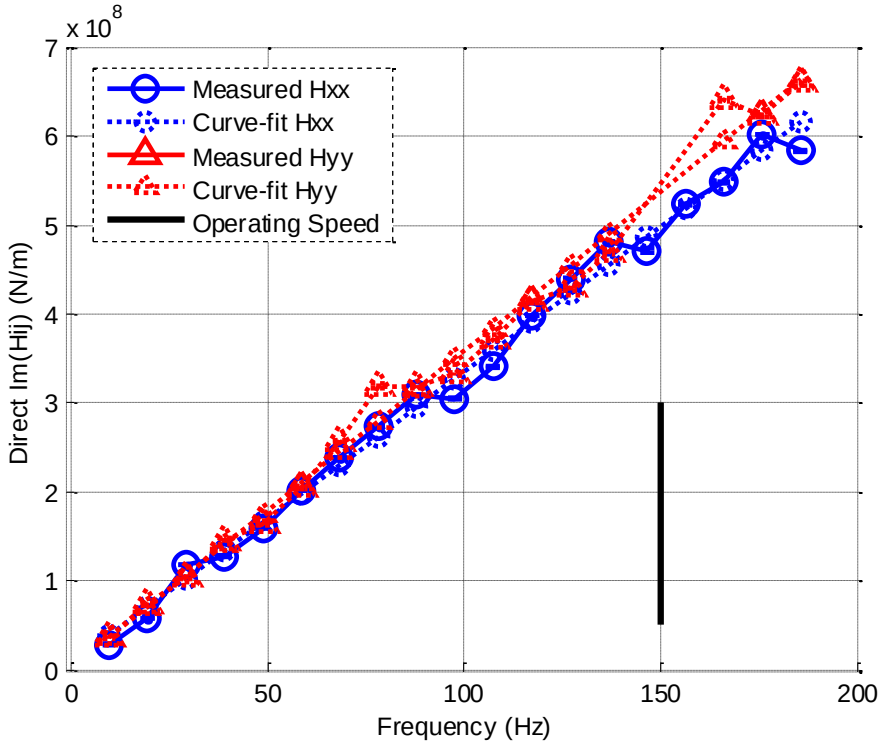

Figure 53. Im($\boldsymbol{H_{xx}}$) and Im($\boldsymbol{H_{yy}}$) measurements at 9000 rpm and 117 kPa

Figure 54 shows Im($\boldsymbol{H_{xy}}$) and Im($\boldsymbol{H_{yx}}$) vs. Ω for the vertical-application bearing at 9000 rpm and 117 kPa. Repeatabilities for the Im($\boldsymbol{H_{yx}}$) coefficients are generally poor. The R^2 value for the curve-fit of Im($\boldsymbol{H_{xy}}$) versus Ω is 0.29, while the R^2 value for the curve-fit of Im($\boldsymbol{H_{yx}}$) versus Ω is 0.05. Neither Im($\boldsymbol{H_{xy}}$) nor Im($\boldsymbol{H_{yx}}$) are well-defined by a frequency-independent damping coefficient. Generally speaking, the curve-fits of Im($\boldsymbol{H_{xy}}$) nor Im($\boldsymbol{H_{yx}}$) were poorly-defined at most other test points. Thus, C_{xy} and C_{yx} are not reported.

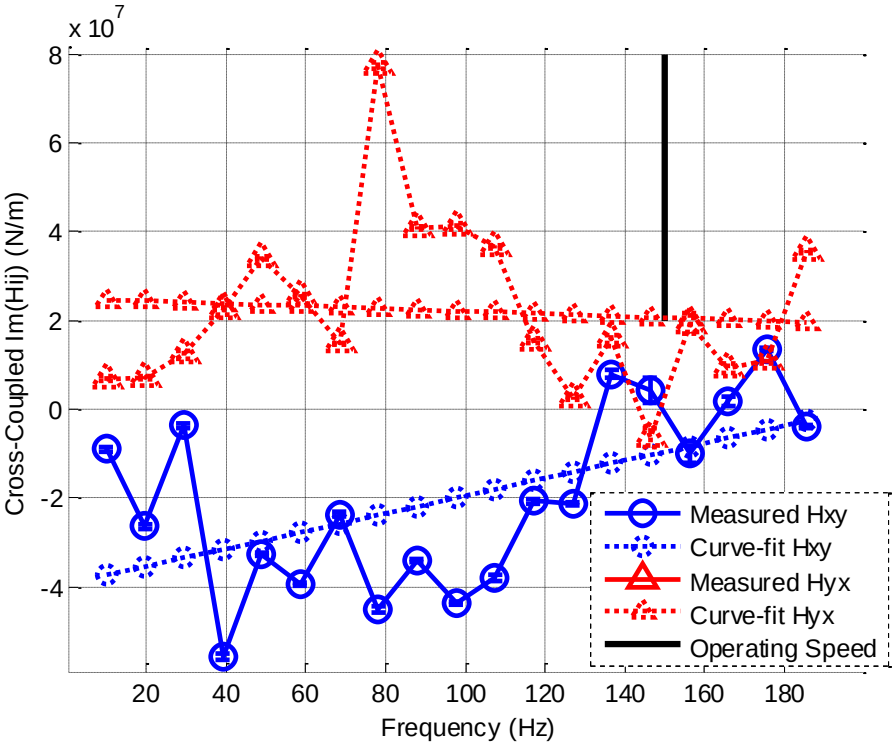

Figure 54. Im(H_{xy}) and Im(H_{yx}) measurements at 9000 rpm and 117 kPa

Table 9 summarizes the R^2 values and 95% confidence intervals for the coefficients of all of the $\boldsymbol{H_{ij}}$ vs. Ω curve-fits at 9000 rpm and 117 kPa. Due to the large confidence intervals, M_{xy}, M_{yx}, M_{xy}, M_{yx}, C_{xy}, and C_{yx} are not reported for the vertical-application bearing. However, the 95% confidence intervals of K_{xx}, K_{yy}, K_{xy}, K_{yx}, C_{xx}, and C_{yy}, are quite low. These coefficients are evaluated and presented in the next section.

Table 9. R^2 Values For Vertical-Application Bearing at 9000 rpm and 117 kPa (Confidence Intervals < 10% in Bold)

Coefficient	R^2 value of curve-fit	Confidence interval of y-intercept (expressed as percentage of y-intercept)	Confidence interval of slope (expressed as percentage of the slope)
Re($\boldsymbol{H_{xx}}$)	.62	**+/- 3.4%**	+/- 46.6%
Re($\boldsymbol{H_{xy}}$)	.51	**+/- 4.0%**	+/- 1149.4%
Re($\boldsymbol{H_{yx}}$)	.45	**+/- 8.5%**	+/- 289.4%
Re($\boldsymbol{H_{yy}}$)	.41	**+/- 4.1%**	+/- 97.9%
Im($\boldsymbol{H_{xx}}$)	.99	N/A	**+/- 4.2%**
Im($\boldsymbol{H_{xy}}$)	.29	N/A	+/- 73.9%
Im($\boldsymbol{H_{yx}}$)	.01	N/A	+/- 573.5%
Im($\boldsymbol{H_{yy}}$)	.99	N/A	**+/- 4.8%**

Direct Stiffness Coefficients

Figure 55 shows the measured and predicted K_{xx} and K_{yy} coefficients vs. unit load at 2000 rpm. Both sets of predictions (using the hot and cold measured clearances as

inputs) predict larger direct stiffnesses than were measured. Predictions using the cold clearance predict lower direct stiffnesses than those using the hot clearance. This means that measurements are in better agreement with the predictions using the cold clearance. Figure 55 also shows that the measured and predicted K_{xx} and K_{yy} coefficients do not vary significantly when increasing the unit load from 0 kPa to 117 kPa.

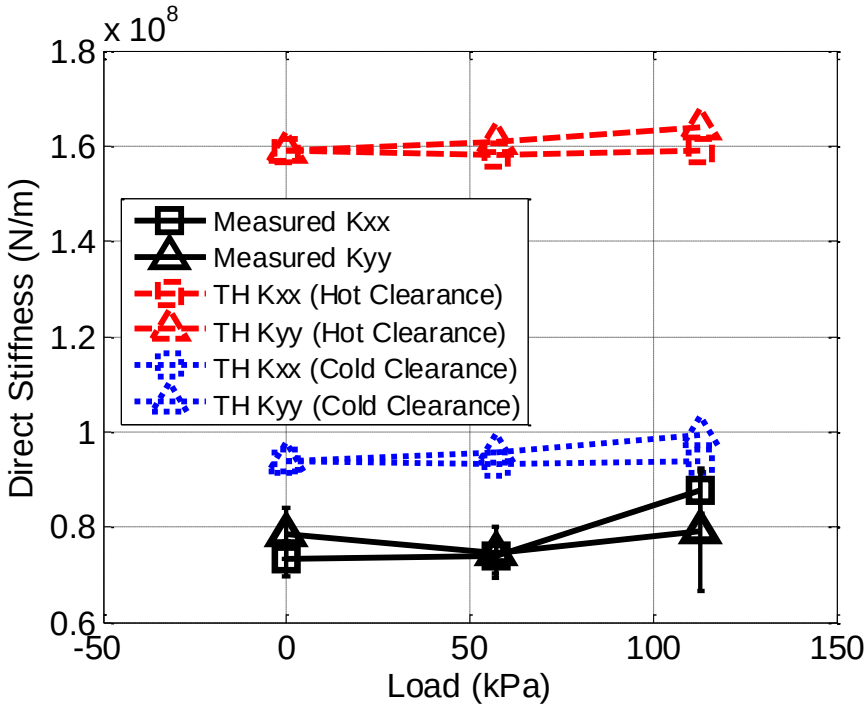

Figure 55. Vertical-application bearing K_{xx} and K_{yy} coefficients at 2000 rpm

Figure 56 shows the measured and predicted K_{xx} and K_{yy} coefficients vs. unit load at 9000 rpm. The same general trends regarding measurements vs. predictions seen in Figure 55 also apply to Figure 54. A comparison of Figures 55 and 56 shows that the

predicted and measured K_{xx} and K_{yy} coefficients are roughly three times larger at 9000 rpm than at 2000 rpm.

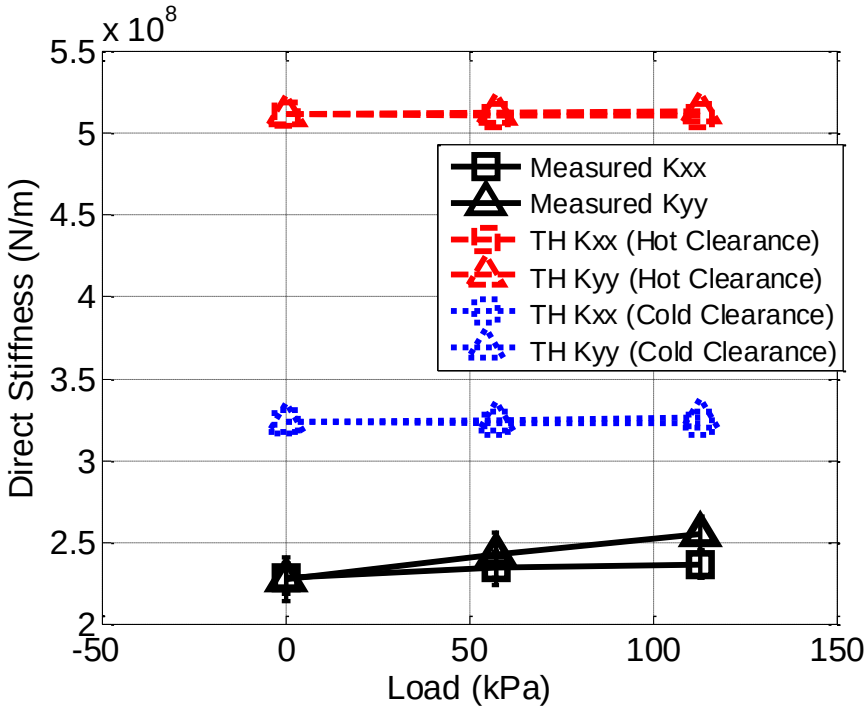

Figure 56. Vertical-application bearing K_{xx} and K_{yy} coefficients at 9000 rpm

Cross-Coupled Stiffness Coefficients

Figure 57 shows the measured and predicted K_{xy} and K_{yx} coefficients vs. unit load at 2000 rpm. K_{yx} coefficients are well-predicted. The predicted K_{yx} coefficients using the hot and cold clearances straddle the measured values at all three loads. The measured K_{xy} term is slightly larger than the K_{xy} term predicted by both solutions at 2000 rpm.

Figure 57 also shows that the model predicts $K_{xy} \cong -K_{yx}$. Measurements show that the K_{xy} coefficient magnitudes are approximately 2 times larger than the K_{yx} coefficient

magnitudes at 2000 rpm. There is little variability in the K_{xy} coefficients when applying light unit loads up to 117 kPa. The K_{yx} coefficients become less negative with increasing unit load.

For all predictions and measurements, the signs of K_{xy} and K_{yx} are opposite, meaning that they contribute de-stabilizing forces to the rotor.

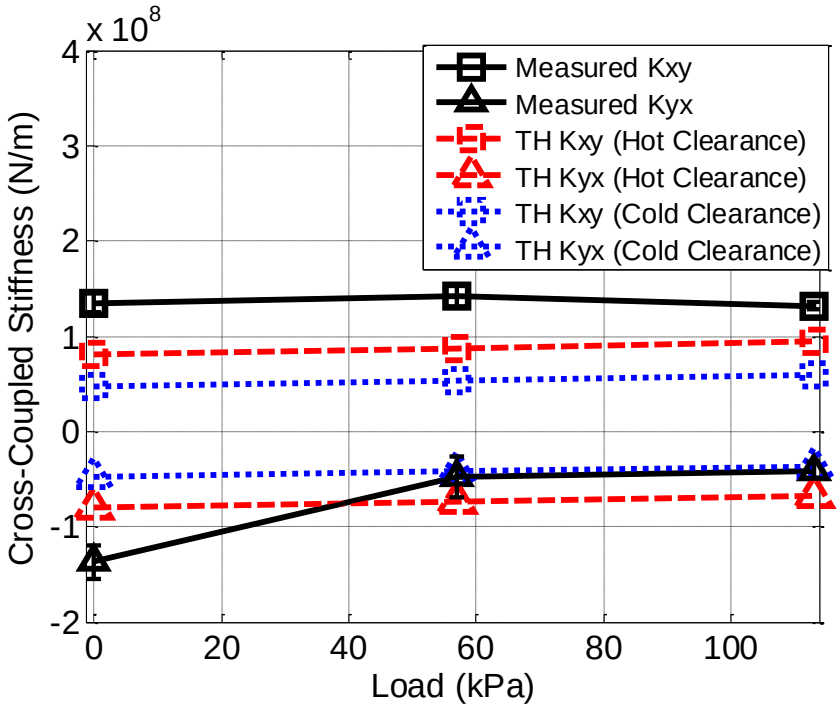

Figure 57. Vertical-application bearing K_{xy} and K_{yx} coefficients at 2000 rpm

Figure 58 shows the measured and predicted K_{xy} and K_{yx} coefficients vs. unit load at 9000 rpm. At 9000 rpm, the measured K_{xy} terms are fairly well-predicted using the hot clearance. K_{yx} is well-predicted by both prediction sets at this speed as well. The magnitude of K_{xy} is slightly larger than the magnitude of K_{xy}.

Comparing Figure 57 with Figure 58 shows that the magnitude of both the K_{xy} coefficients and the K_{yx} coefficients increases with increasing running speed. Since the signs of K_{xy} and K_{yx} are opposite, this implies that these coefficients contribute larger de-stabilizing forces at 9000 rpm than at 2000 rpm.

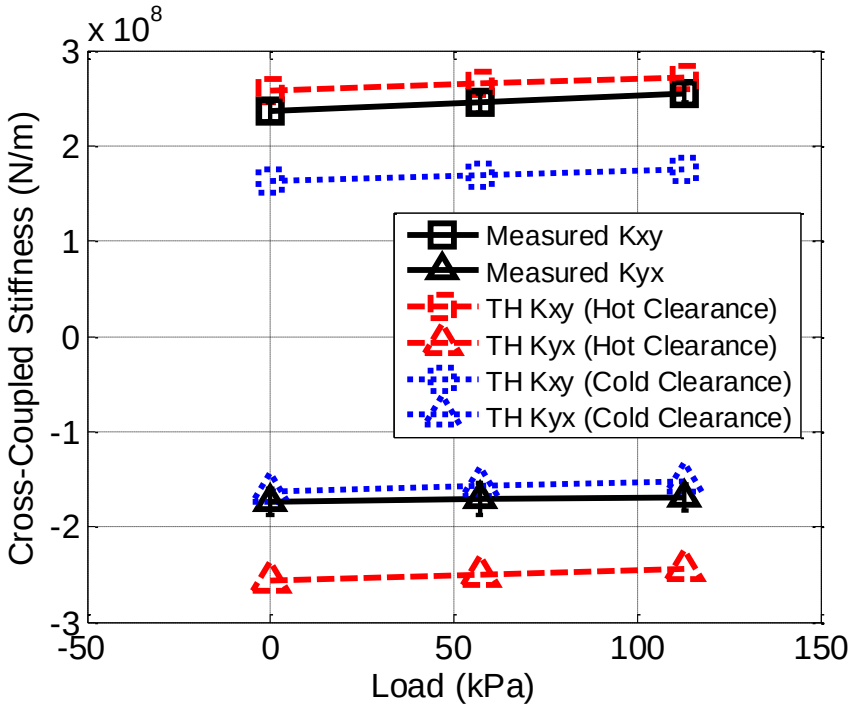

Figure 58. Vertical-application bearing K_{xy} and K_{yx} coefficients at 9000 rpm

Figure 59 shows the measured and predicted K_{eq} coefficients vs. unit load at 2000 rpm. Several of the trends noted in Figure 55 (K_{xx} and K_{yy} at 2000 rpm) are also seen in Figure 59. The K_{eq} coefficients in Figure 59 are approximately equal to the average of the K_{xx} and K_{yy} coefficients shown earlier in Figure 55.

Both sets of predictions (using the hot and cold measured clearances as inputs) predict larger K_{eq} coefficients than were measured. Predictions using the cold clearance predict lower K_{eq} coefficients than those using the hot clearance. This means that measurements are in better agreement with the predictions using the cold clearance. Figure 59 also shows that the measured and predicted K_{eq} coefficients do not vary significantly when increasing the unit load from 0 kPa to 117 kPa.

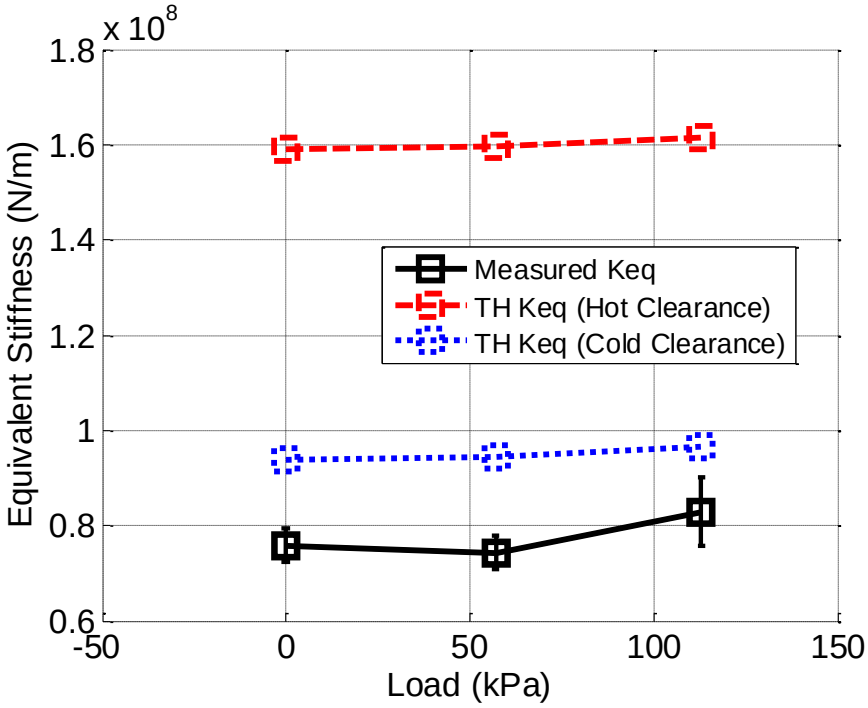

Figure 59. Vertical-application bearing K_{eq} coefficients at 2000 rpm

Figure 60 shows the measured and predicted K_{eq} coefficients vs. unit load at 9000 rpm. The same general trends regarding measurements vs. predictions seen in Figure 59 also apply to Figure 60. The K_{eq} coefficients in Figure 60 are approximately equal to the average of the K_{xx} and K_{yy} coefficients shown earlier in Figure 56. A comparison of Figures 59 and 60 shows that the predicted and measured K_{eq} coefficients are roughly three times larger at 9000 rpm than at 2000 rpm.

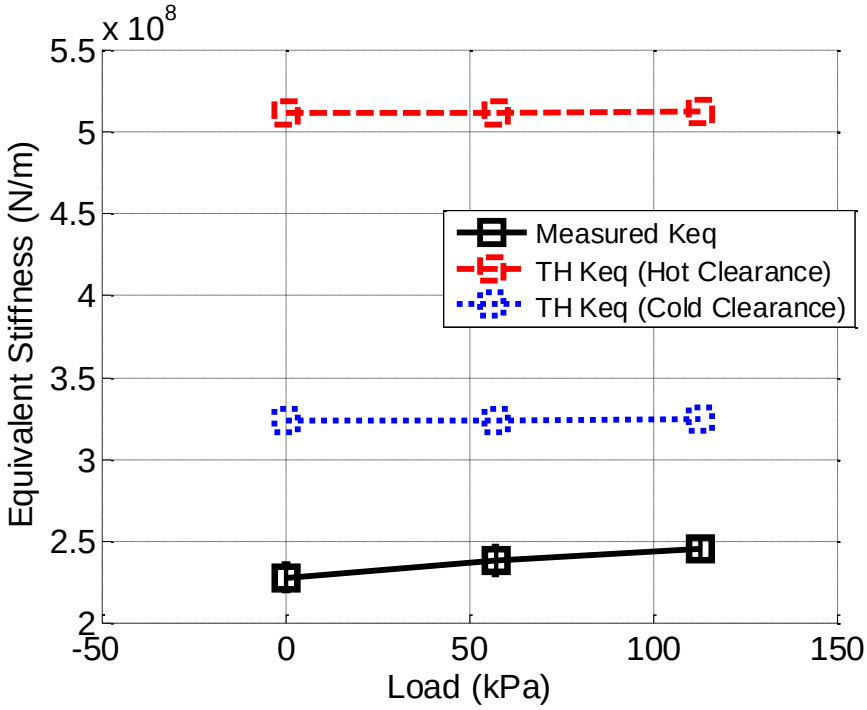

Figure 60. Vertical-application bearing K_{eq} coefficients at 9000 rpm

Direct Damping Coefficients

Figure 61 shows the measured and predicted C_{xx} and C_{yy} coefficients at 2000 rpm. The measured C_{xx} coefficients are generally larger than those predicted by both

sets of predictions at all three unit loads. The difference between the measured and predicted C_{xx} coefficients increases slightly with increasing load. The measured C_{yy} coefficients are larger than those predicted by both sets of predictions at 0 kPa. Agreement between the predicted and measured C_{yy} coefficients improves significantly with unit load. At 113 kPa, the measured C_{yy} coefficients are straddled by the two sets of predictions.

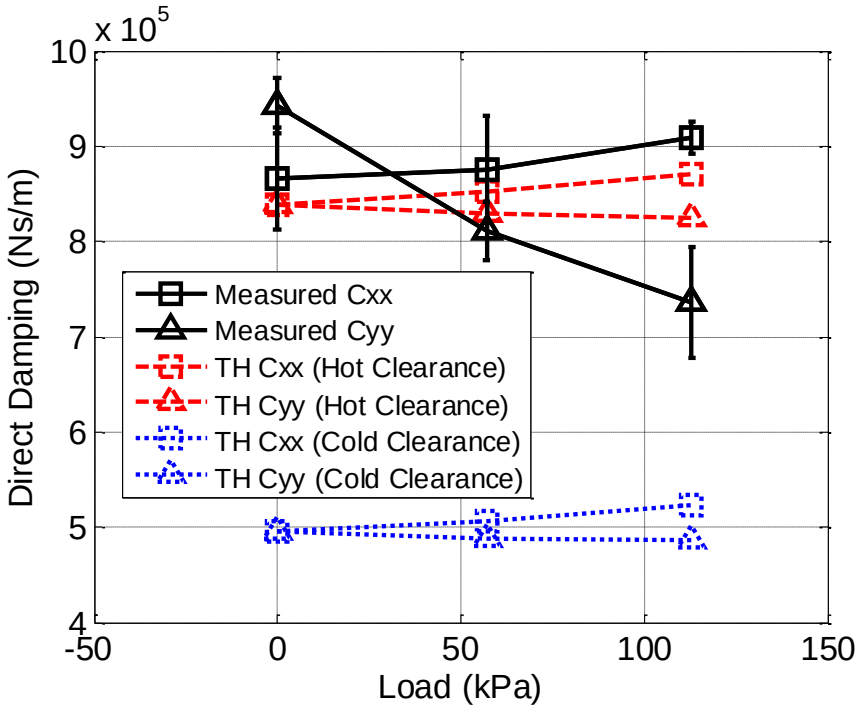

Figure 61. Vertical-application bearing C_{xx} and C_{yy} coefficients at 2000 rpm

Figure 62 shows the measured and predicted C_{xx} and C_{yy} coefficients at 9000 rpm. Agreement between measured and predicted C_{xx} and C_{yy} coefficients is very good at 9000 rpm. At both of these speeds, the measured coefficients are straddled by the two sets of predictions. At 9000 rpm, both C_{xx} and C_{yy} increase with increasing unit load. A

comparison of Figures 61 and 62 shows that the magnitude of both C_{xx} and C_{yy} decreases when increasing the running speed from 2000 rpm to 9000 rpm.

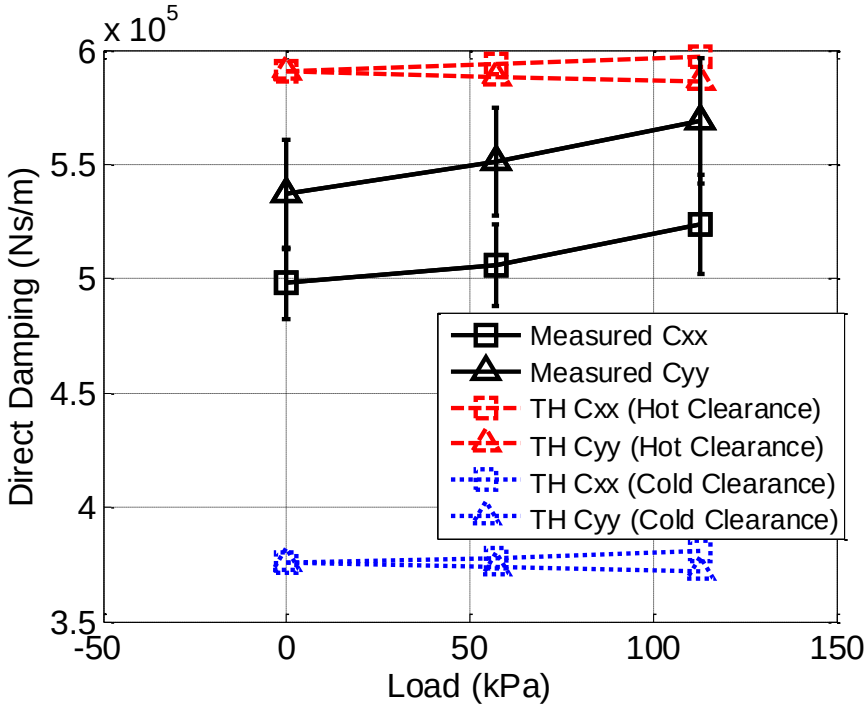

Figure 62. Vertical-application bearing C_{xx} and C_{yy} coefficients at 9000 rpm

Whirl-Frequency Ratios

Figure 63 shows the measured and predicted WFRs for the vertical-application bearing. WFRs for this bearing were calculated using Lund's [5] WFR formula, shown earlier in Eq. (6). The predicted value of 0.47 shown in Figure 59 applies to predictions run using either the hot or cold clearance. The vertical-application bearing is predicted to have a WFR of 0.47 at all three loads and all four speeds tested. In general, the

predicted WFR values closely agree with the measured WFR values. All test points produced a WFR between 0.39 and 0.46, except for the 2000 rpm, no-load case, which produced a WFR of 0.25. Thus, the vertical-application bearing does not offer a significant stability advantage, in terms of WFR, over a conventional plain-journal bearing or over the horizontal-application three-lobe bearing.

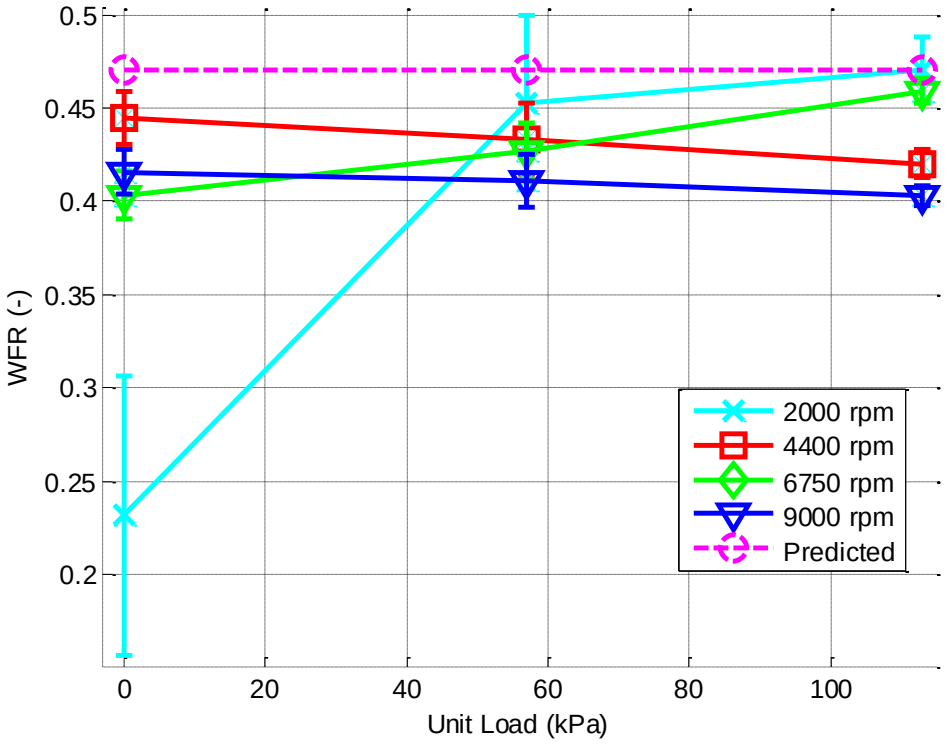

Figure 63. Measured and predicted WFRs for the vertical-application bearing

Comparison of Direct Stiffnesses for Both Bearings

Because the horizontal-application bearing and vertical-application bearing have different operating clearances and speeds, the dimensional rotordynamic coefficients presented thus far cannot be directly compared. The rotordynamic coefficients must be non-dimensionalized. Because zero-load test points are to be compared, Eq. (8a) cannot be used to non-dimensionalize the rotordynamic coefficients, because Eq. (8a) includes

load in the denominator. Thus, the direct and equivalent stiffness coefficients are non-dimensionalized using [1]:

$$\overline{k_{ij}} = \frac{2K_{ij}}{\mu\omega_s R_b}\left(\frac{C_b}{L}\right)^3, \tag{25}$$

where K_{ij} is any dimensional stiffness coefficient and $\overline{k_{ij}}$ is any non-dimensional stiffness coefficient. The non-dimensional equivalent stiffness coefficient, , was calculated using the same formula.

The $\overline{k_{jj}}$ and coefficients at 6750 rpm and 9000 rpm for both the horizontal-application bearing (100° load orientation) and the vertical-application bearing are summarized in Table 10. The measured hot-clearance is used to non-dimensionalize the coefficients. Note that the horizontal-application bearing 100° load orientation coefficients are used for this comparison, because the vertical-application bearing was also tested with a 100° load orientation.

Table 10 shows that the vertical-application bearing is stiffer by factors of 1.45 and 1.48 in the *y*-direction and factors of 1.15 and 1.26 in the *x*-direction. The equivalent stiffness for the vertical-application bearing is larger than that of the horizontal-application bearing by a factor of 1.33 at 6750 rpm and a factor of 1.25 at 9000 rpm. Thus, the vertical-application bearing does impart a larger centering force relative to the horizontal-application bearing at the no-load test point. In Leader's case study [6], the larger direct stiffness helped to enhance stability by increasing the pump's first critical speed.

Table 10. Comparison of Direct Stiffness Coefficients For Both Bearings

Coefficient	Horizontal-Application Bearing (100^o load orientation)	Vertical-Application Bearing	Vertical-Application Bearing Coefficient / Horizontal-Application Bearing Coefficient
$\overline{k_{xx}}$ at 6750 rpm / 0 kPa	.112	.141	1.26
$\overline{k_{xx}}$ at 9000 rpm / 0 kPa	.131	.151	1.15
$\overline{k_{yy}}$ at 6750 rpm / 0 kPa	.101	.149	1.48
$\overline{k_{yy}}$ at 9000 rpm / 0 kPa	.105	.153	1.46
$\overline{k_{eq}}$ at 6750 rpm / 0 kPa	.109	.145	**1.33**
$\overline{k_{eq}}$ at 9000 rpm / 0 kPa	.121	.151	**1.25**

SUMMARY, DISCUSSION, AND CONCLUSIONS

The purposes of this thesis are to: (1) characterize the load-angle orientation sensitivity of a horizontal-application (0.52 preload, 70% offset) three-lobe bearing in terms of static and dynamic performance, (2) measure and report the dynamic characteristics of the vertical-application (0.6 preload, 100% offset) three-lobe bearing, (3) compare measurements to predictions for both bearings, and (4) compare the characteristics of the two bearings.

The responses to these objectives are summarized below.

Characterize the Load-Angle Orientation Sensitivity of a Horizontal-Application Three-Lobe Bearing in Terms of Static and Dynamic Performance

Static tests show that the operating eccentricity is generally largest (lowest static stiffness) when the load vector is oriented towards either the trailing edge of the pad or the leading edge of the pad. Operating eccentricities are generally lowest (largest static stiffness) for the 20^o, 30^o, and 40^o load orientations. This effect is more pronounced at lower speeds and with larger static loads. Pettinato et al. [9] measured the SEP of a three-lobe bearing (0.75 preload, 50% offset) at three different load orientations, but their eccentricity measurements did not show a clear trend regarding load orientation.

In terms of thermal performance, the 30^o and 90^o load orientations yield slightly higher measured maximum temperature increases at speed than the other load orientations. This trend is not as prevalent with higher loads. This trend disagreed with that found by Pettinato et al. [9]. They found that load orientation does not affect the thermal behavior of the bearing, but their study was limited to only one speed and three load orientations. The author did not find any other previously-reported data regarding the thermal load-orientation sensitivity of a three-lobe bearing.

Dynamic tests show that the WFR for the horizontal-application three-lobe bearing is very sensitive to load orientation at low speeds and heavy loads. WFRs at 6750 rpm with loads of 1149 kPa, 1723 kPa, and 2298 kPa are zero for load orientations oriented towards either the leading edge of the pad or the center of the pad, and between 0.3 and 0.5 for load orientations oriented towards the trailing edge of the pad. This general trend agrees with the trend noted by Mehta et al.'s [10] analysis of a 0.5 preload, 50% offset three-lobe bearing. Mehta et al. showed that the OSI asymptotically increased as load orientation decreased below approximately 25^o. Hence, their analysis showed a WFR of zero for load orientations below 25^o. In Mehta's study, OSI decreased (WFR increased) as load orientation increased. Similarly, in this study, the WFR increased as the load orientation is increased. The WFR is not as sensitive to load orientation at light loads and high speeds. At 13200 rpm, measured WFRs are between 0.3 and 0.7 at all loads for all load orientations. Measured WFRs at the no-load condition are approximately 0.5-0.7 for all speeds and load orientations.

The K_{xx} coefficients are highest for the 0^o and 100^o load orientations, and the K_{yy} coefficients are highest for the 20^o, 30^o, 40^o, and 60^o load orientations. Pettinato et al. [9] reported that the 50^o load orientation had the highest K_{yy} coefficients and the lowest K_{xx} coefficients. While the 50^o load orientation is not tested in this study, Pettinato et al.'s results are confirmed in this study by the nearby 40^o and 60^o load orientations. Pettinato et al. also reported that the -10^o (load between pad) load orientation had the highest K_{xx} coefficients and the lowest K_{yy} coefficients. Once again, the nearby 0^o and 100^o load orientations tested in this study confirm this trend.

Orthotropy can also be used to enhance stability or change/split a critical speed. In this study, orthotropy was found to be a significant contributor to small WFRs at various test points. At 6750 rpm and 2298 kPa, the bearing is the most orthotropic when the static load orientation is 30^o and 40^o. At 13200 rpm and 2298 kPa, the bearing is very orthotropic for the 30^o, 40^o, 90^o, and 100^o load orientations. Previous studies did

not comment on observed orthotropy with respect to load orientation, or its effect on stability.

Overall, the results of this part of the study showed that, depending on the magnitude of the static load and the operating speed of the rotor, the static load orientation can play a significant role in the static and dynamic performance of a three-lobe bearing. If the static load orientation is unknown at the design stage or expected to change during normal operation of the machine, the three-lobe bearing is a poor choice. However, if the load orientation is known beforehand, the three-lobe bearing can be advantageously oriented to change/split a critical speed. However, in practical terms, stability is only an issue at high speeds and light loads. For those circumstances, WFR is largely independent of load orientation. Thus, load orientation cannot be used advantageously to provide higher stability; instead, a tilting-pad bearing should be used.

Measure and Report the Dynamic Characteristics of the Vertical-Application (100% Offset) Three-Lobe Bearing

Leader [6] used a 100% offset vertical-application three-lobe bearing design to stabilize a vertical sulfur pump. Leader's bearing design carried a WFR=0.17, calculated from his predicted rotordynamic coefficients. A bearing geometrically similar to Leader's was tested for this part of the study. The reported WFRs in this study were found to be between 0.4 and 0.5 for most cases.

Generally-speaking, the rotordynamic coefficients used to calculate the WFR were well-defined. Repeatabilities for most complex-dynamic stiffness coefficients for the vertical-application bearing were generally good. Re($\boldsymbol{H_{ij}}$) vs. Ω curve-fit R^2 values generally ranged from 0.4-0.7 in most cases. As such, M_{ij} was poorly-defined in most cases, but K_{ij} (y-intercept of the curve-fit) was generally well-defined. C_{xx} and C_{yy} were well-defined, with direct Im($\boldsymbol{H_{ij}}$) vs. Ω curve-fit R^2 values close to 1.00 in most cases.

C_{xy} and C_{yx} were generally poorly-defined, with uncertainties on or greater than the order of magnitude of the measured values.

Compare Measurements to Predictions For Both Bearings

For both bearings, the radial bearing clearance was measured prior to testing ("cold" condition) and immediately after spinning the rotor to the highest speed and applying the maximum unit load to the bearing ("hot" condition). Predictions for maximum-pad-metal-temperature-increases, static equilibrium eccentricity, and all rotordynamic coefficients were run using both the hot and cold clearances measurements.

For the horizontal-application bearing, pad-metal-temperature-increases are well-predicted when using the measured cold clearance value for the numerical solution at low speeds. Pad-metal-temperature-increases are well-predicted when using the measured hot clearance value for the numerical solution at high speeds.

For the horizontal-application bearing, the direct stiffnesses are generally well-predicted at low speeds. At high speeds, the K_{xx} coefficients are well-predicted, but the predicted K_{yy} coefficients are lower than measured values. The predicted K_{xy} and K_{yx} magnitudes are generally larger than the measured values. At the lower loads, the predictions match the measured data slightly better than at higher loads. The predicted C_{xx} and C_{yy} coefficients are generally larger than measured values, especially at higher loads.

Predictions using both the measured hot clearance and measured cold clearance for the vertical-application bearing were also compared to the measured dynamic data in this study. In general, the predicted direct stiffness coefficients (using clearance) are slightly larger than measured direct stiffnesses, but still on the same order of magnitude. Predictions using the hot clearance and predictions using the cold clearance straddle the

measured cross-coupled stiffness coefficients at all speeds. Predicted C_{xx} and C_{yy} coefficients (using either clearance) were larger than measured values at 2000 rpm. At 9000 rpm, the predicted C_{xx} and C_{yy} coefficients straddle the measured values.

Most previous load orientation studies fail to present or comment on both predictions and measurements. Such studies are generally confined to one or the other. Lanes and Flack [8], however, did report both measured and predicted OSI. In their study, discrepancies between measured and predicted OSI up to 45% were reported. Regarding predictions for multi-lobe bearings, Lanes and Flack's [8] conclude that "bearing calculations are inaccurate for preloaded bearings" and that "more fundamental experimental pressure profile data are needed for this bearing type before further improvements in the theoretical predictions can be made". They note that discrepancies between measurements and predictions are generally larger for multi-lobe bearings than pressure-dam bearings. The author agrees with Lanes and Flack's assessment. As stated earlier, the predicted and measured horizontal-application bearing rotordynamic coefficients reported in this study also show significant discrepancies at several test points.

Compare the Characteristics of Both Bearings

Leader [6] stated that the vertical-application bearing carried an advantage, relative to plain journal bearings, in terms of the centering force (direct stiffness) provided by the bearing, due to the pressure profile generated by the 100% offset geometry. Comparing the dimensionless direct stiffness coefficients to those of the horizontal-application bearing, the vertical-application clearly offers an advantage in terms of the centering force, as Leader [6] suggested. Dimensionless direct stiffness coefficients at 0 kPa are larger for the vertical-application bearing by factors of 1.45 and 1.48 in the *y*-direction and by factors of 1.15 and 1.26 in the *x*-direction. The equivalent stiffness for the vertical-application bearing is larger than that of the horizontal-

application bearing by a factor of 1.33 at 6750 rpm and a factor of 1.25 at 9000 rpm. Garner et al. [7] predicted that the 60% offset three-lobe bearing configuration has larger direct stiffness coefficients than the symmetric (50% offset) three-lobe bearing. This study complements Garner's work by showing that increasing the offset from 70% to 100% increases the magnitude of both direct stiffness coefficients.

Additionally, the stability characteristics of both bearings were compared. The vertical-application three-lobe bearing tested in this study does not provide a stability advantage in terms of WFR, relative to a standard plain journal bearing (approximately 0.5 WFR) or to the horizontal-application three-lobe bearing. As mentioned earlier, the measured WFR is between 0.4-0.5 for this bearing at nearly all test points. 0.5 is a "typical" WFR for most plain journal bearings. Garner et al. [7] predicted that the 60% offset three-lobe bearing configuration "enhanced stability". In this study, there is no discernable trend with respect to the measured WFR when comparing the horizontal-application (70% offset) three-lobe bearing to the vertical-application (70% offset) three-lobe bearing.

REFERENCES

[1] Vance, J., 1988, *Rotordynamics of Turbomachinery*. John Wiley & Sons, Inc., New York, NY, Chps. I II, VI, and VII.

[2] Allaire, P.E. and Flack, R.D., 1981, "Design of Journal Bearings for Rotating Machinery", Proceedings of The Tenth Turbomachinery Symposium, College Station, TX, pp. 25-45.

[3] Vannarsdall, M.L., 2010, "Measured Results For A New Hole-Pattern Annular Gas Seal Incorporating Larger Diameter Holes, Comparisons To Results For A Traditional Hole-Pattern Seal, And Predictions", M.S. Thesis. Texas A&M University, College Station, TX.

[4] Nicholas, J. and R. Moll, 1993, "Shifting Critical Speeds Out of the Operating Range by Changing from Tilting Pad to Sleeve Bearings," Proceedings, 22nd Turbomachinery Symposium, pp. 25-32.

[5] Lund, J., 1965, "The Stability of an Elastic Rotor in Journal Bearings with Flexible, Damped Supports," ASME J. of Applied Mechanics, pp. 911-920

[6] Leader, M., 2010, "Evaluating and Correcting Subsynchronous Vibration in Vertical Pumps," Case Study, The International Pump Users Symposium, Houston, Texas.

[7] Garner, D.R., Lee, C.S., and Martin, F.A., 1980, "Stability of Profile Bore Bearings Influence of Bearing Type Selection", Tribology International, **13**(5), pp. 204-210.

[8] Lanes, R.F. and Flack, R.D, 1982, "Effects of Three-Lobe Bearing Geometries on Flexible-Rotor Stability," ASLE Transactions, **25**(3), pp. 377-385.

[9] Pettinato, B. and Flack, R.D., 2001, "Test Results For a Highly Preloaded Three-Lobe Journal Bearing-Effect of Load Orientation on Static and Dynamic Characteristics", J. STLE, **57**(9), pp. 23--30.

[10] Mehta, N. P., Rattan, S. S., and Verma, A., 1992, "Combined Effect of Turbulence,

Load Orientation and Rotor Flexibility on the Performance of Three-lobe Bearings," Tribology Transactions, **35**(3), pp. 530-536.

[11] San Andrés, L. "Thermohydrodynamic analysis of hydrodynamic fluid film bearings". TRC Presentation. May 2008.

[12] Kaul, A., 1999, "Design and Development of a Test Setup for the Experimental Determination of the Rotordynamic and Leakage Characteristics of Annular Bushing Oil Seals," M.S. thesis, Mechanical Engineering, Texas A&M University, College Station, TX.

[13] Childs, D.W. et al, 2011, "Tilting-Pad Bearings: Measured Frequency Characteristics of their Rotordynamic Coefficients". Proceedings of the Fortieth Turbomachinery Symposium. John Wiley & Sons, Inc., New York, NY.

[14] Glienicke, J., 1966, "Experimental Investigation of Stiffness and Damping Coefficients of Turbine Bearings and Their Application to Instability Predictions," Proceedings of the IMechE., **181**, pp. 116-129.

[15] Wilkes, J., 2011, "Measured and Predicted Transfer Functions Between Rotor Motion and Pad Motion for a Rocker-Back Tilting-Pad Bearing in LOP Configuration", Ph.D. Dissertation, Texas A&M University, College Station, TX.

[16] Childs, D., and Hale, K., 1994, "A Test Apparatus and Facility to Identify the Rotordynamic Coefficients of High-Speed Hydrostatic Bearings," ASME J. of Trib., **116**, pp. 337-344.

[17] Childs, D.W., 1993, *Turbomachinery Rotordynamics: Phenomena Modeling and Analysis*. John Wiley & Sons, Inc., New York, NY.

[18] Pinkus, O., 1959, "Analysis and Characteristics of the Three-Lobe Bearing", ASME Journal of Basic Engineering, **81**, pp. 49-55.

[19] Gethin, D.T. and El-Deihi, M.K.I, 1987, "Effect of Loading Direction on the Performance of a Twin-Axial Groove Cylindrical-Bore Bearing," Tribology International, **20**(4), pp. 179-185.

[20] Leader, M.E. et al., 1980, "An Experimental Determination of the Instability of a

Flexible Rotor in Four-Lobe Bearings," Wear, **58**(1), pp. 35-47.

[21] Kulhanek, C.D., 2010, "Dynamic and Static Characteristics of a Rocker-Pivot, Tilting-Pad Bearing with 50% and 60% Offsets," M.S. thesis, Texas A&M University, College Station, TX.

[22] Stachowiak, G.W., 2005, *Engineering Tribology*. Elsevier, Inc., Burlington, MA.

APPENDIX A: HORIZONTAL-APPLICATION BEARING DYNAMIC DATA

Rotordynamic coefficients for the horizontal-application bearing are provided in this section.

Table A.1. Dynamic Coefficients and Repeatability for 0° Load Orientation

	Load	Kxx	Kxy	Kyx	Kyy	Cxx	Cyy	eKxx	eKxy	eKyx	eKyy	eCxx	eCyy
	kPa	N/m	N/m	N/m	N/m	N-s/m	N-s/m	N/m	N/m	N/m	N/m	N-s/m	N-s/m
6750 rpm	0	2.07E+08	1.64E+08	-2.37E+08	2.07E+08	4.46E+05	4.44E+05	4.42E+07	5.39E+07	1.94E+07	2.21E+07	3.85E+04	3.03E+04
	575	2.55E+08	7.24E+07	-3.13E+08	2.43E+08	4.35E+05	5.09E+05	1.46E+07	2.10E+07	3.96E+07	4.75E+07	1.77E+04	7.48E+04
	1149	3.56E+08	5.40E+06	-3.55E+08	3.53E+08	4.37E+05	6.00E+05	1.80E+07	1.25E+07	3.02E+07	6.18E+07	1.21E+04	4.40E+04
	1724	4.55E+08	-4.98E+07	-5.15E+08	4.95E+08	4.25E+05	6.29E+05	1.82E+07	2.25E+07	3.65E+07	5.12E+07	1.40E+04	8.18E+04
	2298	5.52E+08	-1.01E+08	-5.86E+08	6.42E+08	4.05E+05	6.23E+05	1.96E+07	3.33E+07	4.03E+07	5.97E+07	1.45E+04	1.03E+05
9000 rpm	0	2.9E+08	2.2E+08	-2.9E+08	2.9E+08	4.1E+05	4.6E+05	1.15E+08	1.44E+08	1.93E+08	2.27E+08	9.78E+04	1.66E+05
	575	3.5E+08	1.5E+08	-3.6E+08	3.1E+08	3.7E+05	4.3E+05	3.10E+07	2.17E+07	5.34E+07	6.54E+07	7.96E+04	5.12E+04
	1149	4.6E+08	7.7E+07	-4.5E+08	4.1E+08	3.4E+05	4.6E+05	2.94E+07	1.99E+07	2.45E+07	8.74E+07	1.66E+04	5.01E+04
	1724	5.7E+08	1.9E+07	-5.4E+08	5.5E+08	3.5E+05	4.7E+05	2.13E+07	1.82E+07	3.01E+07	4.92E+07	1.33E+04	5.62E+04
	2298	6.6E+08	-3.4E+07	-6.0E+08	6.8E+08	3.2E+05	4.6E+05	2.73E+07	4.84E+07	2.95E+07	9.54E+07	1.65E+04	1.65E+05
10800 rpm	0	3.7E+08	2.5E+08	-4.3E+08	3.6E+08	4.2E+05	4.7E+05	7.94E+07	1.13E+08	1.62E+08	1.61E+08	1.46E+05	1.32E+05
	575	4.5E+08	1.8E+08	-5.0E+08	3.8E+08	3.7E+05	4.3E+05	6.26E+07	3.81E+07	8.20E+07	6.08E+07	4.89E+04	8.93E+04
	1149	5.7E+08	1.1E+08	-5.8E+08	4.7E+08	3.4E+05	4.4E+05	2.43E+07	2.18E+07	2.45E+07	5.12E+07	2.33E+04	3.99E+04
	1724	6.8E+08	4.3E+07	-6.6E+08	5.9E+08	3.2E+05	4.2E+05	2.08E+07	2.68E+07	2.77E+07	3.50E+07	1.47E+04	1.00E+05
	2298	7.6E+08	-9.6E+06	-7.1E+08	7.2E+08	3.0E+05	3.9E+05	2.27E+07	2.39E+07	4.36E+07	1.03E+08	1.40E+04	4.03E+04
13200 rpm	0	6.03E+08	1.99E+08	-5.15E+08	5.77E+08	4.73E+05	5.35E+05	5.53E+07	5.59E+07	5.83E+07	6.77E+07	4.51E+04	7.11E+04
	575	6.98E+08	1.39E+08	-5.62E+08	5.55E+08	3.75E+05	4.79E+05	1.65E+07	1.43E+07	4.39E+07	3.26E+07	3.66E+04	3.13E+04
	1149	8.08E+08	1.39E+08	-6.12E+08	5.99E+08	3.51E+05	4.62E+05	1.05E+07	1.28E+07	1.80E+07	2.91E+07	1.24E+04	1.51E+04
	1724	9.10E+08	1.10E+08	-6.85E+08	6.89E+08	3.36E+05	4.23E+05	9.71E+06	1.04E+07	1.87E+07	2.25E+07	8.96E+03	3.11E+04
	2298	9.92E+08	7.18E+07	-7.37E+08	7.84E+08	3.12E+05	3.74E+05	1.18E+07	1.91E+07	2.46E+07	5.40E+07	8.59E+03	2.37E+04

Table A.2. Dynamic Coefficients and Repeatability for 20° Load Orientation

	Load	Kxx	Kxy	Kyx	Kyy	Cxx	Cyy	eKxx	eKxy	eKyx	eKyy	eCxx	eCyy
	kPa	N/m	N/m	N/m	N/m	N-s/m	N-s/m	N/m	N/m	N/m	N/m	N-s/m	N-s/m
6750 rpm	0	2.29E+08	1.42E+08	-2.44E+08	2.47E+08	4.80E+05	5.01E+05	1.63E+08	1.09E+08	7.52E+07	2.36E+07	1.02E+05	5.31E+04
	575	2.23E+08	8.19E+07	-3.12E+08	3.58E+08	4.29E+05	5.46E+05	1.10E+07	2.39E+07	3.51E+07	1.07E+08	8.35E+03	8.63E+04
	1149	2.54E+08	1.54E+07	-4.01E+08	5.25E+08	3.97E+05	6.01E+05	1.04E+07	2.61E+07	2.37E+07	7.04E+07	7.81E+03	5.71E+04
	1724	2.93E+08	-4.75E+07	-4.87E+08	7.01E+08	3.71E+05	6.39E+05	8.88E+06	2.24E+07	2.55E+07	6.49E+07	8.37E+03	1.08E+05
	2298	3.40E+08	-1.03E+08	-5.67E+08	8.84E+08	3.61E+05	6.96E+05	9.02E+06	3.48E+07	4.46E+07	1.52E+08	1.33E+04	1.99E+05
9000 rpm	0	3.3E+08	2.3E+08	-2.9E+08	3.5E+08	4.3E+05	4.8E+05	6.56E+07	2.56E+07	6.50E+07	5.08E+07	3.07E+04	3.74E+04
	575	3.3E+08	1.5E+08	-3.7E+08	4.7E+08	4.0E+05	4.9E+05	2.53E+07	2.54E+07	2.66E+07	7.21E+07	1.85E+04	6.58E+04
	1149	3.7E+08	6.7E+07	-4.6E+08	6.5E+08	3.7E+05	5.0E+05	2.22E+07	2.87E+07	2.52E+07	7.98E+07	1.74E+04	4.94E+04
	1724	4.1E+08	2.2E+06	-5.4E+08	8.1E+08	3.4E+05	5.3E+05	1.26E+07	2.63E+07	4.52E+07	5.79E+07	1.53E+04	1.07E+05
	2298	4.5E+08	-5.0E+07	-6.0E+08	9.7E+08	3.2E+05	5.4E+05	1.59E+07	2.28E+07	2.91E+07	1.22E+08	1.35E+04	9.27E+04
10800 rpm	0	4.6E+08	2.5E+08	-4.4E+08	4.9E+08	4.2E+05	5.2E+05	2.99E+07	3.08E+07	4.45E+07	6.33E+07	6.61E+04	3.82E+04
	575	4.8E+08	1.5E+08	-5.3E+08	6.0E+08	4.0E+05	4.9E+05	2.80E+07	2.66E+07	3.69E+07	8.06E+07	2.99E+04	7.91E+04
	1149	5.1E+08	5.8E+07	-6.2E+08	7.6E+08	3.8E+05	5.1E+05	1.82E+07	2.91E+07	2.74E+07	7.18E+07	1.72E+04	5.17E+04
	1724	5.5E+08	-4.6E+06	-6.9E+08	9.1E+08	3.5E+05	4.9E+05	1.17E+07	2.64E+07	2.81E+07	6.34E+07	1.41E+04	8.12E+04
	2298	5.8E+08	-5.6E+07	-7.4E+08	1.0E+09	3.3E+05	4.8E+05	1.04E+07	4.03E+07	5.13E+07	1.07E+08	2.12E+04	1.99E+05
13200 rpm	0	7.21E+08	1.60E+08	-5.20E+08	6.60E+08	3.94E+05	5.88E+05	2.93E+07	1.84E+07	3.28E+07	2.26E+07	3.12E+04	2.94E+04
	575	7.52E+08	2.51E+08	-4.91E+08	7.39E+08	3.90E+05	5.49E+05	2.14E+07	1.50E+07	1.99E+07	3.41E+07	4.06E+04	5.27E+04
	1149	8.06E+08	2.10E+08	-4.34E+08	8.43E+08	3.65E+05	5.41E+05	6.70E+06	1.59E+07	1.98E+07	4.30E+07	2.17E+04	2.20E+04
	1724	7.92E+08	1.11E+08	-4.55E+08	9.28E+08	3.46E+05	5.08E+05	6.39E+06	1.26E+07	2.18E+07	3.26E+07	1.32E+04	5.27E+04
	2298	8.40E+08	1.68E+08	-5.65E+08	1.05E+09	3.28E+05	4.89E+05	6.52E+06	1.75E+07	1.85E+07	6.67E+07	1.35E+04	4.94E+04

Table A.3. Dynamic Coefficients and Repeatability for 30° Load Orientation

	Load	Kxx	Kxy	Kyx	Kyy	Cxx	Cyy	eKxx	eKxy	eKyx	eKyy	eCxx	eCyy
	kPa	N/m	N/m	N/m	N/m	N-s/m	N-s/m	N/m	N/m	N/m	N/m	N-s/m	N-s/m
6750 rpm	0	2.03E+08	1.63E+08	-2.31E+08	3.75E+08	4.86E+05	5.38E+05	2.88E+07	3.13E+07	5.86E+07	1.17E+08	1.37E+04	1.51E+05
	575	2.12E+08	1.12E+08	-2.88E+08	5.25E+08	4.69E+05	6.12E+05	1.94E+07	3.23E+07	6.38E+07	1.05E+08	1.56E+04	1.41E+05
	1149	2.28E+08	5.05E+07	-3.52E+08	7.00E+08	4.53E+05	6.38E+05	1.43E+07	3.15E+07	3.80E+07	1.01E+08	1.32E+04	1.35E+05
	1724	2.43E+08	-1.06E+07	-4.20E+08	8.92E+08	4.29E+05	6.49E+05	1.33E+07	2.82E+07	4.86E+07	8.50E+07	1.28E+04	1.74E+05
	2298	2.63E+08	-6.66E+07	-4.81E+08	1.08E+09	4.03E+05	6.36E+05	1.16E+07	2.42E+07	2.15E+07	2.06E+08	1.09E+04	1.28E+05
9000 rpm	0	2.6E+08	2.4E+08	-2.7E+08	4.9E+08	4.0E+05	5.3E+05	1.63E+07	2.81E+07	1.78E+07	3.51E+07	1.13E+04	4.19E+04
	575	2.7E+08	1.8E+08	-3.3E+08	6.3E+08	3.9E+05	5.8E+05	1.41E+07	2.85E+07	1.68E+07	7.21E+07	9.98E+03	6.77E+04
	1149	2.8E+08	1.2E+08	-3.9E+08	8.0E+08	3.7E+05	6.0E+05	1.17E+07	2.84E+07	2.21E+07	7.55E+07	9.56E+03	8.34E+04
	1724	3.0E+08	6.0E+07	-4.5E+08	9.7E+08	3.5E+05	6.1E+05	8.86E+06	2.43E+07	1.94E+07	8.14E+07	9.64E+03	9.22E+04
	2298	3.2E+08	1.1E+07	-5.0E+08	1.1E+09	3.4E+05	5.9E+05	9.38E+06	2.15E+07	1.85E+07	1.19E+08	8.66E+03	8.23E+04
10800 rpm	0	3.3E+08	2.7E+08	-4.2E+08	5.9E+08	3.7E+05	4.8E+05	2.06E+07	2.07E+07	1.54E+07	3.77E+07	1.52E+04	4.70E+04
	575	3.4E+08	2.0E+08	-4.8E+08	7.4E+08	3.6E+05	5.2E+05	1.53E+07	2.54E+07	2.86E+07	6.98E+07	1.37E+04	6.36E+04
	1149	3.5E+08	2.0E+08	-5.4E+08	9.1E+08	3.4E+05	5.1E+05	9.71E+06	2.58E+07	2.06E+07	7.17E+07	9.34E+03	8.05E+04
	1724	3.6E+08	7.5E+07	-5.8E+08	1.1E+09	3.2E+05	5.3E+05	8.56E+06	2.21E+07	3.26E+07	7.20E+07	8.95E+03	1.05E+05
	2298	3.8E+08	3.0E+07	-6.3E+08	1.2E+09	3.0E+05	5.1E+05	7.68E+06	2.12E+07	1.57E+07	1.29E+08	8.77E+03	8.58E+04
13200 rpm	0	4.90E+08	2.07E+08	-4.95E+08	5.80E+08	4.67E+05	4.58E+05	1.05E+07	9.23E+06	4.41E+07	9.21E+07	7.76E+03	8.81E+04
	575	4.93E+08	2.38E+08	-5.91E+08	7.43E+08	4.59E+05	4.17E+05	5.00E+06	1.18E+07	1.14E+07	3.83E+07	7.02E+03	3.99E+04
	1149	4.85E+08	1.77E+08	-6.20E+08	8.53E+08	4.45E+05	4.31E+05	4.34E+06	1.33E+07	1.17E+07	3.88E+07	4.48E+03	4.02E+04
	1724	4.99E+08	1.75E+08	-7.23E+08	1.00E+09	4.19E+05	4.24E+05	3.44E+06	1.10E+07	1.15E+07	4.23E+07	3.66E+03	4.68E+04
	2298	4.93E+08	1.97E+08	-8.23E+08	1.12E+09	3.82E+05	3.65E+05	3.50E+06	7.97E+06	2.49E+07	6.79E+07	3.58E+03	5.21E+04

Table A.4. Dynamic Coefficients and Repeatability for 40° Load Orientation

	Load	Kxx	Kxy	Kyx	Kyy	Cxx	Cyy	eKxx	eKxy	eKyx	eKyy	eCxx	eCyy
	kPa	N/m	N/m	N/m	N/m	N-s/m	N-s/m	N/m	N/m	N/m	N/m	N-s/m	N-s/m
6750 rpm	0	2.11E+08	1.48E+08	-2.30E+08	2.32E+08	4.66E+05	4.91E+05	6.77E+07	4.97E+07	5.15E+07	4.39E+07	5.04E+04	2.45E+04
	575	1.77E+08	1.63E+08	-2.26E+08	3.63E+08	4.35E+05	4.96E+05	4.34E+07	3.16E+07	1.02E+08	8.22E+07	1.08E+05	7.37E+04
	1149	1.77E+08	1.51E+08	-2.46E+08	5.53E+08	4.33E+05	5.28E+05	3.28E+07	3.33E+07	5.36E+07	1.10E+08	2.11E+04	7.76E+04
	1724	1.85E+08	1.27E+08	-2.74E+08	7.68E+08	4.28E+05	5.76E+05	1.94E+07	3.49E+07	2.09E+07	8.85E+07	1.84E+04	1.21E+05
	2298	1.95E+08	9.80E+07	-3.07E+08	9.86E+08	4.29E+05	6.31E+05	1.77E+07	3.57E+07	5.13E+07	1.66E+08	1.98E+04	1.38E+05
9000 rpm	0	2.74E+08	2.39E+08	-2.60E+08	3.07E+08	4.04E+05	4.35E+05	1.6E+08	1.3E+08	1.4E+08	1.5E+08	9.0E+04	6.5E+04
	575	2.37E+08	2.52E+08	-2.56E+08	4.51E+08	3.93E+05	4.35E+05	1.3E+08	6.1E+07	1.9E+08	1.7E+08	9.6E+04	4.8E+04
	1149	2.30E+08	2.30E+08	-2.81E+08	6.64E+08	3.82E+05	4.16E+05	3.7E+07	2.8E+07	5.1E+07	6.4E+07	3.5E+04	1.5E+05
	1724	2.35E+08	2.02E+08	-3.06E+08	8.76E+08	3.76E+05	4.27E+05	1.9E+07	3.2E+07	3.5E+07	1.4E+08	1.6E+04	1.1E+05
	2298	2.45E+08	1.75E+08	-3.28E+08	1.06E+09	3.67E+05	4.72E+05	1.4E+07	3.0E+07	2.9E+07	9.9E+07	1.6E+04	1.7E+05
10800 rpm	0	3.60E+08	2.70E+08	-4.00E+08	4.10E+08	4.30E+05	4.80E+05	2.0E+08	1.1E+08	1.1E+08	1.4E+08	4.1E+04	3.6E+04
	575	3.20E+08	2.80E+08	-4.10E+08	5.90E+08	4.20E+05	4.60E+05	6.1E+07	2.3E+07	1.1E+08	9.3E+07	3.7E+04	6.9E+04
	1149	3.00E+08	2.50E+08	-4.30E+08	8.10E+08	4.20E+05	4.10E+05	3.4E+07	2.7E+07	2.3E+07	7.4E+07	2.1E+04	1.0E+05
	1724	3.00E+08	2.10E+08	-4.50E+08	1.00E+09	4.00E+05	3.90E+05	1.7E+07	3.0E+07	4.6E+07	1.1E+08	1.6E+04	1.4E+05
	2298	3.10E+08	1.80E+08	-4.70E+08	1.20E+09	3.80E+05	4.20E+05	1.1E+07	2.5E+07	2.6E+07	1.2E+08	1.5E+04	1.6E+05
13200 rpm	0	5.44E+08	2.31E+08	-4.67E+08	4.46E+08	4.82E+05	5.70E+05	3.66E+07	2.24E+07	8.11E+07	8.84E+07	1.48E+05	4.45E+04
	575	5.04E+08	2.22E+08	-4.75E+08	6.23E+08	4.86E+05	5.62E+05	1.29E+07	1.95E+07	7.14E+07	4.58E+07	4.10E+04	7.11E+04
	1149	4.88E+08	1.63E+08	-5.12E+08	8.55E+08	4.82E+05	4.66E+05	1.31E+07	1.64E+07	1.19E+07	4.70E+07	1.25E+04	3.03E+04
	1724	4.69E+08	2.36E+08	-5.55E+08	1.04E+09	4.76E+05	4.45E+05	6.70E+06	1.80E+07	1.88E+07	4.08E+07	7.84E+03	1.10E+05
	2298	4.44E+08	2.71E+08	-6.01E+08	1.21E+09	4.59E+05	4.39E+05	4.33E+06	1.59E+07	7.90E+06	8.00E+07	6.90E+03	3.76E+04

Table A.5. Dynamic Coefficients and Repeatability for 60° Load Orientation

	Load	Kxx	Kxy	Kyx	Kyy	Cxx	Cyy	eKxx	eKxy	eKyx	eKyy	eCxx	eCyy
	kPa	N/m	N/m	N/m	N/m	N-s/m	N-s/m	N/m	N/m	N/m	N/m	N-s/m	N-s/m
6750 rpm	575	1.69E+08	1.86E+08	-1.43E+08	2.89E+08	4.04E+05	4.04E+05	2.90E+07	1.22E+07	1.11E+07	3.65E+07	1.67E+04	1.95E+04
	1149	1.74E+08	1.98E+08	-1.46E+08	4.48E+08	4.31E+05	4.48E+05	3.49E+07	1.94E+07	1.10E+07	5.09E+07	2.37E+04	2.56E+04
	1724	1.90E+08	1.95E+08	-1.48E+08	6.57E+08	4.59E+05	4.70E+05	2.28E+07	2.13E+07	6.72E+07	5.41E+07	3.82E+04	3.29E+04
	2298	2.13E+08	1.80E+08	-1.68E+08	8.76E+08	4.84E+05	5.26E+05	5.46E+07	2.33E+07	1.34E+07	5.93E+07	2.55E+04	4.48E+04
9000 rpm	575	2.2E+08	1.3E+08	-8.8E+07	3.5E+08	3.8E+05	3.8E+05	2.19E+07	1.12E+07	1.68E+07	3.88E+07	1.51E+04	1.70E+04
	1149	2.3E+08	1.3E+08	-9.0E+07	5.3E+08	3.9E+05	4.0E+05	3.49E+07	1.26E+07	1.67E+07	4.46E+07	1.61E+04	1.92E+04
	1724	2.4E+08	1.2E+08	-9.4E+07	7.1E+08	4.0E+05	4.2E+05	3.36E+07	1.60E+07	1.55E+07	5.22E+07	1.95E+04	2.52E+04
	2298	2.6E+08	1.0E+08	-1.0E+08	9.1E+08	3.9E+05	4.2E+05	3.33E+07	1.40E+07	1.45E+07	5.59E+07	1.85E+04	2.77E+04
10800 rpm	575	2.7E+08	2.9E+08	-2.5E+08	4.2E+08	3.9E+05	3.9E+05	1.43E+07	1.37E+07	1.66E+07	4.99E+07	1.23E+04	1.69E+04
	1149	2.7E+08	2.9E+08	-2.5E+08	5.9E+08	4.0E+05	4.0E+05	2.14E+07	9.48E+06	2.02E+07	5.10E+07	2.47E+04	2.03E+04
	1724	2.8E+08	2.7E+08	-2.5E+08	7.8E+08	4.0E+05	4.1E+05	2.64E+07	6.81E+06	1.96E+07	5.40E+07	2.49E+04	2.34E+04
	2298	3.0E+08	2.5E+08	-2.5E+08	9.6E+08	3.9E+05	4.1E+05	5.70E+07	1.48E+07	1.81E+07	5.73E+07	2.38E+04	2.79E+04

Table A.6. Dynamic Coefficients and Repeatability for 80° Load Orientation

	Load	Kxx	Kxy	Kyx	Kyy	Cxx	Cyy	eKxx	eKxy	eKyx	eKyy	eCxx	eCyy
	kPa	N/m	N/m	N/m	N/m	N-s/m	N-s/m	N/m	N/m	N/m	N/m	N-s/m	N-s/m
6750 rpm	0	2.73E+08	1.50E+08	-2.27E+08	2.32E+08	5.21E+05	4.40E+05	4.92E+07	5.30E+07	3.73E+07	5.15E+07	6.08E+04	7.35E+04
	575	3.52E+08	2.01E+08	-2.02E+08	2.27E+08	5.98E+05	4.02E+05	2.79E+07	2.36E+07	2.68E+07	4.62E+07	2.58E+04	9.66E+04
	1149	5.03E+08	2.39E+08	-2.09E+08	3.33E+08	7.12E+05	4.21E+05	3.72E+07	2.95E+07	2.05E+07	6.02E+07	4.88E+04	3.15E+04
	1724	6.71E+08	2.70E+08	-2.12E+08	4.76E+08	7.78E+05	4.30E+05	5.09E+07	3.33E+07	3.83E+07	5.98E+07	8.22E+04	5.18E+04
	2298	8.23E+08	2.80E+08	-2.09E+08	6.25E+08	7.90E+05	4.31E+05	5.57E+07	3.23E+07	3.38E+07	6.73E+07	7.55E+04	1.43E+05
9000 rpm	0	3.5E+08	2.5E+08	-2.6E+08	2.9E+08	4.6E+05	3.9E+05	4.80E+07	6.63E+07	3.88E+07	2.88E+07	7.38E+04	5.41E+04
	575	4.5E+08	3.2E+08	-2.1E+08	3.0E+08	5.1E+05	3.5E+05	4.30E+07	2.77E+07	3.53E+07	4.56E+07	4.12E+04	9.68E+04
	1149	6.1E+08	3.5E+08	-2.0E+08	4.2E+08	5.7E+05	3.3E+05	4.48E+07	3.67E+07	2.35E+07	5.78E+07	5.03E+04	2.72E+04
	1724	7.7E+08	3.7E+08	-1.9E+08	5.5E+08	6.1E+05	3.0E+05	5.00E+07	4.40E+07	3.27E+07	6.06E+07	6.01E+04	5.07E+04
	2298	9.3E+08	3.8E+08	-1.8E+08	6.9E+08	6.3E+05	2.9E+05	5.38E+07	4.58E+07	3.12E+07	6.34E+07	6.73E+04	1.54E+05
10800 rpm	0	4.3E+08	3.0E+08	-3.9E+08	3.6E+08	4.6E+05	3.8E+05	8.02E+07	1.19E+08	9.05E+07	6.37E+07	1.38E+05	8.23E+04
	575	5.7E+08	3.7E+08	-3.2E+08	3.9E+08	5.1E+05	3.5E+05	4.61E+07	2.65E+07	3.24E+07	4.52E+07	4.83E+04	9.80E+04
	1149	7.1E+08	4.0E+08	-2.9E+08	5.0E+08	5.4E+05	3.1E+05	4.64E+07	3.80E+07	2.65E+07	6.08E+07	5.26E+04	2.51E+04
	1724	8.7E+08	4.2E+08	-2.7E+08	6.2E+08	5.8E+05	2.4E+05	4.91E+07	4.68E+07	3.44E+07	6.37E+07	5.91E+04	6.01E+04
	2298	1.0E+09	4.3E+08	-2.4E+08	7.6E+08	5.8E+05	2.4E+05	5.07E+07	4.95E+07	3.55E+07	5.45E+07	6.12E+04	1.70E+05
13200 rpm	0	7.64E+08	2.81E+08	-4.45E+08	6.06E+08	5.61E+05	4.29E+05	7.87E+07	5.99E+07	5.66E+07	1.12E+08	4.76E+04	1.03E+05
	575	7.86E+08	3.74E+08	-3.22E+08	7.62E+08	5.84E+05	3.64E+05	1.99E+07	1.40E+07	1.79E+07	2.75E+07	2.66E+04	3.63E+04
	1149	9.24E+08	4.04E+08	-2.53E+08	8.59E+08	6.03E+05	3.32E+05	2.67E+07	2.07E+07	1.86E+07	3.10E+07	2.65E+04	1.13E+04
	1724	1.05E+09	4.16E+08	-2.31E+08	9.39E+08	6.07E+05	2.78E+05	2.74E+07	2.40E+07	2.21E+07	3.29E+07	2.78E+04	2.49E+04
	2298	1.19E+09	4.18E+08	-1.80E+08	1.03E+09	5.97E+05	2.56E+05	2.72E+07	2.29E+07	1.82E+07	3.48E+07	2.71E+04	5.70E+04

Table A.7. Dynamic Coefficients and Repeatability for 90° Load Orientation

	Load	Kxx	Kxy	Kyx	Kyy	Cxx	Cyy	eKxx	eKxy	eKyx	eKyy	eCxx	eCyy
	kPa	N/m	N/m	N/m	N/m	N-s/m	N-s/m	N/m	N/m	N/m	N/m	N-s/m	N-s/m
6750 rpm	0	1.64E+08	1.28E+08	-2.82E+08	1.87E+08	4.92E+05	4.16E+05	1.14E+07	2.01E+07	1.78E+07	1.10E+07	2.84E+04	9.98E+03
	575	3.56E+08	1.41E+08	-1.91E+08	2.04E+08	6.14E+05	4.20E+05	1.89E+07	1.98E+07	2.25E+07	5.18E+07	4.23E+04	3.24E+04
	1149	4.58E+08	1.60E+08	-2.03E+08	2.94E+08	6.37E+05	4.81E+05	3.57E+07	1.77E+07	3.15E+07	8.22E+07	5.52E+04	7.16E+04
	1724	6.10E+08	1.68E+08	-2.16E+08	4.32E+08	6.46E+05	4.94E+05	1.02E+08	2.80E+07	4.21E+07	5.95E+07	1.06E+05	8.80E+04
	2298	8.57E+08	1.79E+08	-2.08E+08	5.95E+08	6.25E+05	5.31E+05	5.35E+07	2.75E+07	3.89E+07	1.08E+08	6.06E+04	5.15E+04
9000 rpm	0	3.8E+08	2.0E+08	-3.0E+08	2.4E+08	3.7E+05	3.7E+05	7.04E+07	4.09E+07	1.49E+07	2.09E+07	1.64E+05	1.31E+04
	575	5.7E+08	2.3E+08	-3.2E+08	2.7E+08	4.8E+05	3.8E+05	6.92E+07	2.58E+07	2.00E+07	4.44E+07	1.53E+05	2.58E+04
	1149	8.0E+08	2.3E+08	-3.7E+08	3.7E+08	4.8E+05	3.5E+05	4.58E+07	2.21E+07	2.73E+07	7.73E+07	4.56E+04	3.65E+04
	1724	9.2E+08	2.4E+08	-3.6E+08	4.8E+08	5.4E+05	4.1E+05	5.55E+07	2.25E+07	3.71E+07	6.46E+07	5.26E+04	8.04E+04
	2298	1.1E+09	2.7E+08	-3.6E+08	6.3E+08	5.1E+05	3.9E+05	6.05E+07	2.54E+07	3.46E+07	9.03E+07	5.82E+04	5.45E+04
10800 rpm	0	5.2E+08	2.4E+08	-4.3E+08	3.1E+08	4.1E+05	3.4E+05	3.61E+07	2.65E+07	1.20E+07	2.00E+07	3.37E+04	2.33E+04
	575	6.8E+08	2.7E+08	-4.3E+08	3.3E+08	4.1E+05	3.4E+05	5.20E+07	2.36E+07	3.36E+07	5.68E+07	6.56E+04	3.08E+04
	1149	9.0E+08	2.7E+08	-4.4E+08	4.3E+08	4.3E+05	3.3E+05	2.81E+07	2.58E+07	2.98E+07	5.34E+07	4.13E+04	7.82E+04
	1724	9.7E+08	2.7E+08	-4.4E+08	5.4E+08	4.4E+05	3.6E+05	7.49E+07	2.74E+07	4.91E+07	7.30E+07	7.08E+04	6.15E+04
	2298	1.2E+09	2.7E+08	-5.2E+08	6.6E+08	4.5E+05	3.4E+05	5.61E+07	3.10E+07	3.22E+07	5.08E+07	6.20E+04	1.32E+05
13200 rpm	0	7.15E+08	2.44E+08	-4.69E+08	4.60E+08	4.65E+05	4.22E+05	2.14E+07	4.01E+07	1.75E+07	4.46E+07	4.53E+04	3.48E+04
	575	9.30E+08	3.70E+08	-4.06E+08	5.04E+08	5.75E+05	4.18E+05	2.73E+07	1.91E+07	2.03E+07	2.90E+07	3.06E+04	2.29E+04
	1149	1.15E+09	3.82E+08	-3.79E+08	5.94E+08	5.19E+05	3.96E+05	2.00E+07	1.23E+07	2.41E+07	1.96E+07	1.92E+04	4.02E+04
	1724	1.28E+09	3.99E+08	-3.67E+08	6.72E+08	4.89E+05	3.81E+05	2.86E+07	1.35E+07	2.29E+07	3.03E+07	2.02E+04	2.63E+04
	2298	1.34E+09	4.11E+08	-3.91E+08	7.46E+08	4.78E+05	3.75E+05	3.38E+07	1.31E+07	2.23E+07	2.96E+07	2.52E+04	3.83E+04

Table A.8. Dynamic Coefficients and Repeatability for 100° Load Orientation

	Load	Kxx	Kxy	Kyx	Kyy	Cxx	Cyy	eKxx	eKxy	eKyx	eKyy	eCxx	eCyy
	kPa	N/m	N/m	N/m	N/m	N-s/m	N-s/m	N/m	N/m	N/m	N/m	N-s/m	N-s/m
6750 rpm	0	2.25E+08	1.34E+08	-2.35E+08	2.03E+08	4.49E+05	4.28E+05	1.24E+08	2.08E+07	7.55E+07	1.63E+07	8.45E+04	1.01E+05
	575	3.35E+08	1.51E+08	-1.90E+08	2.02E+08	5.12E+05	4.10E+05	1.44E+07	6.31E+07	1.51E+08	6.15E+07	1.24E+05	1.03E+05
	1149	4.86E+08	1.64E+08	-2.01E+08	2.72E+08	5.95E+05	4.49E+05	5.77E+07	3.75E+07	3.67E+07	6.41E+07	6.69E+04	3.95E+04
	1724	6.59E+08	1.76E+08	-2.08E+08	4.06E+08	5.93E+05	4.85E+05	5.11E+07	4.50E+07	4.39E+07	4.23E+07	5.03E+04	4.81E+04
	2298	8.00E+08	1.86E+08	-2.17E+08	5.46E+08	5.48E+05	4.70E+05	9.27E+07	1.34E+07	5.01E+07	4.76E+07	7.92E+04	9.96E+04
9000 rpm	0	3.5E+08	1.8E+08	-2.7E+08	2.8E+08	4.2E+05	3.7E+05	8.03E+07	1.02E+08	9.59E+07	1.11E+08	1.30E+05	1.32E+05
	575	6.8E+08	2.8E+08	-3.1E+08	2.9E+08	4.8E+05	3.8E+05	1.09E+08	1.13E+08	1.16E+08	5.37E+07	1.34E+05	8.71E+04
	1149	8.2E+08	3.1E+08	-3.7E+08	3.5E+08	5.0E+05	3.8E+05	1.07E+08	9.88E+07	3.73E+07	5.49E+07	6.17E+04	3.18E+04
	1724	9.0E+08	3.1E+08	-4.0E+08	4.6E+08	5.1E+05	3.7E+05	9.80E+07	8.87E+07	4.19E+07	3.79E+07	5.38E+04	3.67E+04
	2298	1.2E+09	3.3E+08	-4.3E+08	5.7E+08	5.2E+05	3.5E+05	8.47E+07	9.24E+07	4.63E+07	3.80E+07	6.86E+04	8.18E+04
10800 rpm	0	4.8E+08	2.3E+08	-4.1E+08	3.6E+08	4.8E+05	3.7E+05	1.25E+08	1.47E+08	9.21E+07	1.85E+08	1.03E+05	2.38E+05
	575	5.9E+08	2.8E+08	-3.9E+08	3.3E+08	5.1E+05	3.8E+05	1.07E+08	1.29E+08	9.00E+07	9.13E+07	2.00E+05	9.83E+04
	1149	8.1E+08	2.9E+08	-4.3E+08	4.3E+08	4.7E+05	4.0E+05	8.21E+07	6.28E+07	3.91E+07	5.49E+07	4.75E+04	3.49E+04
	1724	9.9E+08	2.7E+08	-4.5E+08	5.5E+08	4.9E+05	3.5E+05	5.95E+07	8.25E+07	4.69E+07	3.93E+07	3.48E+04	3.36E+04
	2298	1.1E+09	3.0E+08	-4.7E+08	6.5E+08	5.1E+05	3.0E+05	8.29E+07	9.23E+07	4.54E+07	4.18E+07	7.66E+04	7.80E+04
13200 rpm	0	6.83E+08	3.08E+08	-4.16E+08	5.45E+08	4.90E+05	4.06E+05	1.10E+07	1.06E+07	8.49E+06	6.27E+07	1.79E+05	8.20E+04
	575	8.68E+08	3.74E+08	-3.86E+08	4.94E+08	5.07E+05	4.00E+05	9.43E+06	1.09E+07	2.82E+07	5.80E+06	1.08E+05	9.33E+04
	1149	1.22E+09	4.01E+08	-3.85E+08	5.67E+08	4.98E+05	3.70E+05	1.17E+07	1.29E+07	2.66E+07	2.79E+07	3.17E+04	1.41E+04
	1724	1.25E+09	4.15E+08	-3.97E+08	5.76E+08	4.93E+05	3.58E+05	7.96E+06	1.29E+07	2.34E+07	2.19E+07	4.21E+04	2.48E+04
	2298	1.33E+09	4.26E+08	-4.01E+08	6.18E+08	4.90E+05	3.57E+05	7.89E+06	1.66E+07	2.38E+07	2.18E+07	6.18E+04	4.65E+04

APPENDIX B: VERTICAL-APPLICATION BEARING DYNAMIC DATA

Rotordynamic coefficients for the vertical-application bearing are provided in this section.

Table B.1. Dynamic Coefficients and Repeatability for the Vertical-Application Bearing

	Load (kPa)	Kxx (N/m)	Kxy (N/m)	Kyx (N/m)	Kyy (N/m)	Cxx (Ns/m)	Cyy (Ns/m)	eKxx (N/m)	eKxy (N/M)	eKyx (N/m)	eKyy (N/m)	eCxx (Ns/m)	eCyy (Ns/m)
2000 rpm	0	7.44E+07	1.42E+08	-1.37E+07	7.86E+07	8.68E+05	9.48E+05	3.68E+06	1.01E+07	1.76E+07	5.32E+06	5.30E+04	2.92E+04
	58	7.49E+07	1.44E+08	-5.52E+07	7.51E+07	8.84E+05	8.30E+05	3.76E+06	1.15E+07	2.13E+07	5.38E+06	5.53E+04	3.01E+04
	117	8.81E+07	1.21E+08	-5.50E+07	7.94E+07	9.10E+05	7.52E+05	4.72E+06	3.37E+06	8.14E+06	1.25E+07	1.66E+04	5.77E+04
4400 rpm	0	7.34E+07	1.58E+08	-1.57E+08	7.86E+07	7.36E+05	8.03E+05	4.68E+06	3.83E+06	2.16E+07	2.74E+07	1.32E+04	2.08E+05
	58	7.39E+07	1.60E+08	-1.34E+08	7.46E+07	7.46E+05	7.21E+05	4.46E+06	3.95E+06	9.88E+06	8.14E+06	1.57E+04	5.41E+04
	117	8.76E+07	1.52E+08	-1.23E+08	7.91E+07	7.59E+05	6.56E+05	5.08E+06	3.76E+06	4.45E+06	2.51E+06	1.70E+04	2.07E+04
6750 rpm	0	1.59E+08	1.94E+08	-1.56E+08	1.69E+08	5.85E+05	6.36E+05	2.66E+06	3.40E+06	4.32E+06	2.43E+06	6.29E+03	7.63E+03
	58	1.62E+08	1.97E+08	-1.69E+08	1.71E+08	5.89E+05	6.20E+05	2.77E+06	3.46E+06	6.60E+06	5.41E+06	4.77E+03	6.92E+03
	117	1.97E+08	2.30E+08	-1.65E+08	2.06E+08	6.04E+05	5.96E+05	3.89E+06	3.11E+06	7.97E+06	4.62E+06	8.68E+03	1.52E+04
9000 rpm	0	2.28E+08	2.36E+08	-1.74E+08	2.27E+08	4.98E+05	5.37E+05	9.41E+06	1.02E+07	1.36E+07	1.35E+07	1.57E+04	2.39E+04
	58	2.34E+08	2.45E+08	-1.71E+08	2.42E+08	5.06E+05	5.51E+05	1.02E+07	9.85E+06	1.67E+07	1.39E+07	1.79E+04	2.37E+04
	117	2.36E+08	2.55E+08	-1.69E+08	2.55E+08	5.24E+05	5.69E+05	7.95E+06	1.01E+07	1.44E+07	1.03E+07	2.17E+04	2.76E+04

APPENDIX C: ADDITIONAL PAST RELEVANT LITERATURE

Akkok, M. and Ettles, C. M., 1980, "The Effect of Grooving and Bore Shape on the Stability of Journal Bearings," ASLE Transactions, **23**(4), pp. 431-441.

Leader, M.E. et al., 1980, "An Experimental Determination of the Instability of a Flexible Rotor in Four-Lobe Bearings," Wear, **58**(1), pp. 35-47.

Flack, R.D. and Allaire, P.E., 1980, "An Experimental and Theoretical Examination of the Static Characteristics of Three-Lobe Bearings," ASME/ASLE International Lubrication Conference, San Francisco, California, pp. 1-7.

Sinhasan, R., Malik, M., and Chandra, M., 1981, "A Comparitive Study of Some Three-Lobe Bearing Configurations," Wear, **72**, pp. 277-286.

Malik, M. et al., 1981, "Performance Characteristics of Tilted Three-Lobe Bearing Configurations", Tribology International, **14(**6), pp. 345-349.

Flack et al., 1982, "Effects of Three-Lobe Bearing Geometries on the Unbalance Response of a Flexible Rotor," ASLE Transactions, **22**(2), pp. 228-235.

Gethin et. al., 1990, "Thermal Behaviour of a Twin Axial Groove Bearing Under Varying Loading Direction," IMechE Journal of Power and Energy, **204**, pp. 77-90
.

Gethin et al., 1992, "A Thermohydrodynamic Analysis of Twin Axial Groove Bearing Under Different Loading Directions and Comparison With Experiment," ASME Journal of Tribology, **114**, pp. 304-310.

Costa, L. et al., 2000, "An Experimental Investigation of the Effect of Groove Location and Supply Pressure on the THD Performance of a Steadily Loaded Journal Bearing," Journal of Tribology, **122**(1), pp. 227-232.

Flack et al., 2000, "Experimental and Predicted Rigid-Rotor Stability Threshold of Axial Groove and Three-Lobe Bearings", Proceedings of the ISROMAC-8, Honolulu, HI

Flack et al., 2002, "Experimental and Predicted Rigid-Rotor Stability Threshold of Three-Lobe Bearings: Effects of Load Orientation", Proceedings of the ISROMAC-9, Honolulu, HI

Solghar, A. A. et al, 2011, "An Experimental Study of the Influence of Loading Direction on the Thermohydrodynamic Behaviour of Twin Axial Groove Journal Bearing," Proceedings of the Institution of Mechanical Engineers, Part J: Journal of Engineering Tribology, **225**(5), pp. 245-254.

Bhushan, 2011, "Effect of Load Orientation on the Stability of a Three-Lobe Bearing Supporting Rigid and Flexible Rotors," Wear, **81**, pp. 195-199